Charmonium production in proton-nucleus collisions at the LHC in collider and fixed-target modes

Cynthia Hadjidakis

▶ To cite this version:

HAL Id: tel-02910790

http://hal.in2p3.fr/tel-02910790

Submitted on 3 Aug 2020

Charmonium production in proton-nucleus collisions at the LHC in collider and fixed-target modes

Habilitation à diriger des recherches de l'Université Paris-Saclay

Habilitation présentée et soutenue à Orsay, le 5 juin 2020, par

CYNTHIA HADJIDAKIS

Composition du Jury :

Jean-Yves Ollitrault Université Paris-Saclay (IPhT)	Président et rapporteur
Anton Andronic Université de Münster	Rapporteur
Joao Seixas Institut supérieur technique de Lisbonne	Rapporteur
Sergey Barsuk Université Paris-Saclay (IJCLab)	Examinateur
Gines Martinez Subatech Nantes	Examinateur

Contents

Introduction

The charmonium family, bound states of charm and anti-charm quarks, is an important tool for the study of Quantum Chromodynamics (QCD) in high-energy hadronic collisions. In proton-proton collisions, thanks to the large mass of the charm quark, the scattering process of charm quark pair production can be described with perturbative QCD. On the other hand, the formation of the charm quark pair into a bound state is a non perturbative process as it involves long distances and soft momentum scales. Theoretical and experimental studies of charmonium production, as well as of open heavy-flavour and bottomonium production, provide a testing ground for both perturbative and non-perturbative aspects of QCD calculations. In nucleus-nucleus collisions, charmonium production is one of the probe of the hot and strongly coupled medium, the quark-gluon plasma (QGP), created at high enough energy and/or density. In particular, the hard scattering process of charm quark pair is expected to take place at the early stage of the collision before the thermalisation of the QGP phase and the charm quark pair to experience the full evolution of the system. In proton-nucleus collisions, the effects from ordinary nuclear matter, also denoted as cold nuclear matter (CNM) effects in opposition to the QGP medium, can modify the charmonium production *w.r.t.* to its normalised production in pp collisions. The CNM effects include the modification of the effective partonic distribution in nuclei, the saturation of the gluon saturation phase space at sufficiently high energy, the multiple scattering and energy loss of partons in nuclei before and after the hard scattering, the absorption or break-up of charmonium states in the nucleus, and the interaction with other particles produced in the collision. Studying CNM effects is important by its own as it gives insight on the modification of the gluon densities in the nuclei, on the interaction between a heavy-quark bound states with light hadrons, or on the medium-induced energy loss of heavy-quark pair. Such studies are also used in the interpretation of charmonium measurements in AA collisions where CNM effects may modify the charmonium yield additionally to the QGP.

In Chapter 1, the production mechanisms of charmonium in pp collisions and the nuclear effects on its production in AA and pA collisions will be discussed. In particular, the CNM effects that arise in pA collisions, as well as the observables used to quantify them, will be described in details.

Charmonium production in pPb collisions at the LHC will be described in Chapter 2. In particular, the analysis of inclusive J/ψ production at $\sqrt{s_{NN}}$ = 5.02 TeV with the ALICE muon spectrometer will be detailed. The results on charmonium production at $\sqrt{s_{NN}}$ = 5.02 and 8.16 TeV will be discussed, also in the context of LHC and RHIC results on open and hidden heavy-flavour measurements in pA collisions.

Finally, the physics opportunities to study charmonium production in pA collisions in a fixed-target mode at the LHC will be discussed in Chapter 3. The general motivations for a fixed-target experiment at the LHC will be presented, as well as the possible and current implementations. The physics opportunities and the expected performances in the case of charmonium production in pA collisions will be described.

Chapter 1

Charmonium production mechanisms and nuclear effects in pA and AA collisions

The charmonium family is extensively studied theoretically and experimentally since its discovery in 1974 as it provides a testing ground for both perturbative and non-perturbative aspects of QCD calculations in high-energy hadronic collisions. In heavy-ion collisions, it is an important process used to characterise the quark-gluon plasma formed in nucleus-nucleus collisions and to probe the cold nuclear matter effects that arise in proton-nucleus collisions. In the following, the charmonium states and its production mechanism in pp collisions will be briefly described. Hot medium effects on charmonium production in AA collisions will be then discussed. Finally, the cold nuclear matter effects than can modify charmonium production in pA collisions will be reviewed in details.

1.1 Charmonium states

Charmonium is a flavorless meson that consists of a charm quark and a charm antiquark. The J/ψ was the first discovered charmonium in 1974, thanks to its large cross section, significant branching ratio for muonic decay and low mass of 3.1 GeV/c^2. Its two-letter name was formed from the names given by the two simultaneous discoverers: "J" from the group of BNL and "Psi" from the one of SLAC. The discovery of excited states, such as the first J/ψ excited state, $\psi(2S)$, came fastly afterwards. Nowadays, 17 states of charmonium have been experimentally established [1]. The lowest mass charmonium is the η_c(1S) with a mass of 2.98 GeV/c^2. Figure 1.1 shows the charmonium family states, their quantum numbers and hadronic decay modes.

Thanks to the hadronic and radiative transitions, a given charmonium state can be the product of the decay of an excited state. One refers to *direct* production whenever a given state is directly produced and to *indirect* if it originates from the feed-down of an excited states. The sum of these two contributions give the *prompt* contribution. It is crucial to measure precisely the feed-down contribution of a given state in order to interpret its measurements. Table 1.1 [2] summarizes the feed-down fraction for J/ψ in hadroproduction at LHC energies. Low (high) p_T corresponds to p_T values of about 2 (14) GeV/c.

	direct	from χ_{c1}	from χ_{c2}	from $\psi(2S)$
low p_T J/ψ	$79.5 \pm 4\%$	$8 \pm 2\%$	$6 \pm 1.5\%$	$6.5 \pm 1.5\%$
high p_T J/ψ	$64.5 \pm 5\%$	$23 \pm 5\%$	$5 \pm 2\%$	$7.5 \pm 0.5\%$

Table 1.1: J/ψ feed-down contribution at LHC energies [2].

In addition, the weak decay of beauty mesons can lead to a charmonium state. This represents the
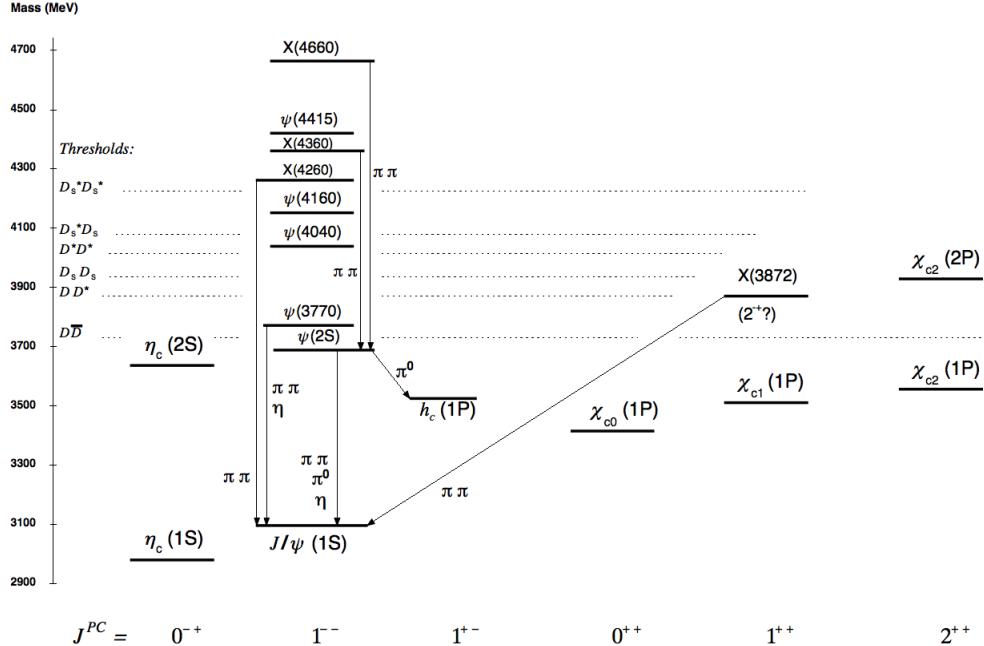
Figure 1.1: Charmonium family with experimentally established $c\bar{c}$ states. Spin-singlet states are called η_c and h_c, spin-triplet states ψ and χ_{cJ}, and unassigned charmonium-like states X. Only observed hadronic transitions are shown. The single photon transitions $\psi(nS) \rightarrow \gamma\eta_c(mS)$, $\psi(nS) \rightarrow \gamma\chi_{cJ}(mP)$, and $\chi_{cJ}(1P) \rightarrow \gamma J/\psi$ are omitted for clarity. Figure from [1].

non-prompt contribution to charmonium production. Since the *b*-hadron lifetime is large, it is possible experimentally to separate the prompt from the non-prompt contribution thanks to a vertex detector with a good precision that allows to isolate the *b*-decay vertex from the main collision vertex. The *inclusive* production is the sum of the *prompt* and the *non-prompt* contributions.

1.2 Charmonium production in pp collisions

The charmonium, and more generally the quarkonium production, is extensively studied since its discovery by different theoretical approaches. Nowadays, its production can be described within the Quantum Chromodynamics (QCD) framework by assuming a factorisation between perturbative and non-perturbative processes.

In pp collisions, the hard scattering of partons inside the two colliding hadrons can result in the production of the charm quark pair. This process can be described perturbatively because of the large mass of the charm quark. The cross section of this process can be written as:

$$\sigma_{c\bar{c}} = \sum_{i,j} \int dx_i \, dx_j \, f_i(x_i, \mu_F) \, f_j(x_j, \mu_F) \, \sigma_{ij \rightarrow c\bar{c}}(x_i, x_j, \mu_F, \mu_R, \sqrt{s}) \tag{1.1}$$

where $x_{i,j}$ are the fractions of the hadron momenta carried by the partons i and j, $f_{i,j}$ are the Parton Distribution Functions (PDFs) and $\sigma_{ij \rightarrow c\bar{c}}$ is the partonic cross-section. There are two scales entering the equation: the factorisation and the renormalisation scales, μ_F and μ_R, respectively. These scales are introduced to cancel the divergences that appear in the calculations of the Feynman diagram at limited order of the coupling constant α_S. The renormalisation scale, entering the $c\bar{c}$ pair production amplitude, cancel the ultraviolet

4

divergences due to large momentum in the loop of Feynam diagram and the infrared divergences that arise in case of zero momentum of real or virtual particle. The factorisation scale, of which the PDFs and the process amplitude depend on, cures the infrared divergences that appear when massless particles radiate other massless particles. These scale values are not physical and unknown. They are usually fixed to a physics meaningful value such as the produced particle transverse mass and they are varied in the calculations (*e.g.* 2μ and $\mu/2$) in order to test the sensitivity of the theory to those parameters.

At LHC energy, heavy quarks are mainly produced by gluon fusion [3] and the gluon PDFs, such as MSTW08 (see *e.g.* [4]), extracted from deep inelastic scattering and Drell-Yan data, are used.

The $c\bar{c}$ pair evolves then into a charmonium state. The hadronisation is a non perturbative process and is described theoretically by three different approaches: the Color Evaporation Model (CEM), the Color Singlet Model (CSM) and the Non-Relativistic QCD model (NRQCD).

The CEM considers that every $c\bar{c}$ pair produced with a mass above the charm pair threshold production and below twice the open heavy flavour (D meson) threshold production evolves into a charmonium. Since the $c\bar{c}$ pair can be produced in a color-singlet or color-octet state, this model assumes that the color of the produced color-octet $c\bar{c}$ pair "evaporates" through gluon emission that does not change its momentum. The charmonium cross section is then simply an integral over the mass of the charm pair:

$$\sigma_\psi = F_\psi \int_{2m_c}^{2m_D} \frac{d\sigma_{c\bar{c}}}{dm_{c\bar{c}}} dm_{c\bar{c}} \tag{1.2}$$

where the phenomenological factor F_ψ represents the probability for the $c\bar{c}$ pair to evolve into a given charmonium state. It is a constant defined for a given charmonium state that can be obtained from its total cross section. This model is quite successful to describe a large set of data but does not provide any predictions for the polarisation of charmonia.

The CSM assumes no evolution of the quantum state of the pair (spin, colour) between its production and its hadronisation into a charmonium state. Therefore, the hard scattering can produce only color-singlet $c\bar{c}$ pairs. The name "Color Singlet Model" refers to this assumption. The cross section depends on the Schrödinger wave function at the origin in the position space and can be written as:

$$\sigma_\psi = \sigma_{c\bar{c}} |\psi(0)|^2. \tag{1.3}$$

This model is predictive for hadroproduction data since $\psi(0)$ can be extracted from charmonium decay width measurements. It reproduces well the hadroproduction cross section at low p_T. It however largely underestimates the large p_T spectra. It was found that higher order corrections in α_S are larger than the Leading Order (LO) calculations and are needed for describing the full p_T spectrum [2].

Finally, NRQCD is an effective model that considers charmonia can be formed from a $c\bar{c}$ pair either in a color-singlet or a color-octet state. The different probabilities for the transition from a $c\bar{c}$ pair to the charmonium are encoded in the Long Distance Matrix Elements (LDMEs). In that model, the charmonium cross section can be written as:

$$\sigma_\psi = \sum_n \sum_{i,j} \int dx_i \, dx_j \, f_i(x_i, \mu_F) \, f_j(x_j, \mu_F) \, \sigma_{ij \to c\bar{c}_n}(x_i, x_j, \mu_F, \mu_R, \sqrt{s}) \, LDME(\psi, n) \tag{1.4}$$

with n representing the different quantum number of the $c\bar{c}$ pair for a given charmonium state. An extensive set of data sample on charmonium production is then needed to extract the LDMEs. The NRQCD models describe generally well the high-p_T charmonium measurements but can not be extended to low p_T since the NRQCD factorisation of Eq. 1.4 is assumed to hold when the momentum transfer p in the hard-scattering production process is of the order of m_c or larger.

The left panel of Fig. 1.2 shows the inclusive J/ψ p_T-differential cross-section in pp collisions at $\sqrt{s} = 13$ TeV at forward rapidity as measured by ALICE [5]. The data are compared to calculations for prompt
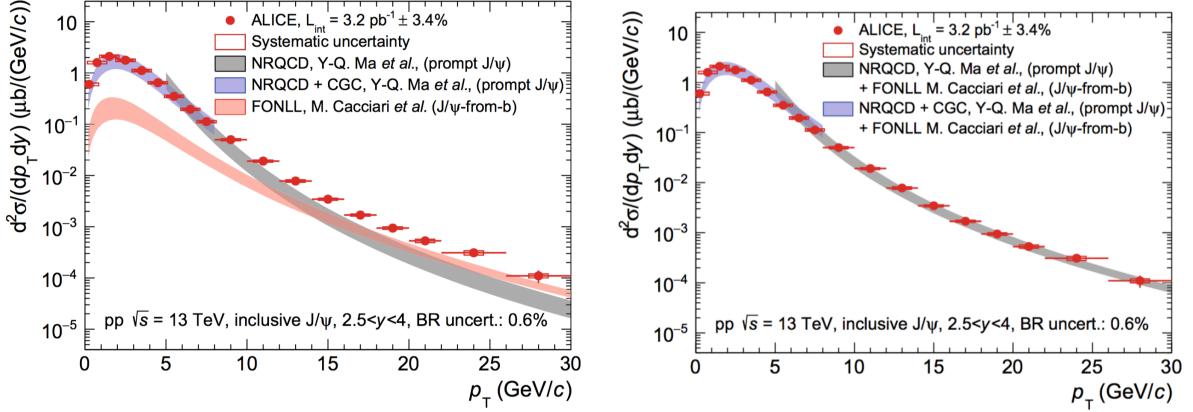
Figure 1.2: Differential cross-section as a function of p_T at $\sqrt{s}$ =13 TeV as measured by ALICE [5] for inclusive J/ψ and compared to theoretical models. In the model calculations, the contributions from prompt and non-prompt J/ψ are separated on the left panel, while they are summed up on the right panel.
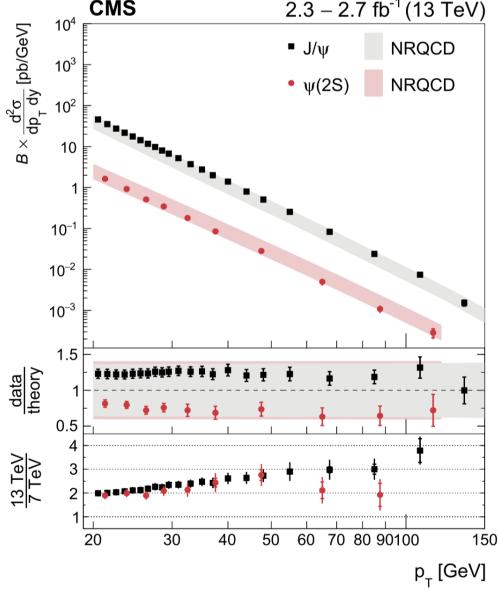
Figure 1.3: Differential cross-section as a function of p_T at $\sqrt{s}$ =13 TeV as measured by CMS [6] for prompt J/ψ and $\psi(2S)$ for $|y| < 1.2$ and compared to NLO NRQCD.

J/ψ from a NRQCD model at NLO [7] and a NRQCD model coupled to a Color Glass Condensate (CGC) description of the low-x gluons in the proton [8]. Since the measurement is inclusive for these data, the non-prompt contribution estimated from FONLL calculations [9] is also shown. This contribution is of the same order as the prompt one at p_T = 15 GeV/c and is lower than 10% for p_T < 8 GeV/c. On the right panel of Fig. 1.2, the data are compared to the sum of the NRQCD and FONLL calculations. Figure 1.3 shows the prompt J/ψ and $\psi(2S)$ cross sections as a function of p_T in a large p_T interval for p_T > 20 GeV/c from CMS [6]. The data are also compared to the NRQCD model at NLO [7] for prompt J/ψ and $\psi(2S)$. Within uncertainties, the calculations from NLO NRQCD (with the FONLL contribution for ALICE data) agree with the LHC data over a large p_T interval for p_T > 5 GeV/c. At lower p_T, the calculations from NRQCD coupled to CGC describe well the data.

In order to better constrain these models, it is valuable to get precise charmonium measurements as a function of transverse momentum, rapidity and at various energies. The charmonium polarisation measurement is also crucial since the various approaches give different expectations/predictions. Associated production of charmonium (charmonium associated to a jet, double charmonium production, etc) is another tool to dig into the charmonium production mechanism. Studies of bottomonia, bound state of beauty and anti-beauty quarks, allow one to constrain the models at a larger mass scale.

1.3 Probing the quark gluon plasma with charmonia in AA collisions

1.3.1 Quark gluon plasma

The quark gluon plasma (QGP) is a state of matter predicted by lattice QCD to exist at high temperature and/or energy density. This matter consists of deconfined quarks and gluons. The temperature (T) and baryo-chemical potential (μ_B) define the phases of the QCD matter. When the temperature or energy density decreases, the quarks and gluons hadronize and there is a transition between the QGP and the hadronic matter as shown in the QCD matter phase diagram in the left panel of Fig. 1.4. Lattice QCD calculations from the HotQCD Collaboration predicts that at $\mu_B = 0$, the critical temperature (T_c) that defines a deconfined QCD medium is $T_c = 156.5 \pm 1.5$ MeV [10].
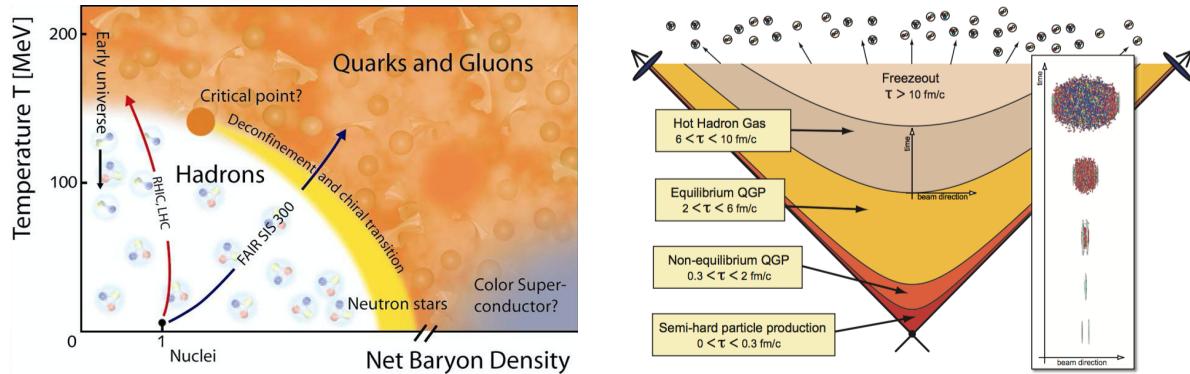
Figure 1.4: Left: Sketch of the QCD matter phase diagram. Right: Schematic view of the space-time evolution of the QGP as generated in an ultra-relativistic heavy-ion collision. The given values of the phase lifetimes correspond to LHC energies and to the core of the created fireball. Figure from [11].

It is believed that the Universe was in a QGP state up to a few microseconds after the Big Bang. Experimentally, this state of matter can be created by colliding heavy-ions at very high energy. The space-time evolution of the two heavy nuclei interaction is illustrated in the right panel of Fig. 1.4. At the initial stage of the collision, the partons from the two incoming nuclei scatter and quarks, gluons and other hard-scale states are created through hard processes. Then the medium made of deconfined partons thermalize though multiple parton scattering. This is the QGP phase with a non-equilibrium and an equilibrium phases. The system continue then to expand and to cool down and, below T_c, the partons hadronize and the system becomes a hot hadronic gas. One can then distinguish the chemical and kinetic freeze-out stages. At chemical freeze-out, there are no more inelastic interactions and the number of formed hadrons in the collision is defined. At kinetic freeze-out, the density is too low and there are no more elastic interactions between the hadrons and the kinematics of the produced hadrons do not evolve anymore.

In heavy-ion collisions, many particles are produced. For instance, in PbPb collisions at $\sqrt{s_{NN}} = 5.02$ TeV, 21.4 k charged particles are produced in the 5% most central collisions [12]. Various probes can then be used to study the QGP, such as:

- particles at low p_T made of light quarks (soft particles): multiparticle correlations give access to the bulk properties in a hydrodynamic picture,

- strangeness production: strangeness particles are predicted to be enhanced in a QGP,

- jet and high p_T particle production: jets are quenched due to parton energy loss in a QGP,

- electromagnetic probes such as direct photons and dileptons productions at low p_T: thermal photons can be radiated in QGP and hot hadronic matter phases,

- quarkonium production, see next Section.

Heavy-ion experiments have searched for the QGP phase since 1980. Experiments at the SPS at CERN first announced evidences of a new state of matter in 2010. In the same year the RHIC experiments at BNL, after ten years of operation, published new results stating that the observations obtained so far in AuAu collisions at $\sqrt{s_{NN}} = 200$ GeV suggest interactions between quarks and gluons in the medium formed in the collisions. After this period of discovery, the RHIC experiments continued the exploratory phase of QGP by collecting high statistic data. The LHC extended the exploratory phase of the QGP by using PbPb collisions at $\sqrt{s_{NN}} = 2.76$ and 5.02 TeV. Such high energetic collisions form the longest-lived deconfined medium with the highest energy density over the largest volume ever produced in the laboratory, at nearly vanishing μ_B. The set of results obtained at the LHC have refined the physical picture established at RHIC: an almost perfect fluid with vanishing mean-free path and high color charge density that leads to a medium opaque to the energetic colored particles that traverse it. At LHC, collective-like dynamics in high multiplicity pp and pPb collisions have also been discovered, questioning the origin of the collective patterns. Ongoing studies and future measurements at RHIC and the LHC will allow one to better constrain the QGP properties and define the dynamical origin of the collective behaviour.

1.3.2 Hot medium effects on charmonium production

Studying the particle production in heavy-ion collisions can probe the QGP created in such collisions. Particles made of heavy quarks are particularly interesting as heavy quarks are expected to be produced by hard partonic scatterings in the initial stage of the collision before the thermalization of the QGP phase and to experience the full space-time evolution of the system. Also in contrast with light hadrons, charmonium masses are largely determined by the bare charm quark masses. These large quark mass allow a calculation of many basic charmonium properties using a non-relativistic potential theory, as illustrated in Table 1.2 for the mass, binding energy and radius of some quarkonium states. These tightly bound states and of very small spatial size, such as the J/ψ, are not expected to be dissociated by hadronic interaction.

It was predicted in [13] that the production of quarkonia is suppressed in case of a QGP formation with respect to its production in a hadronic medium. The suppression would arise from the color screening of the force that binds the $q\bar{q}$ state. In this scenario, since the binding energy and radius depends on the quarkonium state, quarkonium suppression should occur sequentially [14]. For the charmonium family, the strongly J/ψ bound state should melt at higher medium temperature than the more loosely bound states: the χ_c and $\psi(2S)$. Since the χ_c and $\psi(2S)$ contribute to the J/ψ production from feed-down (indirect production), the J/ψ production in the hot medium should be first suppressed from $\psi(2S)$ melting, then from χ_c melting and finally from direct J/ψ melting. However, this prediction of a J/ψ sequential suppression pattern is complicated by several other effects: the regeneration process in hot medium and various effects in cold matter that we will discuss in Section 1.4.

At LHC energy, the charm cross section is large and lead in heavy-ion collisions to a large number of charm quarks in the deconfined medium. These charm quarks could combine and produce charmonium states

State	J/ψ	χ_c(1P)	ψ(2S)	Υ(1S)	χ_b(1P)	Υ(2S)	χ_b(2P)	Υ(3S)
Mass [GeV/c^2]	3.10	3.53	3.68	9.46	9.99	10.02	10.26	10.36
Binding energy [GeV]	0.64	0.20	0.05	1.10	0.67	0.54	0.31	0.20
Radius [fm]	0.50	0.72	0.90	0.28	0.44	0.56	0.68	0.78

Table 1.2: Masses, binding energies and radius of the charmonium and bottomonium states obtained from a non-relativistic potential model [15]. The binding energies are the differences between the quarkonium masses and the open charm or beauty threshold, respectively.

in the QGP or at the phase boundary between the QGP and the hadronic matter [16, 17]. In this scenario of regeneration, charmonium production is enhanced in the QGP with respect to a hadronic medium.

Experimentally, charmonium production can be compared to its production in pp collisions. In that case, one defines the nuclear modification factor R_{AA} that can be written as:

$$R_{AA} = \frac{Y_{AA}}{T_{AA} \times \sigma_{pp}}$$

(1.5)

where Y_{AA} is the charmonium invariant yield in AA collisions, T_{AA} the nuclear overlap function calculated using the Glauber model and σ_{pp} the cross section measured in pp collisions at the same energy. R_{AA} is expected to be equal to unity if the AA collision consists of an incoherent superposition of nucleon-nucleon collisions, i.e. without nuclear effect.

The azimuthal anisotropy of the final-state particle momentum distribution is sensitive to the geometry and the dynamics of the early stages of the collision. The spatial anisotropy in non-central collisions is expected to be transferred to the final momentum via multiple collisions in case of a strongly coupled medium. The second coefficient (v_2) of the Fourier expansion of the particle azimuthal distribution with respect to the reaction plane is called elliptic flow. Here the reaction plane is defined by the beam axis and the impact parameter vector of the colliding nuclei. If charm quarks thermalize in the QGP, then regenerated J/ψ can have a large v_2. In contrast, for primordial J/ψ that survive the QGP, only a small azimuthal anisotropy is expected due to the shorter in-plane versus out-of-plane path length in non-central collisions.

Measurements carried out at SPS and RHIC energies have revealed a suppression of J/ψ production in the most central collisions [18, 19, 20, 21]. At the LHC energy, the suppression of J/ψ was found to have a lower magnitude in the low p_T region, below $\sim$ 6 GeV/c [22, 23]. These results suggest a non-negligible contribution from J/ψ produced via the combination of charm quarks in the medium at LHC. In addition, non-zero v_2 were observed for D [24, 25] and J/ψ [26] mesons in semi-central PbPb collisions at $\sqrt{s_{NN}} = $ 5.02 TeV, suggesting that charm quarks thermalize and flow with the bulk of particles during the QGP phase.

However, for a correct interpretation of the energy, rapidity and p_T dependence of the measured suppression, different effects such as those due to cold or hot nuclear matter have to be considered. The cold nuclear matter (CNM) effects, that will be described in the next section, can influence the quarkonium production in heavy-ion collisions without the need of the QGP formation. Characterizing the QGP produced in heavy-ion collisions therefore requires an accurate study of the cold nuclear matter effects.

1.4 Nuclear effects in pA collisions on charmonium production

The cold nuclear matter (CNM) effects modify the production of charmonium production in nuclear collisions with respect to pp collisions and can be precisely measured in pA collisions, where one does not expect hot nuclear matter effects. These effects include the modification of the effective partonic distribution in nuclei, the saturation of the gluon saturation phase space at sufficiently high energy, the multiple scattering of

partons in nuclei before and after the hard scattering, the absorption or break-up of charmonium states in the nucleus, and the interaction with other particles produced in the collision. In this Section, typical timescale and kinematic relative to pA collisions will be presented, the CNM effects will then be described in details and the interpolation of the nuclear effects from pA to AA collisions will be shortly discussed.

1.4.1 Production timescales

The CNM effects often refer to various time scales entering the process of charmonium production:

- production time (or coherence time): it is the $Q\bar{Q}$ pair production time and is of the order of $\tau_c = 1/m_{Q\bar{Q}} < 0.1$ fm/c in the $Q\bar{Q}$ rest frame. In the rest frame of the target nucleus, the production time is $t_c = E_{Q\bar{Q}}/m_{Q\bar{Q}}^2$, where $E_{Q\bar{Q}}$ is the heavy quark pair energy in the nucleus rest frame.

- formation time: it is the time needed by the $Q\bar{Q}$ pair to develop the charmonium wave function and is much larger than the coherence time. Using the uncertainty principle, it is related to the mass splitting between the 1S and 2S states [27]: $\tau_f = 1/(m_{2S} - m_{1S}) \sim 0.3$ fm/c. In the nucleus rest frame, this formation time is denoted as t_f.

- color neutralisation time: it is the time for the $Q\bar{Q}$ pair to neutralise its colour. In the colour singlet model, this process occurs though the emission of a perturbative gluon and should thus occur in a time comparable to τ_c. In the colour octet and colour evaporation models, colour neutralisation occurs through a soft process on a long timescale, of the order of the quarkonium formation time, τ_f.

- crossing time: it is the time spent by the $Q\bar{Q}$ state in the nucleus. It is given by $\tau_{\mathrm{cross}} = L/\beta_z\gamma$ [28], where L is the longitudinal path of the $Q\bar{Q}$ pair or formed charmonium through the nucleus, β_z and $\gamma = 1/\sqrt{1 - \beta_z^2}$ are the velocity and Lorentz factor of the charmonium along the beam direction in the nucleus rest frame.

1.4.2 Kinematic variables

If one assumes a $2 \rightarrow 1$ partonic process for charmonium production, there is a direct correspondence between the longitudinal momentum fractions x_1 and x_2 of the partons struck in the nucleons and the rapidity y_{cms} of the produced particle in the nucleon-nucleon center-of-mass (cms) frame:

$$x_1 = \frac{m}{\sqrt{s_{NN}}} e^{y_{\mathrm{cms}}} \text{ and } x_2 = \frac{m}{\sqrt{s_{NN}}} e^{-y_{\mathrm{cms}}}, \tag{1.6}$$

with m the mass of the produced particle. So, the momentum fraction of the parton probed depends on the rapidity coverage (detector acceptance), the mass of the particle produced and the center-of-mass energy of the reaction. However, this is a simple assumption, and the x values differ if one assumes different underlying partonic production processes, such as a $2 \rightarrow 2$ partonic process, where the extra degree of freedom can arise from the transverse momentum of the particle produced.

In addition to the usual kinematic variables used in hadronic collisions, such as the rapidity and the transverse momentum, the Feynman variable x_F is often used in pA collisions to describe charmonium production where:

$$x_F = \frac{2p_z}{\sqrt{s_{NN}}} = \frac{2m_{\mathrm{T}}\sinh(y)}{\sqrt{s_{NN}}}, \tag{1.7}$$

with p_z, y and m_{T} the charmonium longitudinal momentum, rapidity and transverse mass. Assuming a $2 \rightarrow 1$ process with $p_{\mathrm{T}} = 0$, one ends up with $x_F = x_1 - x_2$.

1.4.3 Observables

As for the AA case, the nuclear modification factor is often used to quantify the nuclear effects in pA collisions:

$$R_{pA} = \frac{Y_{pA}}{T_{pA} \times \sigma_{pp}}, \tag{1.8}$$

where Y_{pA} is the charmonium invariant yield in pA collisions, T_{pA} the nuclear overlap function calculated using the Glauber model and σ_{pp} the cross section measured in pp collisions at the same energy. This factor can be estimated for different selection on event centrality and as a function of the kinematic variables p_T and rapidity. For minimum bias events, one can also directly use:

$$R_{pA} = \frac{\sigma_{pA}}{A \times \sigma_{pp}}, \tag{1.9}$$

with A the atomic mass number of the nucleus. In past experiments, the nuclear modification was estimated with α such as:

$$\sigma_{pA} = \sigma_{pp} A^{\alpha}. \tag{1.10}$$

In the absence of CNM effects, R_{pA} and α are expected to be equal to 1.

In order to avoid the use of σ_{pp}, the forward-to-backward ratio is also defined as:

$$R_{FB}(y_{\text{cms}}) = \frac{\sigma_{pA}(y_{\text{cms}})}{\sigma_{pA}(-y_{\text{cms}})}. \tag{1.11}$$

This is very useful to cancel out some of the experimental uncertainties and the σ_{pp} uncertainties that appears in the R_{pA} results. However, since the absolute value of the rapidity interval in the backward and forward rapidity intervals has to be the same, this factor is obtained at a cost of reduced statistics *w.r.t.* R_{pPb}.

The $\langle p_T \rangle$ and $\langle p_T^2 \rangle$ are observables that allow to quantify the nuclear effect on the p_T distribution. In particular, the p_T broadening, Δp_T, is defined as:

$$\Delta\langle p_T^2 \rangle = \langle p_T^2 \rangle_{pA} - \langle p_T^2 \rangle_{pp}, \tag{1.12}$$

and is expected to be null when there is no nuclear effect in pA.

In pPb collision, the nuclear modification factor as well as the p_T broadening can also be measured as a function of the centrality of the collision. Indeed the CNM effects are expected to be the largest for the most central collisions. The event centrality can be estimated from the energy deposited in the Zero Degree Calorimeter in ALICE, and the geometry of the collision can be defined thanks to a Glauber model as it will be explained in Section 2.2.3.

It is also possible to perform a measurement of the charmonium yield and $\langle p_T \rangle$ as a function of the charged-particle pseudo-rapidity density, $dN_{\text{ch}}/d\eta$, measured at mid-rapidity. Such measurements can be normalised to their average values and do not require an interpretation of the event classes in terms of the collision geometry. They can be compared to the same measurements performed in pp collisions. A measurement as a function of the multiplicity allows one to select events with very high multiplicities of charged particles where collective-like effects may arise and establish a connection with multiplicity measurements for other probes.

The azimuthal anisotropy of charmonia in non-central pA events (*e.g.* v_2) is also used in order to search for collective effects in pA as in AA.

1.4.4 Cold nuclear matter effects

Nuclear parton distribution functions The dynamics of partons inside free protons may be different from those in bound nucleons inside a nucleus due to the larger density of partons in a nucleus. As a consequence, the free proton PDF of Eq. 1.1 can be modified in a nucleus by a nuclear modification factor R_i^A such as:

$$f_i^A(x, \mu_F^2) = R_i^A(x, \mu_F^2) \times f_i(x, \mu_F^2). \tag{1.13}$$

$f_i^A(x, \mu_F^2)$ is the nuclear parton distribution function (nPDF). As illustrated in the left panel of Fig. 1.5, the dependence of the nuclear modification factor factor over x defines four regions. The shadowing region covers small $x \lesssim 5 \times 10^{-2}$ where R_i^A is lower than 1. The anti-shadowing region lies at intermediate x values $5 \times 10^{-2} \lesssim x \lesssim 5 \times 10^{-1}$ where R_i^A is higher than 1. The EMC-effect region, named after its observation by the EMC Collaboration [29], cover the high $x \gtrsim 5 \times 10^{-1}$ where R_i^A is lower than 1. Finally the Fermi-motion region is defined for $x \rightarrow 1$, where R_i^A is higher than 1.

The parametrisation of R_i^A for each nucleus and parton flavour are determined as a function of x and factorisation scale from global fit analyses of lepton-nucleus and proton-nucleus data, as for instance the EPPS16 [30] and nCTEQ15 [31] analyses. The right panel of Fig. 1.5 shows the gluon nuclear modification factor from the EPPS16 analysis at Q^2=1.69 GeV^2/c^2. The uncertainty in that analysis is very large at small x, in the shadowing region, and at very large x, in the EMC-effect region, because of the lack of existing data that probes the gluon content of nucleon. Note the uncertainty decreases with increasing Q^2. With the LHC data, the nuclear gluon distribution can be further constrained from electroweak bosons and heavy-flavour productions [32, 33].
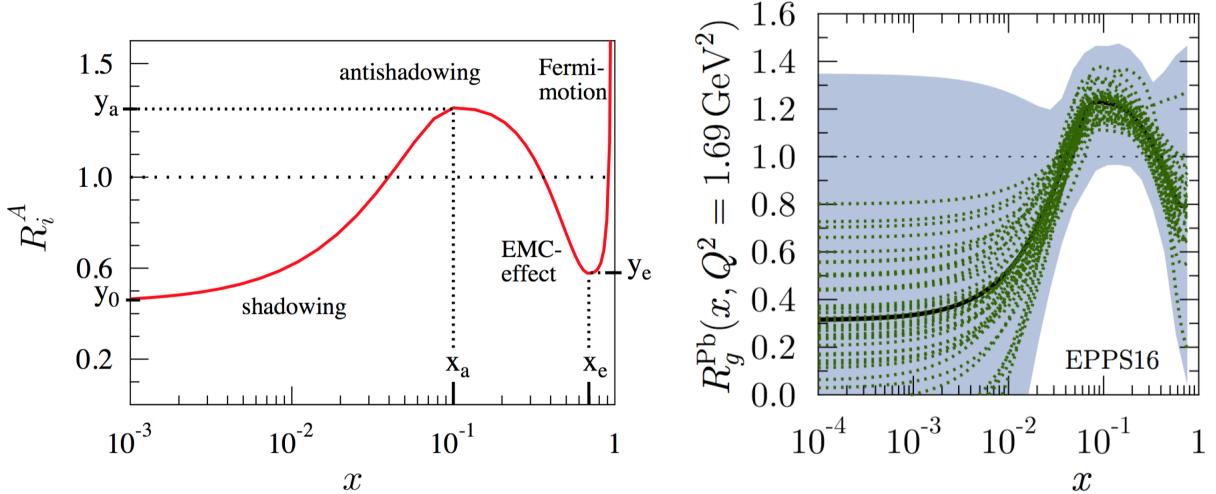
Figure 1.5: Left: illustrative picture of the parton nuclear parton distribution function as a function of the parton longitudinal momentum fraction of the nucleon, x. Picture from [34]. Right: nuclear modification factor as a function of x from EPPS16 analysis at Q^2=1.69 GeV^2 [30].

In the case of J/ψ production, the left panel of Fig. 1.6 shows the x-range of the parton in the nucleus probed by four experiments: NA3, E866, PHENIX and ALICE, operating at various center-of-mass energies per nucleon pair. A simple $2 \rightarrow 1$ partonic process was assumed for this calculation. At forward rapidity in ALICE, J/ψ production involves gluons with a x value that can be down to 5×10^{-5} while at backward rapidity, the x value is of the order of 5×10^{-2}, quite similar to the values probed at mid-rapidity with PHENIX or with the fixed-target experiment E866. In the nPDF framework, a scaling of the nuclear effect with x_2 is expected. This scaling is not observed if one considers the α factor from Eq. 1.10 as a function

of x_2 and measurements from NA3, E866 and PHENIX as shown in the right panel of Fig. 1.6. This scaling violation may be attributed to other CNM effects such as nuclear absorption or coherent energy loss.
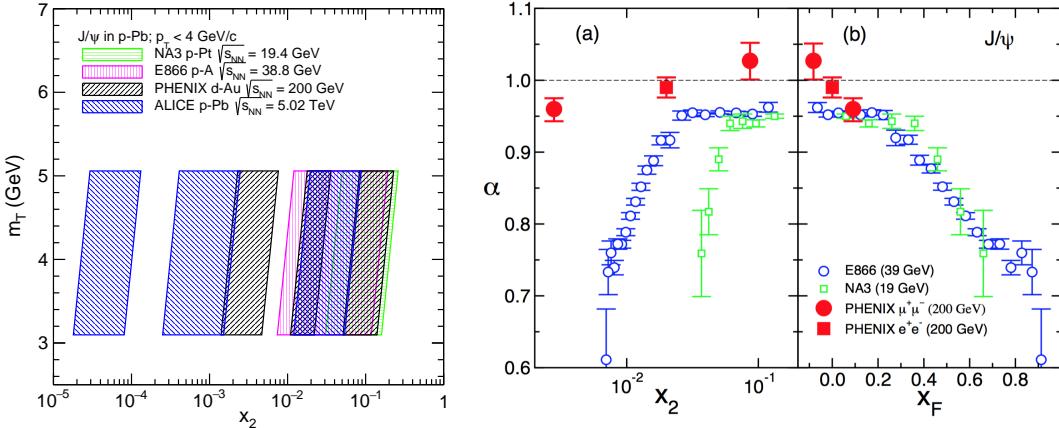
Figure 1.6: Left: x-range probed by NA3, E866, PHENIX and ALICE experiments by assuming $x_2 = m_T/\sqrt{s_{NN}} e^{-y_{CM}}$. Right: α as a function of x_2 and x_F from NA3, E866 and PHENIX experiments. Figure from [35].

Parton saturation in the nucleus   The suppression of small-x parton in the nucleus can alternatively be described within the Color Glass Condensate (CGC) theoretical framework [36], where the initial nucleus is seen as a coherent and dense gluonic system. While in the nPDF approach, the small-x evaluation of the PDF is described with the DGLAP linear evolution equation, the CGC framework is based on the JIMWLK non-linear evolution equations that describes the saturation of the gluon density in the nucleus at small-x. In charmonium production models [37, 38, 39, 40, 41], multiple scattering of the initial gluons and produced heavy-quark pair traversing the dense nucleus are also considered. The numerical values obtained are often valid only for a restricted interval of rapidity, $y > 0$, where the nucleus can be seen as a dense system and the incoming proton is treated as a dilute system. This approximation allows for a factorization between a dense system described by the CGC and a dilute system parametrized with the usual PDFs.

The left panel of Fig. 1.7 shows the comparison of the J/ψ nuclear modification factor measured at forward rapidity with PHENIX with the CGC model from [38]. While at $p_T > 4$ GeV/c there is a good agreement between the calculations and the data, the large Cronin peak at $p_T \sim 2$ GeV/c from multiple scattering in the model is not seen in the data.

In the CGC approach from [41], soft color exchanges between the $c\bar{c}$ pair and the sources (*i.e.* the proton or nucleus) can also affect the charmonium production. The effect from soft color exchanges with the sources has little impact on the J/ψ but not on the $\psi(2S)$ which is more weakly bound.

Parton multiple scattering and energy loss   Multiple scattering of partons and of the $c\bar{c}$ pair in the nucleus before and/or after the hard scattering can lead to radiative or collisional parton energy loss and consequently to the broadening of the charmonium transverse momentum. The latter is also known as the Cronin effect. The multiple scattering is often characterised by the transport coefficient of cold nuclear matter, $\hat{q}$.

The approach from [42] is based on the transport properties of the partons in large nuclei. When the scattering from the medium is largely incoherent, the parton modification is dominated by transverse momentum broadening that leads to the large Cronin-like enhancement at intermediate p_T of the order of few GeV/c. Instead, when the longitudinal momentum transfer is small compared to the inverse path length of

13

the parton as it propagates through the nucleus, the scattering becomes coherent, which can lead to atten-uation, or shadowing. Multiple scattering also leads to medium-induced radiative corrections that have the interpretation of energy loss in the limit of soft gluon emission.

In the model from [43], the J/ψ production in pA collisions is described within the dipole approach, assuming the dominance of the CSM mechanism for the p_T-integrated cross section. Shadowing and energy loss contributions are accounted for. In particular, the propagation and attenuation of the dipole $c\bar{c}$ pair in nuclear matter and the gluon shadowing leads to a J/ψ suppression that increases with the colliding energy because the dipole cross section increases accordingly. The energy loss contribution is significant at forward rapidity at RHIC energy. In order to reproduce the almost constant and large J/ψ suppression observed at low p_T from RHIC to LHC energy, another contribution from multiple colour exchange interaction of a $c\bar{c}$ pair with different bound nucleons in the nuclear matter was introduced. This contribution leads to J/ψ enhancement in nuclei *w.r.t.* proton and is more important at high energy.

Finally, coherent energy loss was proposed in [44] to explain the large J/ψ suppression observed at for-ward rapidity/large x_F from AGS to RHIC energy. In this model, the charmonium is assumed to be produced from the splitting of a gluon into a $c\bar{c}$ pair in an octet state. At large $c\bar{c}$ pair energy and small production angle in the nucleus rest frame, the medium induces energy loss that scales as the $c\bar{c}$ pair energy. The gluon radiation induced by the medium arises from the interference between the initial and final state emission am-plitudes, hence it is a coherent energy loss process. Coherent energy loss depends on the production process and while it is also predicted for open heavy flavour meson production, it is not for Drell-Yan production.

The right panel of Fig. 1.7 shows the comparison of the J/ψ normalised cross-section ratio [1] between W and Be measured at E866 at the AGS [45] with the coherent parton energy loss model from [44] that describes well the broad x_F interval.
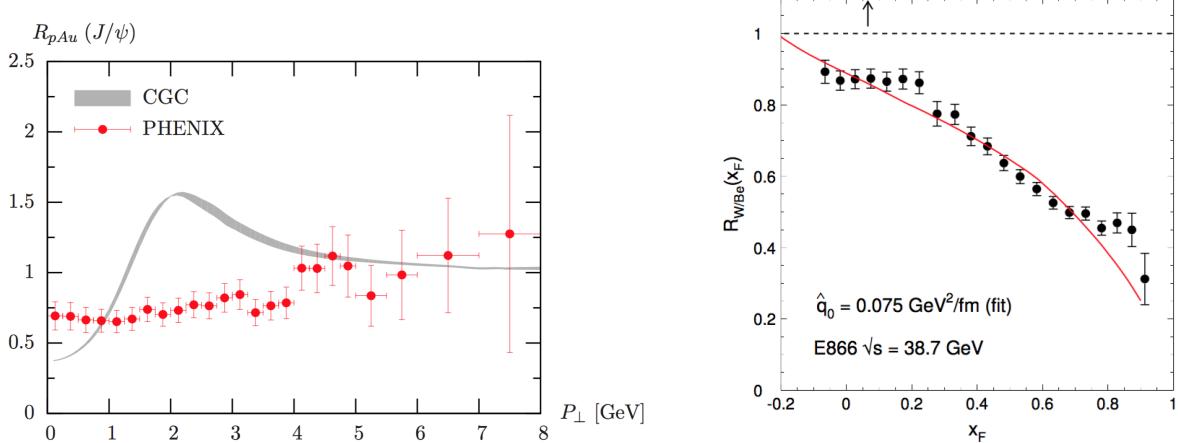
Figure 1.7: Left: J/ψ nuclear modification factor as a function of p_T $1.2 < y < 2.2$ at PHENIX compared to a CGC model [38]. Right: J/ψ normalised cross-section ratio between W and Be as a function of x_F at E866 [45] as compared to an energy loss model [44].

Nuclear absorption   Final-state inelastic interactions can dissociate the $c\bar{c}$ bound state when passing through the nucleus, leading to a suppression of charmonium production. In that case, one expects different disso-

---

[1]E866 released the parameter α such as $\sigma_A = \sigma_N \times A^\alpha$ where A is the atomic mass number and σ_N the cross section on a nucleon. Measurements were performed for Be, Fe and W targets. From α, one can compute the normalised cross-section ratio between two targets such as: $R_{W/Be} = R_{pW}/R_{pBe} = (A_W/A_{Be})^{\alpha-1}$ where $R_{pA} = \sigma_{pA}/(A \times \sigma_N)$.

ciation rate depending on the bound state radius, i.e. more suppression for $\psi(2S)$ than J/ψ according to Table 1.2. To quantify this effect, the break-up or absorption cross section, σ_{abs}, was defined. It represents the inelastic cross section of a charmonium state with a nucleon. Since the J/ψ is not necessarily fully formed, σ_{abs} can rather be seen as an effective J/ψ-nucleon cross section. Various studies were carried out to extract it from pA measurements, by assuming a factorisation between the charmonium production and its absorption in the nuclear matter. Most of these studies show that σ_{abs} decreases with the colliding energy at mid-rapidity [46] and with a decreasing time spent in the nucleus [47]. Indeed, at large energy, the formation time t_f becomes much larger than the nuclear size. Consequently, the charmonium state is produced far outside the nucleus and should not be sensitive to nuclear absorption. This is the case at LHC energy for almost all rapidity intervals but very large backward rapidity interval, $y \lesssim -3.8$ [48]. At lower colliding energy, nuclear absorption can not be excluded and has to be considered when interpreting results obtained with ion beam/target.

Comoving particles In order to describe the SPS pA and AA results on J/ψ and $\psi(2S)$ production, it was proposed that the charmonia, produced outside of the nucleus and surrounded by a dense system of hadrons, mainly pions, could convert into open charm due to the interactions with the comoving medium. The comovers are defined as particles produced at the same rapidity as the charmonia. This purely final-state effect could describe well the SPS data [49] in heavy-ion collisions, when considering it on top of the effect from nuclear absorption. It was also used to describe the RHIC and LHC data [50, 51] in addition to the nPDF initial-state effect. Since the $\psi(2S)$ is less bound than the J/ψ, this model can reproduce the relative suppression of $\psi(2S)$ to J/ψ as observed at PHENIX [52] at backward and mid-rapidity in pAu and dAu collisions, as shown in the left panel of Fig. 1.8. In that model, the comoving particles can also suppress slightly the J/ψ production, in particular at backward rapidity in pA collisions (corresponding to the nucleus-going direction), characterized by a larger charged-particle multiplicity.
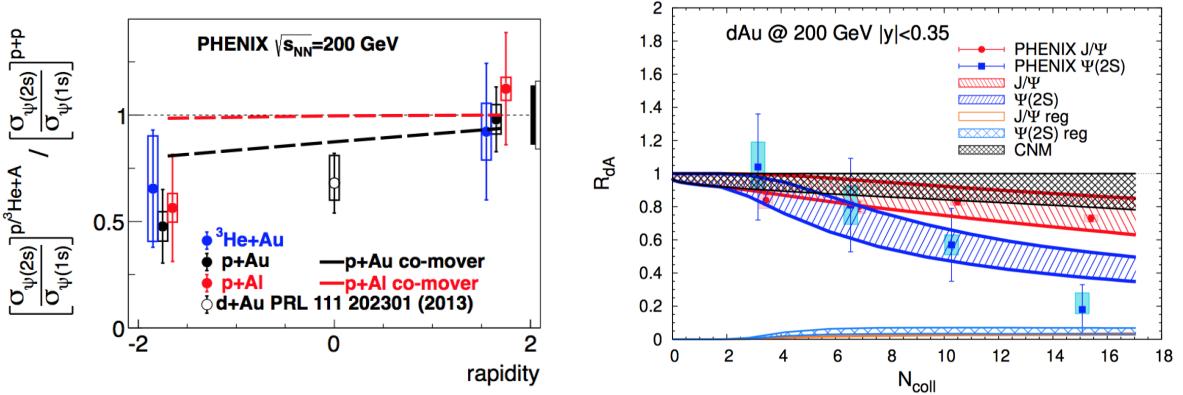
Figure 1.8: Left: double ratio of $\psi(2S)$ to J/ψ production in pp and p (or light nucleus)-A collisions as a function of rapidity at PHENIX and comparison with a comover model [51]. Right: J/ψ and $\psi(2S)$ nuclear modification factor in dAu collisions at PHENIX and comparison with calculations from a transport model [53]. In that model, CNM effects include shadowing and multiple scattering in the initial state.

Hot nuclear matter effect in pA The discovery of long-range correlations in high-multiplicity pp and pA collisions at RHIC and LHC has increased the interest of the heavy-ion community for small collision systems. Further studies using multi-particle correlations [54, 55, 56] support the interpretation of collective origin to explain the observed long-range correlations in pp and pA collisions. It is however not clear

whether the collective effects in small systems at high multiplicity have the same origin as those observed in AA collisions. For charmonium production, some transport models [57, 58, 53] assume that hot fireballs are created in the most central collisions in pA collisions. The relative suppression of $\psi(2S)$ *w.r.t.* J/ψ as a function of the number of binary collisions is shown in the right panel of Fig. 1.8 for mid-rapidity interval at RHIC. The data are well reproduced by those transport models, *e.g.* the calculations from [53] which is also displayed in the Figure. In this model, the final state effect from the hot medium is considered on top of the CNM effects. Also, the regeneration component of the charmonium production in pA collisions is found to have a small effect at RHIC and LHC. Note that in [59], a model based on the transport approach considers the dissociation of the $\psi(2S)$ in both QGP and hadron gas to describe the $\psi(2S)$ suppression in dAu collisions at RHIC.

1.4.5 Extrapolating nuclear effects from pA to AA collisions

It is important to understand whether cold nuclear matter effects can be extrapolated from pA to AA collisions. Some models assume a factorisation of the CNM effects in AA collisions and related works show that the cold nuclear matter effects can be extrapolated from pA to AA in nPDF model, see *e.g.* [60], and coherent energy loss model [61]. Note that in those models, the nuclear effect on charmonium excited states production is similar to that on the J/ψ one. Since additional nuclear effect was measured for $\psi(2S)$ *w.r.t.* J/ψ production, a factorisation approach of the CNM effects should consider this additional effect, if possible. Also it is crucial to investigate if such additional nuclear effect applies to direct J/ψ and χ_c production. Measurements on χ_c production in pA collisions are however still lacking. First measurements were carried out at RHIC [28] but the large uncertainties prevent any firm conclusion.

On the other hand, other models consider that the extrapolation of the CNM effects measured in pA collisions to AA collisions is delicate due to interference effects between the two nuclei involved in the collisions, such as in the approach from [62].

Chapter 2

Charmonium production measurements in pPb collisions at the LHC

In 2013 and 2016, the LHC delivered pPb collisions at $\sqrt{s_{NN}}$ = 5.02 and 8.16 TeV, respectively, as part of the LHC heavy-ion program. These runs provided to the LHC experiments, ALICE, ATLAS, CMS and LHCb large luminosities and high statistical data samples, in particular at $\sqrt{s_{NN}}$ = 8.16 TeV. In this Chapter, we will focus on charmonium production measurements in the backward ($-4.46 < y_{\rm cms} < -2.96$) and in the forward ($2.03 < y_{\rm cms} < 3.53$) center-of-mass rapidity intervals in ALICE. First, the ALICE detectors will be briefly described, then the data analysis on J/ψ production in pPb collisions at $\sqrt{s_{NN}}$ = 5.02 TeV will be detailed and finally the results on charmonium production in pPb collisions at $\sqrt{s_{NN}}$ = 5.02 and 8.16 TeV in ALICE will be discussed, also in the context of other results from LHC and RHIC on open and hidden heavy-flavour measurements.

2.1 ALICE detectors at the LHC

ALICE is the LHC experiment dedicated to the study of the QGP. The ALICE detectors (see Fig. 2.1) are composed of global detectors, that trigger on minimum bias events and give information on the event characteristics, such as event plane and centrality, of a central barrel at mid-rapidity and of a muon spectrometer at forward rapidity. In that section, only the detectors that were used in the charmonium pPb analysis are mentioned. More details on the ALICE detectors can be found in [63, 64].

2.1.1 Global detectors

V0 The V0 detector is composed of two scintillator hodoscopes placed at forward rapidity on each side of the interaction point: on the A-side at z = 340 cm covering $2.8 < \eta < 5.1$ and on the C-side at $z = -90$ cm covering $-3.7 < \eta < -1.7$. They are mainly used for triggering purposes with a time resolution of 1 ns, allowing to trigger on minimum bias events in all collision systems with a high efficiency. The minimum bias (MB) trigger is defined by a coincidence of the signals from both V0 hodoscopes (V0AND). They are also used to remove beam-gas events displaced from the main interaction vertex that can be identified by measuring the time difference between the V0A and V0C. The V0 is used to estimate the collision centrality by measuring the charged particle multiplicity. Finally, it is also used for the measurement of the luminosity, along with the T0 detector.

T0 The T0 detectors are two quartz Cherenkov counters, placed on each side of the interaction point covering $-3.28 < \eta < -2.97$ and $4.61 < \eta < 4.92$. They are used to measure precisely the event time

17
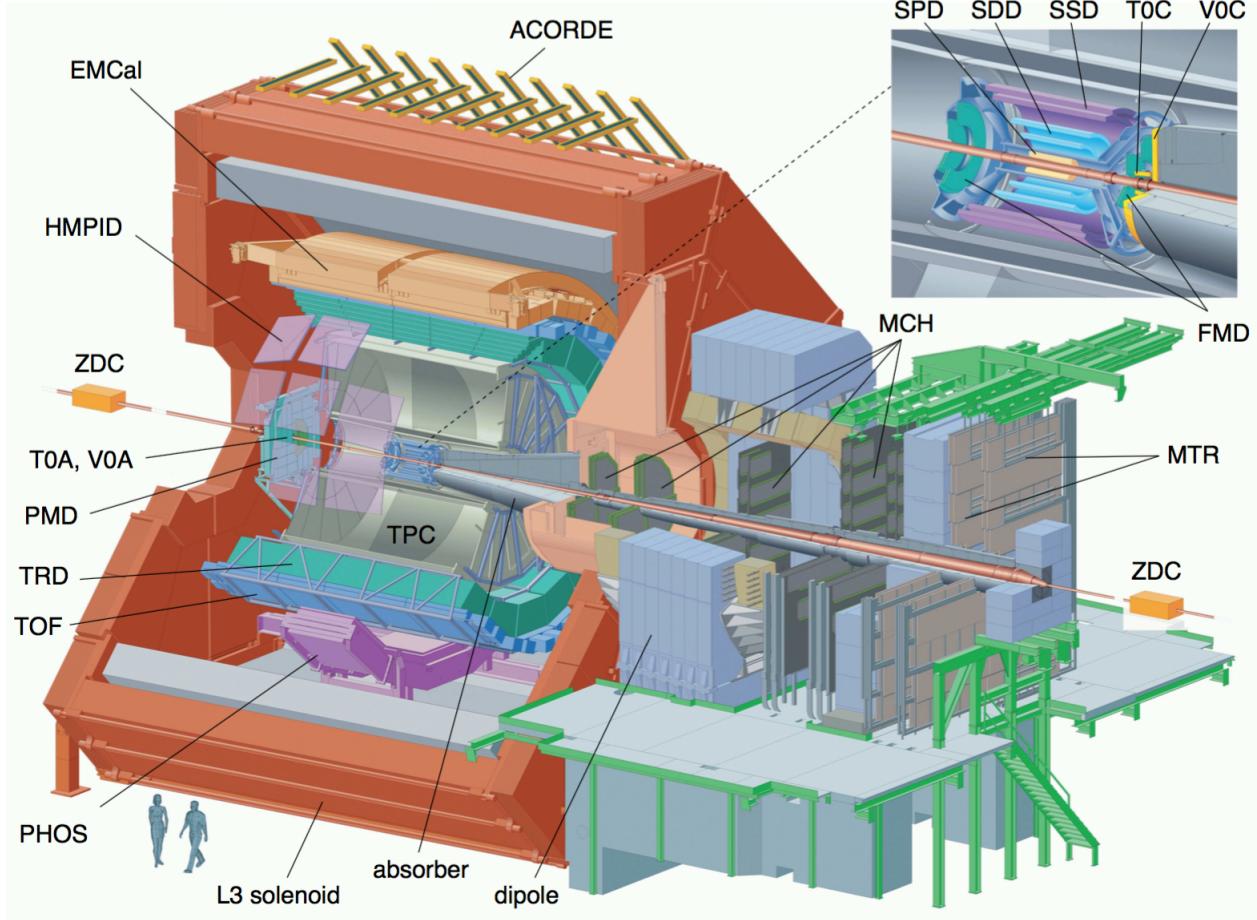
Figure 2.1: The ALICE experiment at the CERN LHC. The central-barrel detectors (ITS, TPC, TRD, TOF, PHOS, EMCal, and HMPID) are embedded in a solenoid with magnetic field B = 0.5 T and provide particle detection and identification at midrapidity. The detector ACORDE, positioned on top of the magnet, triggers on cosmic-rays. Forward detectors (PMD, FMD, V0, T0, and ZDC) are used for triggering, event characterization, and multiplicity studies. The muon spectrometer provides muon detection and identification at forward rapidity.

information with a time resolution of 20-40 ps and for the luminosity determination.

Zero-Degree Calorimeter (ZDC) The ZDC consists of two sets of hadronic calorimeters positioned symmetrically at 112.5 m from the interaction point. They are quartz fibers sampling calorimeters that measure the energy deposited by spectator protons and neutrons emitted from the nucleus following the collision. Spectator nucleons can be nucleons produced from de-excitation processes or knocked-out by wounded nucleons. The neutron calorimeter (ZN) is positioned between the two beam pipes downstream of the first machine dipole that separates the beams. The proton calorimeter (ZP) is installed externally to the outgoing beam pipe. The ZDCs are also used to remove parasitic p-Pb interactions displaced from the nominal interaction point. The energy deposited in the ZDC is an estimator of the collision centrality.

2.1.2 Central barrel

The central barrel detectors are placed in a solenoidal magnetic field of 0.5 T and cover a pseudorapidity range of $|\eta| < 0.9$. They are composed of the Inner Tracking System (ITS), the Time Projection Chamber (TPC), the Transition Radiation Detector (TRD) and the Time-Of-Flight (TOF). Those detectors have a full azimuthal coverage. In addition the High Momentum Particle Identification (HMPID) detector, the Electromagnetic Calorimeter (EMCal) and the Photon Spectrometer (PHOS) have a limited azimuthal coverage.

The ITS contains six cylindrical layers of silicon detectors with the innermost layer at a radius of 3.9 cm with respect to the beam axis and the outermost layer at 43 cm. The two innermost layers are equipped with Silicon Pixel Detectors (SPD). The track segments (tracklets) reconstructed from the hits in the SPD layers are used for reconstructing the primary interaction vertex position as well as vertices from simultaneous interactions per bunch crossing (pile-up). The position of the interaction vertex is also determined, with better resolution, from the tracks reconstructed in the TPC and the ITS. The ITS is also used to reconstruct secondary vertices from decays of heavy-flavour particles.

The TPC is the main tracking and particle identification (PID) device and is a gaseous drift detector with a cylindrical geometry extending from 85 to 247 cm in the radial direction and 500 cm longitudinally. The PID is performed via the measurement of the specific energy loss, dE/dx, in the gas volume.

2.1.3 Muon spectrometer

The muon spectrometer covers the pseudorapidity interval of $-4 < \eta < -2.5$. It consists of a dipole magnet with an integrated field of 3 Tm, five high-granularity tracking stations comprising two planes of Cathode Pad Chambers each, two trigger stations consisting of two planes of Resistive Plate Chambers each and a system of absorbers.

The tracking system was designed to achieve a spatial resolution of about $100\,\mu$m (in order to obtain an invariant mass resolution of about 100 MeV/c^2 at the Υ mass) and to operate at a maximum readout rate of 1 kHz. It can operate at a hit density lower than 5×10^{-2} cm^{-2}. It consists of five tracking stations; two tracking stations are placed before the dipole magnet, one inside and two after. Each station consists of two Multi-Wire Proportional Chambers and each chamber has two cathode planes to provide two-dimensional hit information. A mixture of Ar (80%) and C0$_2$ (20%) gas fills the volume between the two cathode planes. The first station is located behind the absorber to measure the exit points of the muons. To keep the occupancy at about 5%, a fine-granularity segmentation of the readout pads was needed: pads as small as 4.2×6.3 mm^2 are used for the region of the first station close to the beam pipe, where the highest multiplicity is expected. Since the hit density decreases with the distance from the beam, larger pads are used at larger radii. Two different designs were adopted: the first two stations are based on a quadrant structure (four quadrants per chamber) and the three last stations have a slat architecture (up to 26 slats per chamber, the larger slat dimension being 40×280 cm^2). In both cases, the quadrants and slats overlap to ensure a full azimuthal coverage.

The total number of readout channels is 1.08 million. The tracking front-end electronics is based on chips called MANAS, reading 16 channels each. Four MANAS are read out by a chip called MARC, performing in particular the suppression of the channel pedestal values. This readout chain is mounted on front-end boards called MANUs. There are 17000 MANU to readout all the channels of the tracking system. Each chamber is then readout by two CROCUS that concentrate the data and send them to the DAQ. The trigger signals coming from the Central Trigger Processor (CTP) are distributed to MANU by the CROCUS through the Trigger Crate Interface (TCI). The TCI decodes the trigger signals and manages the busy signals of the CROCUS crates.

The trigger system was designed to deliver trigger signals to the CTP, in less than 800 ns after the interaction and at 40 MHz frequency. In order to reduce the rate of the trigger signal, a p_T cut is applied on each triggered muon, requiring a position-sensitive trigger detector with a space resolution better than

1 cm. The muon trigger system consists of four Resistive Plate Chambers planes arranged in two stations. It provides single muon and dimuon triggers, in combination with the MB trigger set by the V0 detector. The dimuon triggers are defined by the detection of two unlike-sign or like-sign muon candidate tracks in the trigger system. The muon triggers select muons with a transverse momentum above a threshold of $p_T = 0.5$, 1, 1.7 or 4.2 GeV/c. Two thresholds can be programmed for a given period and those are referred to "low" and "high" thresholds. These thresholds are not sharp in p_T and the single-muon trigger efficiency reaches a plateau value of $\sim 96\%$ at $p_T \sim 1.5$ GeV/c for the 0.5 GeV/c trigger threshold.

A system of absorbers is used for filtering out the hadrons produced in the collision and before the absorbers by decaying particles: the front absorber, made of concrete, carbon and steel with a thickness of 4.1 m (10 nuclear interaction lengths) is installed between the interaction region and the muon tracking stations; a second absorber, a 1.2 m thick iron wall (7.2 nuclear interaction lengths), is located upstream of the trigger stations and absorbs secondary hadrons escaping from the front absorber and low-momentum muons produced predominantly from π and K decays. Finally, a conical absorber placed around the beam pipe protects the spectrometer from secondary particles produced in interactions of large-η primary particles with the beam pipe. The combined effect of the front absorber and the muon filter leads to a detection threshold of $p > 4$ GeV/c for tracks matching the trigger.

The clusters of charge deposited by the particles crossing the muon tracking chambers are unfolded and fitted to determine their spatial locations. A tracking algorithm reconstructs the trajectory of the particles across the five tracking stations. These tracks are then extrapolated to the vertex position measured by the SPD and their kinematic parameters are further corrected for multiple scattering and energy loss of muons in the front absorber.

During data taking in pp, pPb, PbPb or XeXe collisions, muon trigger and tracking detectors were included in the muon readout cluster with SPD and V0, as well as T0 in pp collisions and ZDC in pPb and AA collisions. In this cluster, the slowest readout detector was the muon tracking with a readout time of about 200 μs with optimal readout channel pedestal values. Pedestal values could however increase with time, leading to an increase of muon trigger dead time and several works were carried out during the Long Shutdown 1 (LS1) to improve the situation. In addition, 8 CROCUS of the first two stations suffer from high frequency of single event upset during high-rate pp and pPb collisions. The busy states of those CROCUS were reset during a run thanks to a DAQ pause and reset procedure that was implemented in LS1.

2.2 Data analysis: focus on inclusive J/ψ production in pPb collisions at $\sqrt{s_{NN}} = 5$ TeV

2.2.1 Rapidity shift

The LHC superconducting magnets were designed to contain two magnet coils on the inside, each surrounding one of the two beam pipes. This two-in-one magnet design imposes an asymmetry of the energy per nucleon of the p and Pb beams ($E_p = 4$ TeV and $E_{Pb} = 4 \times Z_{Pb} = 1.58 \cdot A_{Pb}$ TeV, where $Z_{Pb} = 82$ and $A_{Pb} = 208$ are the lead nucleus atomic and mass number, respectively). The nucleon-nucleon center-of-mass system is also consequently shifted with respect to the laboratory system by $\Delta y = 0.5\, ln(A_{Pb}/Z_{Pb}) = 0.465$ in the p-going direction. The data samples used for the measurements in pPb collisions were collected in two configurations, obtained by inverting the direction of the p and Pb beams. The two beam configurations allow one to measure the J/ψ production using the muon spectrometer in the backward ($-4.46 < y_{cms} < -2.96$) and the forward ($2.03 < y_{cms} < 3.53$) centre-of-mass rapidity (y_{cms}) regions, corresponding to the Pb-going and the p-going directions, respectively. The data samples were requested to have similar luminosities.

2.2.2 Data sample and selection

The data for this analysis were obtained in 2013 during a LHC run dedicated to the heavy-ion programme with an integrated luminosity of 5.81 ± 0.20 nb^{-1} at backward rapidity and 5.01 ± 0.19 nb^{-1} at forward rapidity. The MB trigger is defined by a coincidence of the signals from both sides of the V0 detector. The dimuon triggers require, in addition to the MB condition, the detection of two unlike-sign muon candidate tracks in the trigger system of the muon spectrometer. In these data samples, the trigger p_T threshold is $p_T = 0.5$ GeV/c. The signal timing in SPD and ZDC is required to be compatible with that of nominal pPb interaction in order to reject beam-induced background. The primary vertex is reconstructed from SPD layers. There is not cut on vertex position since the muon resolution does not depend on it. For the analysis as a function of event centrality, events belonging to the centrality class $0 - 2\%$ are removed since the contribution of pile-up events (events with two or more simultaneous interactions per bunch crossing) is estimated to be large for this event class, of the order of $20 - 30\%$. The following cuts are applied to the reconstructed muon tracks: a fiducial cut of $-4 < \eta < -2.5$ corresponding to the muon spectrometer acceptance; a selection on the radial coordinate of the track at the end of the front absorber, $17.6 < R_{abs} < 89.5$ cm, in order to remove particles crossing the high-density section of the absorber; tracks reconstructed with the tracking stations are required to match with tracks reconstructed in the trigger stations, in order to reject background from π and K particles. J/ψ candidates are obtained by combining opposite-sign dimuon pairs. In addition the following selections on dimuon pairs are applied: rapidity cut of $2.5 < |y_{\text{lab}}| < 4$ and $p_T < 15$ GeV/c.

2.2.3 Centrality determination

The determination of event centrality is usually based on charged-particle multiplicity estimated with the V0 signal amplitudes in PbPb collisions. However, in pPb collisions, the magnitude of the multiplicity fluctuations at a given impact parameter is comparable to the whole dynamic range of the minimum bias multiplicity distribution. The fluctuations can be related to various event topologies (*e.g.* hard collisions with large momentum transfers associated to high-multiplicity events, compared to soft collisions without any high-p_T particle), detector acceptance effects (jets fragmenting out of the experimental coverage) or other effects as explained in [65]. A centrality selection based on charged-particle multiplicity may therefore select a sample of pPb collisions that contains biases unrelated to the collision geometry.

In contrast, a centrality selection based on the energy measured with the neutron calorimeter of the ZDC in the Pb-going direction should not induce such a bias. Under this assumption, one can in principle relate the measured ZN energy to the number of binary nucleon collisions. However, in absence of a model which properly relates these two quantities, hybrid methods have been developed [65]. They are based on three assumptions to estimate the average number of binary nucleon collisions, $\langle N_{coll} \rangle$, and the average nuclear overlap function, $\langle T_{\text{pPb}} \rangle$.

The first one assumes that the charged-particle multiplicity measured at mid-rapidity is proportional to the number of participant nucleons, $\langle N_{part} \rangle$. The values of $\langle N_{part} \rangle$ for a given ZN-energy class are calculated by scaling the MB value of the number of participant nucleons by the ratio of the average charged-particle multiplicities measured at mid-rapidity for the considered ZN event class to the corresponding value in MB collisions. $\langle N_{coll} \rangle$ and $\langle T_{\text{pPb}} \rangle$ are calculated from $\langle N_{part} \rangle$ according to the Glauber model [66]. This assumption is used for the published results and the resulting values are denoted as $\langle N_{coll}^{mult} \rangle$ and $\langle T_{\text{pPb}}^{mult} \rangle$ to indicate the ansatz used for their derivation. The second assumption uses the proportionality of $\langle N_{coll} \rangle$ to the yield of high-p_T charged particles ($10 < p_T < 20$ GeV/c) at mid-rapidity. The third method assumes $\langle N_{coll} \rangle$ is proportional to the charged-particle multiplicity measured with the V0 detector in the Pb-going direction, *i.e.* at forward rapidity.

The variation on $\langle N_{coll} \rangle$ obtained with the three methods determine the uncertainty on $\langle N_{coll}^{mult} \rangle$ and $\langle T_{\text{pPb}}^{mult} \rangle$

in each ZN event class. In addition to this hybrid method uncertainty, other uncertainties on $\langle N_{coll}\rangle$ and $\langle T_{pPb}\rangle$ are related to the Glauber model and are obtained by varying the model parameters. Events without a signal in the ZN detector are assigned to the most peripheral event class.

Figure 2.2 shows Q_{pPb} for high-p_T charged particles as a function of centrality, calculated with various centrality estimators. The left panel shows the results when using the V0 (V0M, V0A) and SPD (CL1) detectors. The multiplicity biases are well reproduced by the MonteCarlo G-PYTHIA (lines in the Figure) which is the PYTHIA event generator coupled to a MonteCarlo Glauber calculation. The right panel of Fig. 2.2 shows results from the hybrid method, where the centrality classes are selected with the ZN detector in the Pb-going direction and $\langle N_{coll}\rangle$ are calculated with the hybrid method assumptions. In that case, Q_{pPb} is consistent with unity and the results obtained from the two assumptions used to estimate $\langle N_{coll}\rangle$ are in agreement.
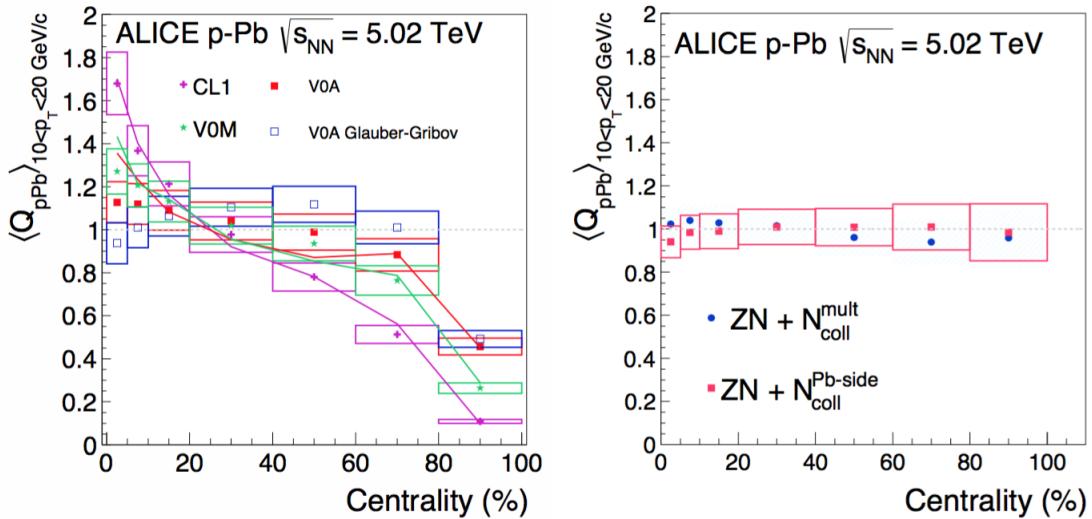

Figure 2.2: Q_{pPb} as a function of centrality for high-p_T ($10 < p_T < 20$ GeV/c) charged particles measured at mid-rapidity, with various centrality estimators. The left panel shows the results from the data with the V0 and SPD centrality estimators while the right panel shows the results obtained from the hybrid method with ZN energy.

2.2.4   Signal extraction

The raw J/ψ yield is estimated for each rapidity, p_T and centrality interval from fits of the dimuon invariant-mass distribution. Various functions, as described in [67], are used for the signal and background parameterisation. The $\psi(2S)$ is also included in the fit function. Figure 2.3 shows the distributions in the forward and backward rapidity intervals with a Crystal Ball functions for the signal and a variable-width Gaussian for the background. The signal functions include non-Gaussian tails that can not be determined by the data due to the poor signal-to-background ratio in the tail regions. The tails are determined from Monte-Carlo simulations for each kinematic (p_T, y) interval. The fits are performed in two different invariant mass ranges. The number of J/ψ is obtained by integrating the signal function over the fitting range. The invariant mass fits are performed using different combination of signal and background functions and fitting ranges. The raw number of J/ψ and the associated statistical uncertainty are given by the mean value of the results from various fits. The systematic uncertainty is obtained from the Root Mean Square of the results from various fits.
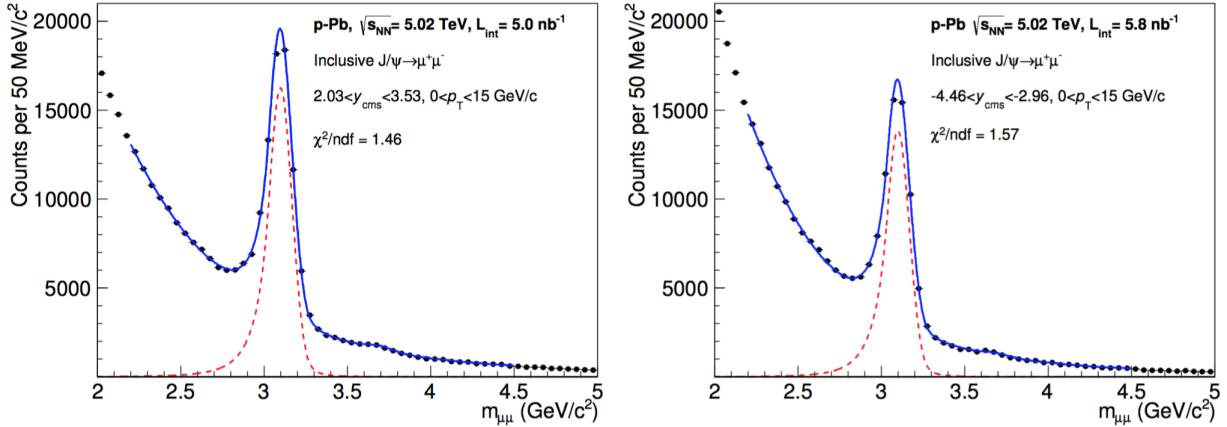
Figure 2.3: Opposite-sign dimuon invariant mass distributions in the forward (left) and backward (right) rapidity intervals. The data are fitted with a Crystal Ball function (red dashed-lines) for the signal and a variable-width Gaussian for the background.

2.2.5 Acceptance efficiency correction

The J/ψ raw yields are corrected by the acceptance and the efficiency ($A \times \epsilon$) of the detectors. The $A \times \epsilon$ is determined from pure signal simulations where the experimental setup is modeled with GEANT3. Signal simulations without background particles are motivated because the muon tracking and trigger efficiency and their resolutions are not deteriorated by the detector occupancy in central pPb collisions (as it is seen in central PbPb collisions). The kinematic distributions of the J/ψ signal in the Monte-Carlo are tuned to the reconstructed distributions using an iterative procedure. The J/ψ is also assumed to be unpolarised, consistent with the measurements performed so far on the polarisation at the LHC [68, 69, 70, 71], however not yet measured for $p_T < 2$ GeV/c. The data reconstruction and analysis procedures are the same in data and simulations. Also the detector conditions and their variation with time during the data-taking periods are considered in the simulations. A dead map is built from data and applied to both data and simulations to reject detector elements for which the efficiency is unstable and not reproducible in simulations. Figure 2.4 shows the $A \times \epsilon$ in the backward and forward rapidity intervals as a function of rapidity (left) and p_T (right). It is smaller at backward rapidity which corresponds to the second data-taking period when the muon tracking detector efficiency is deteriorated. There are three sources of systematic uncertainties related to $A \times \epsilon$: MonteCarlo input distributions, tracking and trigger efficiency. The systematic from the MonteCarlo input distributions was estimated by varying the p_T and rapidity distributions. The efficiency from the trigger and tracking stations can be obtained from the detector redundancy in a station (2 chambers per station). The systematic uncertainty from the tracking efficiency was obtained by comparing the tracking efficiency of single muon from data and simulation. This uncertainty is squared to obtained the dimuon uncertainty. The systematic uncertainty from the trigger efficiency arises from the statistical uncertainty on the measured intrinsic detector efficiency, as well as on the discrepancy between data and simulation for the p_T dependence of the muon trigger efficiency that slightly differ at the p_T trigger threshold. These uncertainties are propagated to an uncertainty on J/ψ by using pure signal simulations.

2.2.6 Normalisation and luminosity determination

The luminosity corresponding to the two data samples are computed from the MB cross-section that is determined using Van der Meer scans [72]. During these scans, the MB triggers were based on the V0 and T0 detectors. Since the analysis is based on a dimuon trigger sample, the equivalent number of MB triggers
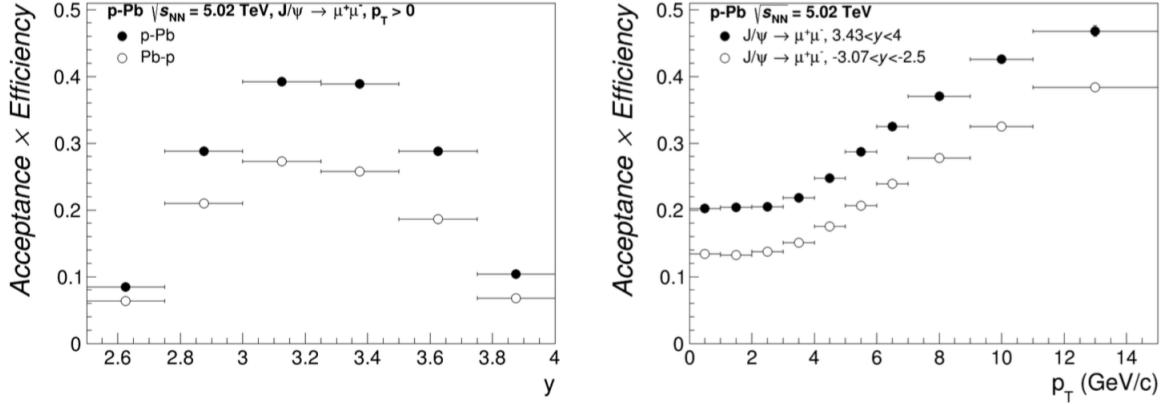
Figure 2.4: Detector acceptance and efficiency as a function of rapidity (left) and p_T (right) in the backward (open points) and forward (full points) rapidity intervals.

is evaluated as $N_{MB}^{eq} = F \times N_{MUL}$ where F is a normalisation factor that represents the inverse probability to have a dimuon trigger in a MB triggered event. This factor can be determined from the recorded data after event selection (offline method) or from the counters recording the number of level-0 triggers (scaler method). The statistic is huge from the scaler method. In both methods, corrections from pile-up events and event selection are needed and are obtained from the recorded data. F has to be computed run per run because the dimuon trigger is polluted by beam-gas tracks. The resulting F factor for each method is taken as the average over the runs weighting by the number of dimuon trigger events. The final F value is taken as the average from the values obtained with the offline and scaler methods and the difference between the two methods gives the systematic uncertainty.

In the data sample, the MB rate could reach 200 kHz. The average number of MB interactions per bunch-crossing can be computed assuming a Poissonian distribution of MB interactions, such as: $\mu = -ln(1 - L0b/(n_b \times f_{rev}))$, where $L0b$ is the number of level-0 MB triggers corrected from beam-gas interaction, n_b the number of colliding bunches and f_{rev} the LHC revolution frequency of 11245 Hz. The MB rate of the considered data samples correspond to a maximum pile-up probability of about 3%.

For the analysis as a function of the event centrality, the normalisation factor, F^{cent}, is obtained for each centrality class from the centrality-integrated value which is scaled by the fraction of MB events and the inverse fraction of dimuon events in a given centrality class. The pile-up event contribution to the number of MB events is estimated by using alternatively the interaction vertices reconstructed with the SPD to select pile-up events, or a fast simulation describing the ZN energy distribution.

The fast simulation is built from the ZN energy distribution of a run with negligible pile-up contribution. The left panel of Fig. 2.5 shows the ZN energy distribution from data (full blue line), from data with negligible pile-up contribution (dotted line) and from fast simulation (full pink line). The shoulder at large ZN energy comes from pile-up contribution and it is well described by the fast simulation. The right panel of Fig. 2.5 shows that the pile-up event contribution is as large as $20 - 30\%$ for the $0 - 2\%$ centrality class. It decreases to 43% for the $2 - 10\%$ centrality class and is less than 2% in all other centrality classes. A systematic uncertainty equal to the pile-up event contribution is assigned to the factors F^{cent}. It was checked by using the ZN fast simulation that the overall effect of pile-up events, including the shift of events from a given centrality class to a more central one, is covered by the systematic uncertainties quoted on F^{cent} for pile-up events.
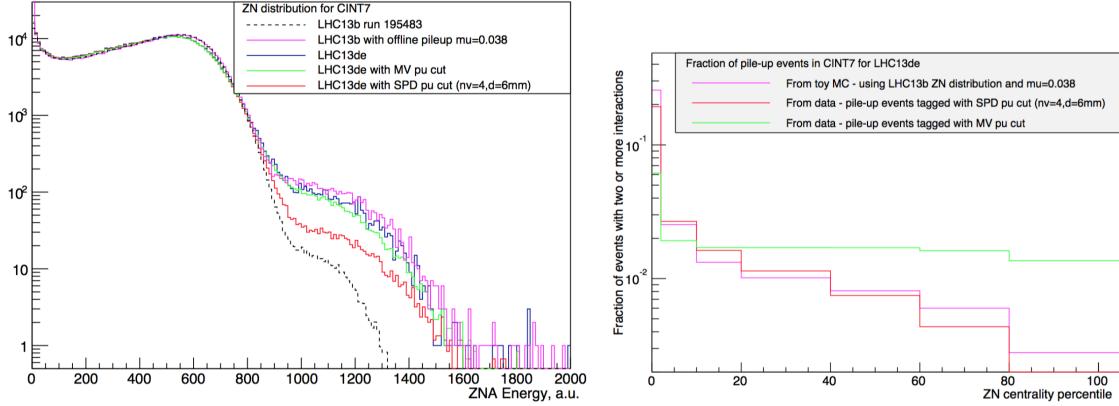
Figure 2.5: Left: ZN energy distribution from data (full blue line), fast simulation (full pink line) and data at low interaction rate (dotted line). Right: fraction of pile-up events in MB trigger as estimated from the SPD detector (red line) and a fast ZN energy simulation (pink line) as a function of centrality class.

2.2.7 pp reference

In order to obtain the nuclear modification factor and the p_T broadening, one needs the J/ψ cross-section in pp collisions at the same energy and in the same rapidity range than the pPb collisions. The first 5.02 TeV pp collisions took place in 2015, well after the pPb collisions at the same energy. Note also that pp collisions were delivered at $\sqrt{s}$ = 8 TeV in LHC Run 2 however at slightly lower energy than the corresponding pPb collision energy. At both energies, the rapidity shift in pPb collisions requires an extrapolation of the pp cross-section in rapidity. For these reasons, it was decided to interpolate and extrapolate the pp cross-sections at the energies and the rapidity intervals of the existing measurements. Note that LHCb decided to reduce the rapidity acceptance of the pPb measurements by half unit in order to avoid the rapidity extrapolation step.

The reference pp cross section is obtained from an interpolation/extrapolation procedure described in details in [73]. It uses the ALICE pp results at $\sqrt{s}$ = 2.76 and 7 TeV for the 5.02 TeV interpolation procedure. The $\sqrt{s}$-interpolation is based on three empirical shapes (linear, power law and exponential) and is independently performed for each of the rapidity (p_T) bins corresponding to the measured dσ/dy (dσ/dp_T) values. The resulting values are taken from the average values obtained from the three shapes as shown in the left panel of Fig. 2.6 and their systematic uncertainties are computed from the maximum spread obtained between the three shapes. The rapidity extrapolation is based on three different functions (Gaussian, 2nd and 4th degree polynomials). The resulting values and their systematic uncertainties are estimated as for the energy interpolation procedure. For the p_T-differential procedure, the dσ/dp_T values are also corrected by factors that depend on p_T and that account for the p_T shape modification when the rapidity increases/decreases. These factors are derived from the inclusive J/ψ dσ/dp_Tdy in pp collisions from LHCb.

The inclusive pp cross-section was measured in 2015 [5, 23] and is shown in comparison to the interpolated cross-section in the right panel of Fig. 2.6. The interpolated cross-section is in agreement with the measured cross-section.

2.3 Results on charmonium production and interpretation

In LHC Run 1 and 2, there were two heavy-ion campaigns with pPb collisions: in 2013 at $\sqrt{s_{NN}}$ = 5.02 TeV and in 2016 at $\sqrt{s_{NN}}$ = 8.16 TeV. In both cases, the data taking period was divided in two configurations by inverting the proton and lead beam direction. The integrated luminosity collected by ALICE with the dimuon trigger is higher in 2016: L_{int}^{5TeV} = 5.81 ± 0.20 nb^{-1} and L_{int}^{8TeV} = 12.8 ± 0.3 nb^{-1} at backward rapidity
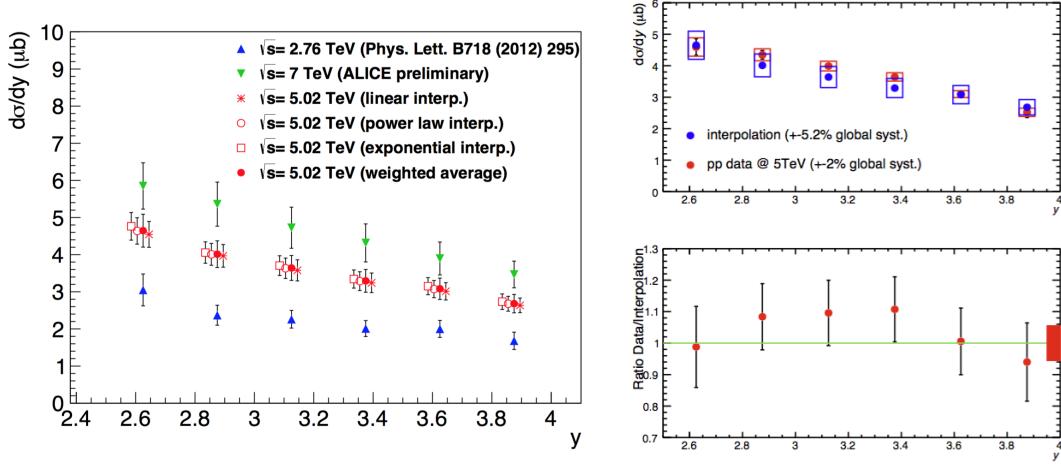
Figure 2.6: Left: Inclusive J/ψ differential cross-section as a function of rapidity at $\sqrt{s}$ =2.76 and 7 TeV and interpolated cross-section at $\sqrt{s}$ = 5.02 TeV obtained with the three interpolation functions as well as for the average values. Right: Inclusive J/ψ cross-section as a function of rapidity at $\sqrt{s}$ = 5.02 TeV and compared to the interpolated cross-section.

and $L_{int}^{5\text{TeV}} = 5.01 \pm 0.19$ nb^{-1} and $L_{int}^{8\text{TeV}} = 8.4 \pm 0.2$ nb^{-1} at forward rapidity. In the following the ALICE J/ψ and $\psi(2S)$ measurements in pPb collisions at $\sqrt{s_{NN}}$ = 5.02 and 8.16 TeV will be presented, and they will be discussed also in the context of the results obtained at LHC on open and hidden heavy-flavour production.

2.3.1 J/ψ measurements in pPb collisions at $\sqrt{s_{NN}}$ = 5.02 and 8.16 TeV

J/ψ cross sections The double differential cross-section for a given centrality class can be written as:

$$\frac{\text{d}^2\sigma_{\text{J}/\psi}^{\text{cent}}}{\text{dyd}p_\text{T}} = \frac{Y_{\text{J}/\psi\to\mu^+\mu^-}^{\text{cent}}}{\text{BR}} \times \sigma_{\text{MB}}, \tag{2.1}$$

where σ_{MB} is the pPb MB cross-section, BR is the branching ratio of the considered J/ψ decay channel, which amounts to $(5.96 \pm 0.03)\%$ for dimuons [1], and $Y_{\text{J}/\psi\to\mu^+\mu^-}^{\text{cent}}$ is the inclusive J/ψ yield per-event. The latter is defined as

$$Y_{\text{J}/\psi\to\mu^+\mu^-}^{\text{cent}} = \frac{N_{\text{J}/\psi\to\mu^+\mu^-}^{cent}}{N_{\text{MB}}^{cent} \cdot (A \times \epsilon) \cdot \Delta y \cdot \Delta p_\text{T}}, \tag{2.2}$$

where $N_{\text{J}/\psi\to\mu^+\mu^-}^{cent}$ is the raw number of J/ψ mesons decaying into dimuons for a given centrality class, rapidity and p_T range, N_{MB}^{cent} is the number of MB events for the given centrality class, $A \times \epsilon$ is the acceptance times efficiency and Δy and Δp_T are the widths of the rapidity and p_T intervals, respectively.

The left panel of Fig. 2.7 shows the inclusive J/ψ differential cross-section as a function of rapidity in pPb collisions at $\sqrt{s_{NN}}$ = 5.02 TeV [74] and the comparison to the normalized pp reference cross-section extrapolated from existing ALICE data [73]. The pp cross-section is normalised by the lead atomic mass number. While the J/ψ production in pPb is close to its normalised production in pp at backward rapidity, it is clearly suppressed at forward rapidity. The right panel of Fig. 2.7 shows the differential cross-section as a function p_T at backward, mid- and forward rapidity [75]. The mid-rapidity data were obtained with the central barrel detectors in the dielectron decay mode. Figure 2.8 shows the J/ψ cross-section as a function p_T for various centrality classes at backward (left) and forward (right) rapidity [76]. Six centrality classes were defined: : 2-10%, 10-20%, 20-40%, 40-60%, 60-80% and 80-100%.

26
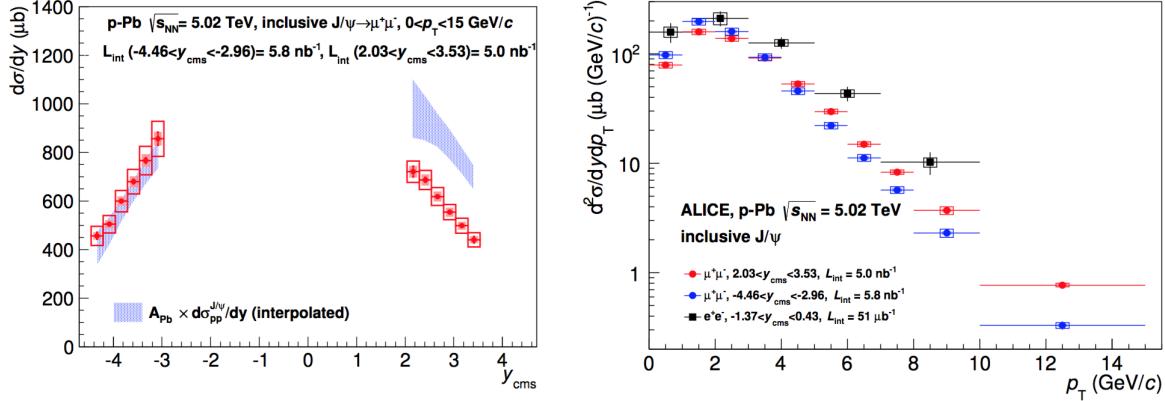
Figure 2.7: Left: inclusive J/ψ y-differential cross-section in pPb collisions at $\sqrt{s_{NN}}$ = 5.02 TeV and comparison to the pp reference cross-section extrapolated from existing ALICE data. Right: inclusive J/ψ p_T-differential cross-section as a function of p_T in pPb collisions at $\sqrt{s_{NN}}$ = 5.02 TeV at backward, mid- and forward rapidity.
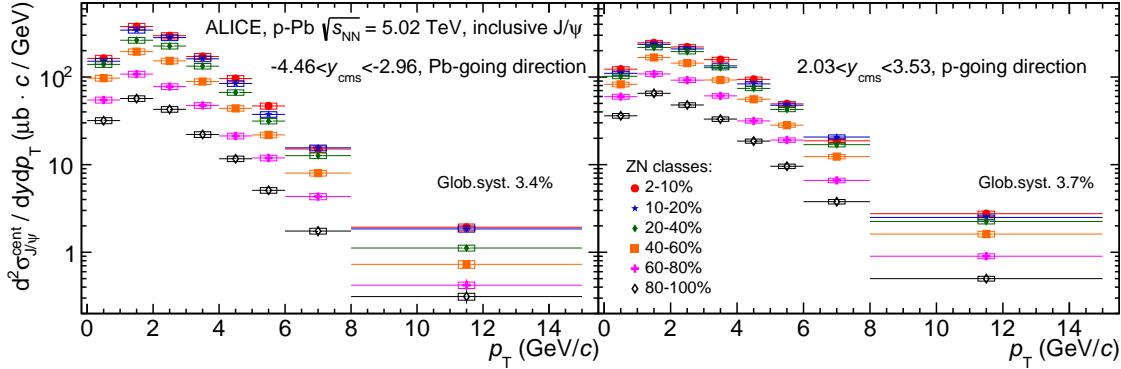

Figure 2.8: Inclusive J/ψ double-differential cross-section as a function of p_T for various centrality classes in pPb collisions at $\sqrt{s_{NN}}$ = 5.02 TeV at backward (left) and forward (right) rapidity.

J/ψ nuclear modification factor The J/ψ nuclear modification factor can be obtained either from the cross section in pPb collisions integrated over centrality, as shown in Eq. 1.8, or from the invariant yield as follows:

$$R_{\text{pPb}} = \frac{Y_{\text{J}/\psi \to \mu^+\mu^-}}{\langle T_{\text{pPb}} \rangle \cdot BR \cdot \sigma_{pp}^{\text{J}/\psi}}. \tag{2.3}$$

with $\langle T_{\text{pPb}} \rangle$ the average nuclear overlap function. For the results obtained in various centrality intervals, the notation Q_{pPb} is used for the nuclear modification factor in order to emphasise the possible bias in the evaluation of $\langle T_{\text{pPb}} \rangle$ (see Section 2.2.3)).

Figure 2.9 shows the rapidity dependence of R_{pPb} at $\sqrt{s_{NN}}$ = 8.16 TeV as measured by ALICE for inclusive J/ψ [77] and LHCb [78] for prompt J/ψ. The inclusive J/ψ R_{pPb} is compatible with unity at backward rapidity. It is lower than one at forward rapidity and it decreases with increasing rapidity. The ALICE results include prompt and non-prompt (from b-hadron decays) J/ψ contributions. When integrating over p_T, the non-prompt contribution to the inclusive yield based on LHCb results [78] is estimated to be of the order of 10-15% at $\sqrt{s_{NN}}$ = 8.16 TeV. The difference between prompt and inclusive J/ψ R_{pPb} have been estimated to be of the order of 1-4% depending on the rapidity. The ALICE and LHCb results show a good agreement in the two rapidity ranges.

27
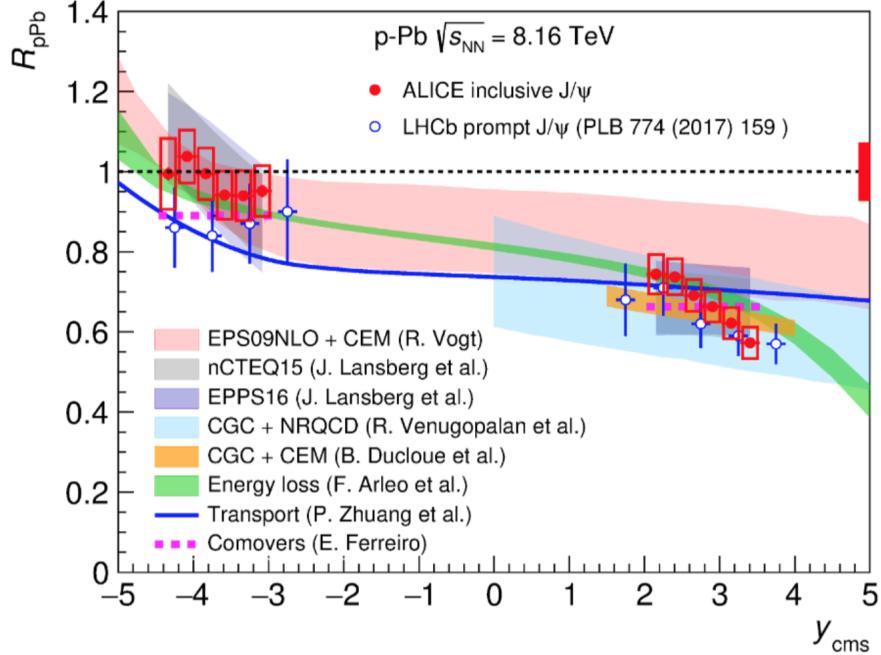
Figure 2.9: Nuclear modification factor of inclusive J/ψ in pPb collisions at $\sqrt{s_{NN}} = 8.16$ TeV as a function of rapidity [77] and comparison to model calculations (see text).

Figure 2.10 shows the inclusive J/ψ R_{pPb} as a function of p_T at $\sqrt{s_{NN}} = 5.02$ TeV [74] and 8.16 TeV [77] in the backward (left) and forward (right) rapidity intervals. The results obtained at both energies agree with each other given the uncertainties. Practically, all the models (*e.g.* [39]) did expect a larger suppression at $\sqrt{s_{NN}} = 8.16$ TeV but not significantly given the uncertainties on the measurements. Thanks to the higher energy and luminosities, the results at $\sqrt{s_{NN}} = 8.16$ TeV are more precise and allow to reach higher p_T: 20 GeV/c at $\sqrt{s_{NN}} = 8.16$ TeV vs 15 GeV/c at $\sqrt{s_{NN}} = 5.02$ TeV for the pPb cross-section, the p_T reach for R_{pPb} at $\sqrt{s_{NN}} = 5.02$ TeV being limited by the pp reference cross-section. In the backward rapidity interval, R_{pPb} increases as a function of p_T and is above unity, but not significantly, for $p_T > 3$ GeV/c at $\sqrt{s_{NN}} = 8.16$ TeV. In the forward rapidity interval, R_{pPb} increases as a function of p_T from 0.6 at low p_T to unity at $p_T \sim 10$ GeV/c. At mid-rapidity, the ALICE measurements using the dielectron decay channel with the central barrel [74] show a similar pattern to the one measured at forward rapidity. The J/ψ is therefore largely suppressed at low p_T for mid- and forward rapidity intervals at LHC energy.

In Fig. 2.11, the data are compared to theoretical calculations. Several groups provided theoretical calculations for the J/ψ R_{pPb}. Some groups provided predictions [37, 79, 80, 81] and others postdictions [32, 39, 41, 51, 40, 43], *i.e.* calculations after the first 5.02 TeV data were released. In Fig. 2.9, a comparison of J/ψ R_{pPb} with several theoretical models for prompt J/ψ is presented.

There are three calculations based on nuclear shadowing only. The model of Vogt [79] is based on the CEM model to describe the J/ψ production associated to the EPS09 nPDF [34]. The model of Lansberg *et al.* [32] uses the LHC data on open and hidden heavy-flavour to constrain the gluon nPDF from a Bayesian-reweighing analysis. For the J/ψ production, a data driven modeling of the scattering at the partonic level, folded with one proton PDF and one lead nPDF, was used [82]. For nPDF, this model uses nCTEQ15 [31] or EPPS16 [30]. These three shadowing calculations describe well the rapidity dependence. If one considers a $2 \rightarrow 1$ partonic process for J/ψ production, the x values probes correspond to the shadowing region ($x \sim 5 \times 10^{-5}$) at forward rapidity and to the transition interval between the shadowing and the anti-shadowing
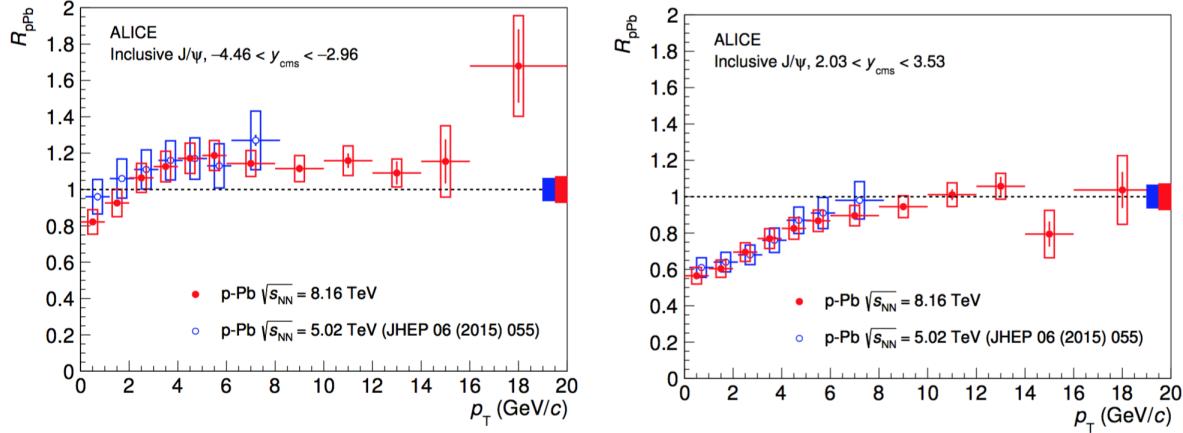
Figure 2.10: Nuclear modification factor of inclusive J/ψ in pPb collisions at $\sqrt{s_{NN}} = 5.02$ and 8.16 TeV as a function of p_T [75, 77] at backward (left) and forward (right) rapidity.
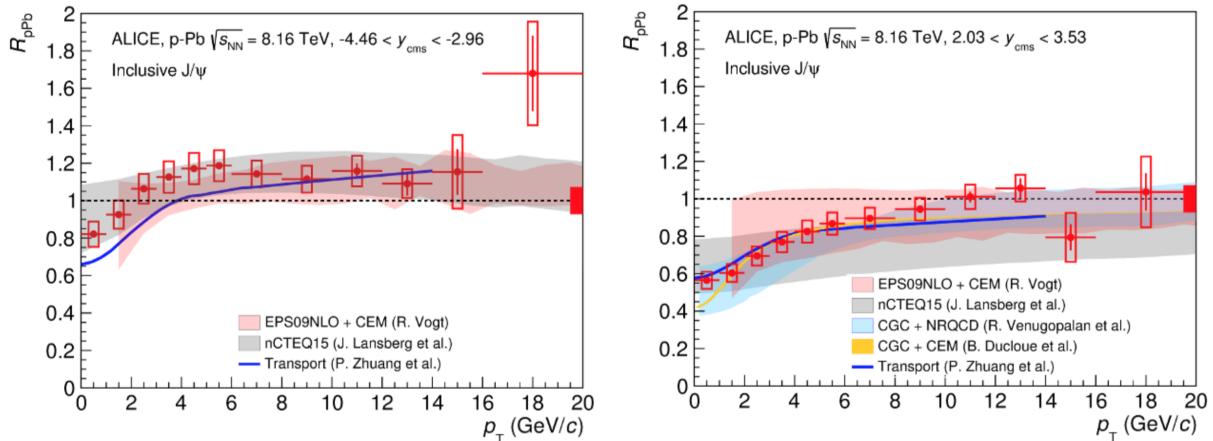

Figure 2.11: Nuclear modification factor of inclusive J/ψ in pPb collisions at $\sqrt{s_{NN}} = 8.16$ TeV as a function of p_T [77] at backward (left) and forward (right) rapidity and compared to theoretical calculations based on EPS09NLO [79] and nCTEQ15 [32] nPDFs, CGC [39, 40] and a transport model [58].

region ($x \sim 5 \times 10^{-2}$) at backward rapidity. The p_T dependences are also well described by those models in the full rapidity interval (see [75] and Fig. 2.11).

There are two calculations based on CGC models. These models assume a dilute-dense configuration where the incoming proton is a dilute system described by the usual PDF and the incoming nucleus is a dense system described within the CGC framework. This hypothesis is only valid at mid- and forward rapidity. For the elementary production model, Ducloué *et al.* [39] uses CEM while Venugoplan *et al.* [40] uses NRQCD. These calculations reproduce well the rapidity and p_T dependence of the data at forward rapidity as it can be seen in Fig. 2.9 and 2.11.

The model from Arleo *et al.* [44] includes effects from parton coherent energy loss. The prompt J/ψ production cross section in pp collisions is parametrised on the world data. In that calculation, it is interesting to note that there is no shadowing/anti-shadowing effect. It gives a good description of the rapidity dependence as it can be seen in Fig. 2.9. The p_T dependence at forward rapidity is steeper in the model (see [75]) than in the data. A better agreement is found when the nPDF from EPS09 NLO is included.

Finally, there are two calculations that include final-state interaction of the $c\bar{c}$ pair with the medium

29
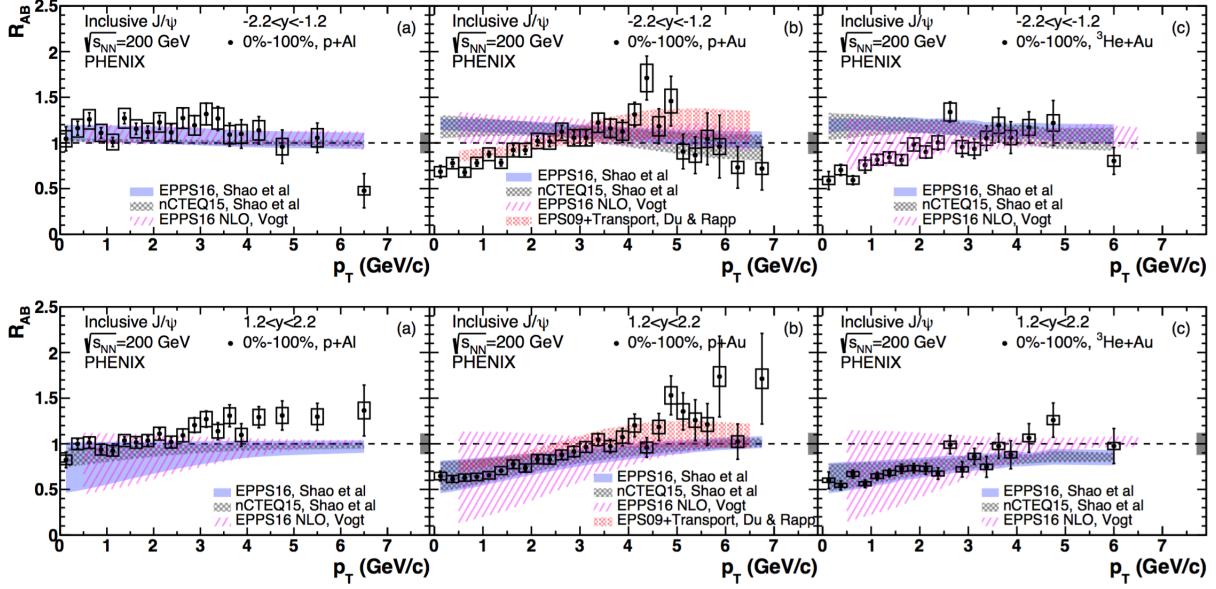
Figure 2.12: Nuclear modification factor of inclusive J/ψ in pAl, pAu and ^{3}HeAu collisions at $\sqrt{s_{NN}} =$ 200 TeV as a function of p_T [52] at backward (top) and forward (bottom) rapidity and compared to nPDFs-based theoretical calculations [79, 32] and a transport model [53].

created in the collision. This medium can be either of partonic or hadronic nature and the models consider the effects from initial and final state can be factorized. The model from Ferreiro [51] uses EPS09 LO nPDF with a comoving hadronic medium. The model from Zhuang *et al.* [58] uses EPS09 NLO sets for the nPDFs to describe cold nuclear matter effect and the transport approach to describe the dissociation of J/ψ in the hot part of the fireball created in central pPb collisions. Both models can reproduce the rapidity dependence of the data, despite different R_{pPb} values at backward rapidity as it can be seen in Fig. 2.9 and 2.11. This final state effect, however, leads to a small suppression of the J/ψ production when integrating over event centrality, while it has a large effect on the $\psi(2S)$ production as we will see later.

It is interesting to compare the J/ψ modification factor measured at LHC to lower energy data, in particular the most recent measurements from PHENIX [52] in pA, pAu and ^{3}HeAu collisions at $\sqrt{s_{NN}} = 200$ TeV, also shown in Fig. 2.12 at backward (top panel) and forward (bottom panel) rapidity. At backward rapidity in pA collisions, the p_T dependence of R_{pA} and its amplitude is very similar for the two energies. For $p_T > 3$ GeV/c, R_{pA} is systematically higher than unity at LHC and not at RHIC. At forward rapidity and low p_T the amplitude of R_{pA} is similar at RHIC and LHC and an increase of R_{pA} with p_T is observed in both cases. However while R_{pA} reaches unity at RHIC at $p_T \sim 3$ GeV/c, it reaches unity at LHC only at larger p_T, $p_T \sim 8$ GeV/c.

The RHIC and LHC data are compared to the same nPDFs models from Lansberg, Shao *et al.* [32] where the nPDFs were reweighted on the LHC data. At forward rapidity, the p_T distribution of R_{pA} is well described by this model at RHIC. This indicates that nPDFs can reproduce the large J/ψ suppression observed at RHIC at forward rapidity coherently with the suppression measured at the LHC. Instead at backward rapidity at $\sqrt{s_{NN}} = 200$ TeV with the Au beam, the nPDF model does not describe the J/ψ suppression for $p_T < 2$ GeV/c. This difference suggests additional effects at backward rapidity and low p_T. In particular, nuclear absorption is expected to be important at backward rapidity at RHIC because the nuclear crossing time is comparable with the charmonium formation time τ_f [47].

The dependence of the nuclear modification factor as a function of event centrality was also measured, where the centrality is estimated from the energy deposited in the zero degree calorimeter. $\langle N_{coll} \rangle$ and $\langle T_{pPb} \rangle$

were calculated according to the Glauber model [66] with the hybrid method, as explained in Section 2.2.3. Figure 2.13 shows Q_{pPb} as a function of the number of binary collisions, $\langle N_{coll} \rangle$, at backward (left plot) and forward (right plot) rapidity at $\sqrt{s_{NN}} = 5.02$ [83] and 8.16 TeV. The data at the highest energy are preliminary. The results at the two energies agree well except for the most peripheral event class at backward rapidity. At backward rapidity, the measured J/ψ production is compatible, within the total uncertainties, with expectations from the binary collision scaling for all centrality classes but the two most peripheral centrality classes at $\sqrt{s_{NN}} = 8.16$ TeV. At both energies, an increase of Q_{pPb} from peripheral to central pPb collisions is observed. At forward rapidity, Q_{pPb} decreases from peripheral to central pPb collisions.
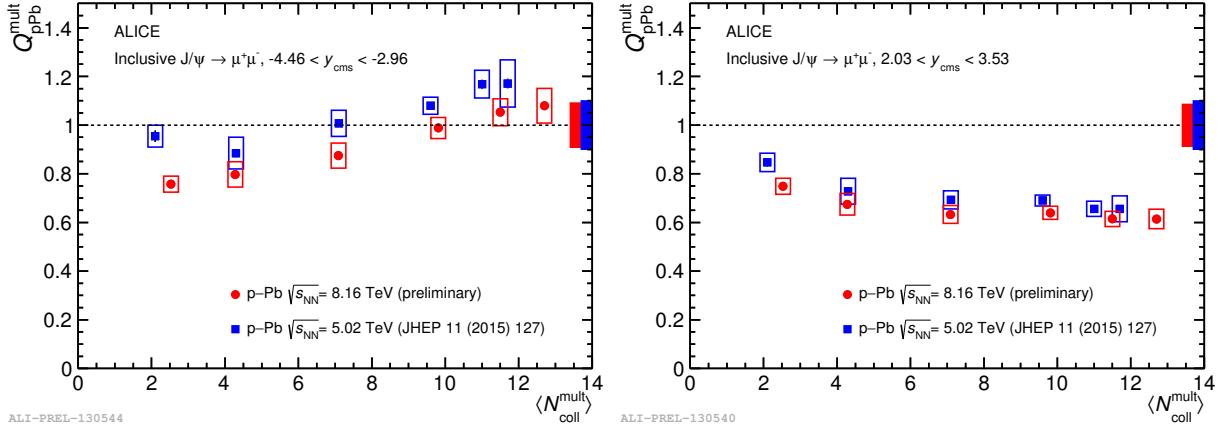

Figure 2.13: Nuclear modification factor of inclusive J/ψ in pPb collisions at $\sqrt{s_{NN}} = 5.02$ [83] and 8.16 TeV as a function of the number of binary collisions at backward (left) and forward (right) rapidity. Data at $\sqrt{s_{NN}} = 8.16$ TeV are preliminary.

Some of the models described above based on shadowing, CGC, coherent energy loss or with final-state interaction reproduce well the Q_{pPb} measurements as a function of event centrality at backward and forward rapidity as shown in Fig. 2.14 or in the corresponding theoretical papers [39, 58]. Note however that most of the models do not describe the increase of Q_{pPb} from peripheral to central pPb collisions as measured in data at backward rapidity. In particular the calculations based on transport model [58] indicate that Q_{pPb} should decrease from peripheral to central pPb collisions if one considers hot and cold nuclear matter effects. The authors of this model conclude that it is not possible to describe both J/ψ and $\psi(2S)$ at backward rapidity.
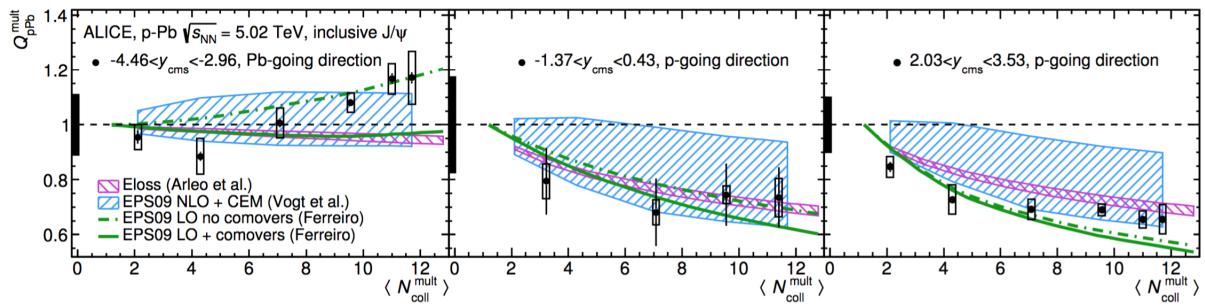

Figure 2.14: Nuclear modification factor of inclusive J/ψ in pPb collisions at $\sqrt{s_{NN}} = 5.02$ [83] as a function of the number of binary collisions at backward (left) mid- (middle) and forward (right) rapidity and compared to theoretical calculations (see text).

In [83], the nuclear modification factor was also measured as a function of p_T for the six centrality

classes defined above. These results show that Q_{pPb} is compatible with unity over the full p_T range at backward rapidity and for the most peripheral collisions at forward rapidity. At forward rapidity and for all the other centrality classes, Q_{pPb} is lower than unity at low p_T, it increases with increasing p_T, and its values at low p_T decrease when going to most central collisions.
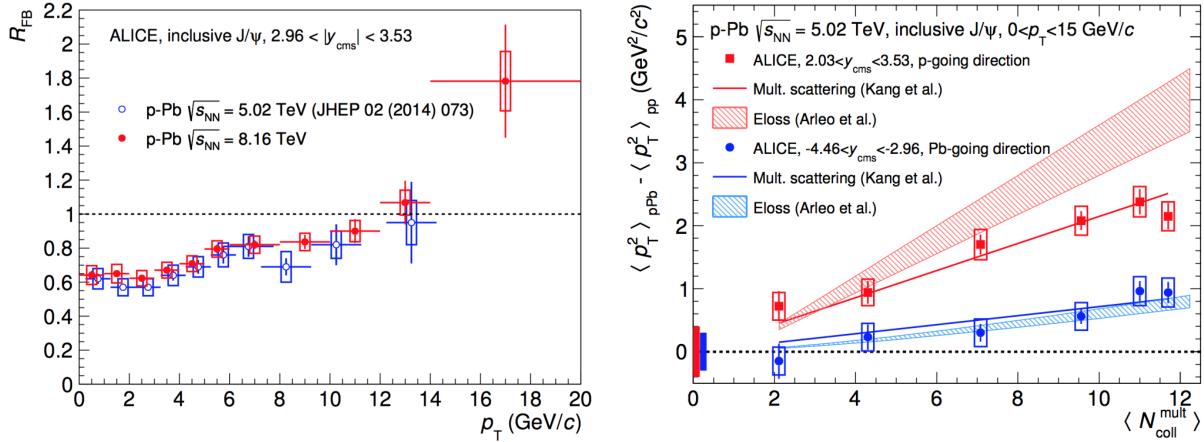

Figure 2.15: Left: forward-to-backward ratio of inclusive J/ψ in pPb collisions at $\sqrt{s_{NN}} = 5.02$ and 8.16 TeV [74, 77] as a function of p_T. Right: p_T broadening as a function of the number of binary collisions at $\sqrt{s_{NN}} = 5.02$ TeV [83].

J/ψ forward-to-backward ratio As discussed previously, the forward-to-backward ratio defined in Eq. 1.11 has the advantage to not rely on σ_{pp} at a cost of a reduced statistics. This observable was measured in pPb collisions at $\sqrt{s_{NN}} = 5.02$ and 8.16 TeV [74, 77]. The left panel of Fig. 2.15 shows the p_T dependence of R_{FB}. The results obtained at different energies agree very well within uncertainties. R_{FB} is lower than 1 at low p_T and increases with increasing p_T. It reaches unity at $p_T \sim 13$ GeV/c.

p_T broadening The p_T broadening, as defined in Eq.1.12, is useful to study the multiple scattering of the partons or the $c\bar{c}$ pair in the nucleus. It was extracted from the p_T-dependent cross sections corresponding to pPb and pp collisions. The p_T dependence of the cross section was parametrised by the empirical function:

$$\frac{\mathrm{d}^2\sigma_{J/\psi}}{\mathrm{d}y\mathrm{d}p_T} = C \times \frac{p_T}{\left(1 + \left(\frac{p_T}{p_0}\right)^2\right)^n} \tag{2.4}$$

where C, p_0 and n are free parameters. The cross sections were fitted by this function in order to obtain the $\langle p_T \rangle$ and $\langle p_T^2 \rangle$ which correspond to the first and second moment of the function, respectively. The uncertainties were obtained by performing fits including only the statistical or the systematic uncertainties on the differential cross sections.

The right panel of Fig. 2.15 shows the p_T broadening as a function of the number of binary collisions at $\sqrt{s_{NN}} = 5.02$ TeV [83]. The $\Delta\langle p_T^2 \rangle$ increases from peripheral to central pPb collisions by 1.1 GeV^2/c^2 and 1.4 GeV^2/c^2 at backward and forward rapidity, respectively. For the most peripheral collisions, corresponding to $\langle N_{coll} \rangle \sim 2$, the $\langle p_T^2 \rangle$ value at backward rapidity is compatible with the one in pp collisions. At forward rapidity, it is found to be larger than in pp collisions by 0.7 GeV^2/c^2. The magnitude of the p_T broadening observed by PHENIX [84] in dAu collisions at $\sqrt{s_{NN}} = 200$ GeV in the backward, mid- and

forward rapidity interval ($|y| < 2.2$) is similar to the one measured by ALICE at backward rapidity. At forward rapidity, ALICE data show a stronger p_T broadening and a steeper increase with increasing centrality as compared to PHENIX.

The data are compared to two theoretical calculations on the right panel of Fig. 2.15 and to one transport model in the corresponding theoretical paper [58]. The first model from Kang *et al.* [85, 86] is based on the LO CEM production model and include initial and final-state multiple scattering of partons with the nuclear medium. In this model, the contribution from final-state multiple scattering on p_T broadening is expected to be sensitive to the colour-octet or colour-singlet nature of the pre-resonant $c\bar{c}$ pair. The calculations are in good agreement with the data at both rapidity intervals. The second model from Arleo *et al.* [81] is based on coherent energy loss by the incoming and outgoing partons and it was described previously. This model describes well the centrality dependence of the p_T broadening at backward rapidity. The $\langle N_{coll} \rangle$ dependence of $\Delta \langle p_T^2 \rangle$ of the model at forward rapidity is steeper than for the data. Finally, while the model from Chen, Zhuang *et al.* [58] can describe the p_T broadening fairly well by including cold and hot nuclear matter, it can not describe the backward rapidity data.

Self-normalised yield as a function of charged particles at mid-rapidity   The self-normalised yields, $dN/dy/\langle dN/dy \rangle$, were measured as a function of the self-normalised charged-particle multiplicity, $dN_{ch}/d\eta/\langle dN_{ch}/d\eta \rangle$, in pPb collisions at $\sqrt{s_{NN}} = 5.02$ [87] and 8.16 TeV. This observable allows one to link the pp, pPb and PbPb measurements as a function of the charged multiplicity measured at mid-rapidity and also to reach higher multiplicity intervals *w.r.t.* the analysis based on the energy deposited in the ZDC [88]. The results are shown in the left panel of Fig. 2.16. An increase of the self-normalised yield with charged-particle multi-
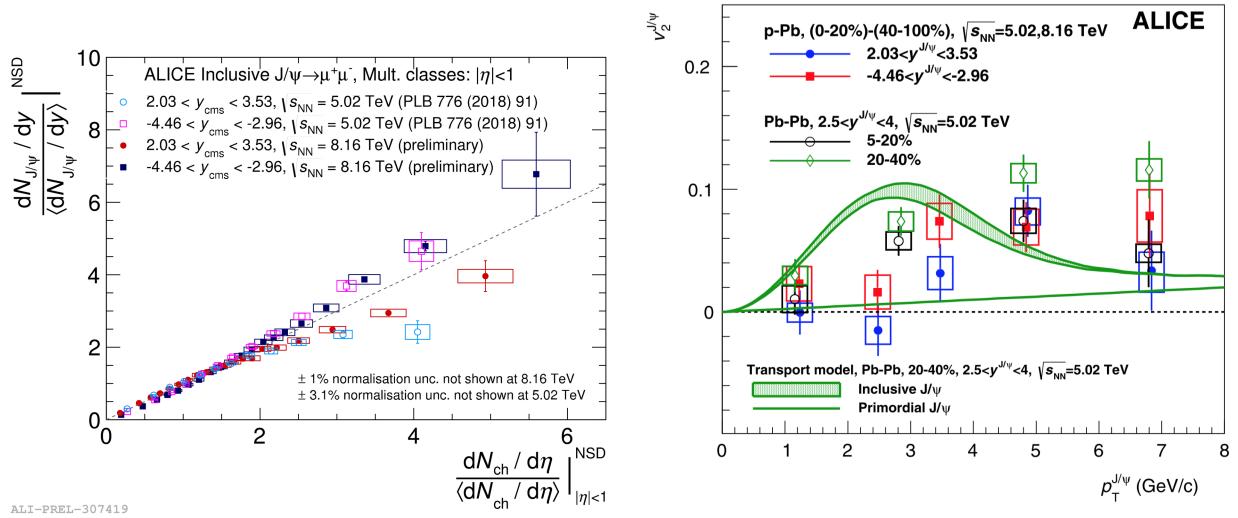
Figure 2.16: Left: self-normalised yield of inclusive J/ψ as a function of self-normalised charged-particle pseudorapidity measured at backward and forward rapidity at $\sqrt{s_{NN}} = 5.02$ [87] and 8.16 TeV. The 8.16 TeV data are preliminary. The dashed line is the first diagonal. Right: elliptic flow, v_2, in pPb and Pbp collisions at backward and forward rapidity combined with the data at $\sqrt{s_{NN}} = 5.02$ and 8.16 TeV [89] and compared to the results obtained in central and semi-central PbPb collisions at $\sqrt{s_{NN}} = 5.02$ TeV [26]. Theoretical calculations from a transport model for semi-central PbPb collisions are also shown (see text) where the green solid line corresponds to the contribution from path-length dependent suppression inside the medium and the band corresponds to the v_2 obtained from recombination of thermalized charm quarks and the feed-down from b-hadron decays with thermalized beauty quarks.

plicity is observed in both rapidity intervals. At low multiplicity, the self-normalised yield increases linearly

with the charged-particle multiplicity in both rapidity intervals. At multiplicities beyond 1.5-2 times the event-average multiplicity, two different behaviours are observed. While at backward rapidity, the increase is similar as in pp collisions at forward rapidity at $\sqrt{s} = 7$ TeV [90] and seems to follow a linear dependence, it has a slower increase at forward rapidity. This slower increase is compatible with CNM effects that reduced the J/ψ production yield at forward rapidity and more importantly for central pPb collisions, as seen in the R_{pPb} measurements.

J/ψ elliptic flow The measurements of angular correlations between particles produced in hadron and nucleus collisions is a powerful tool to study the particle production mechanism. Long-range correlations have been measured in high-multiplicity pp [91] and pPb [92, 93, 94] collisions for charged hadrons. From studies using multiple-particle correlations [54, 55, 56], these long-range correlations are attributed to collective effects. Also it has been found that these measurements in small systems have common features [95, 96] (p_{T} and particle-mass dependencies of the v_n coefficients) with the measurements obtained in PbPb collisions, where they are usually interpreted as signatures of collective particle flow produced during the hydrodynamic evolution of the hot fireball (see *e.g.* [97]). This similarity between small systems and PbPb collisions suggests a common hydrodynamic origin of the observed correlations. Alternative interpretations based on CGC based models [98] and final-state parton scattering [99] have also been proposed to explain these correlations.

The angular correlations between forward and backward J/ψ and mid-rapidity charged hadrons were also studied in pPb collisions at $\sqrt{s_{NN}} = 5.02$ and 8.02 TeV [89]. At mid-rapidity, the charged-hadrons yield associated to a J/ψ was estimated from the SPD tracklets, allowing to probe a pseudorapidity difference between the J/ψ and the tracklets in the range $1.5 < |\Delta\eta| < 5$. The J/ψ second-order Fourier azimuthal coefficient, or elliptic flow, $v_2^{\text{J}/\psi}\{2, \text{sub}\}$, was estimated by subtracting the associated tracklet yields per dimuon trigger at low event multiplicity to the one obtained at high multiplicity, by obtaining the J/ψ yield from the dimuon yield and by extracting the J/ψ v_2 from the J/ψ-tracklet v_2. The J/ψ elliptic flow is found to be positive for $3 < p_{\text{T}} < 6$ GeV/c. The results, shown in the right panel of Fig. 2.16, are compared to the values obtained in PbPb collisions at $\sqrt{s_{NN}} = 5.02$ TeV. In PbPb collisions, the v_2 amplitudes reach similar values than in pPb collisions.

The data are also compared to calculations from a transport model [59] for semi-central PbPb collisions. The solid line corresponds to the contribution of primordial J/ψ inside the medium from path-length dependent suppression only. The band includes the contribution from primordial J/ψ as well as from thermalized charm quarks that recombine into J/ψ and the feed-down from b-hadrons assuming a thermalization of beauty quarks. The model reproduces well the data at $p_{\text{T}} < 4$ GeV/c but do not reproduce the magnitude of the $v_2^{\text{J}/\psi}$ above that value. In pPb collisions, the $v_2^{\text{J}/\psi}$ is expected to be null, as observed for $p_{\text{T}} < 3$ GeV/c, since the amount of produced charm quarks is small and the contribution from charm recombination should be negligible. However the comparable magnitude of the $v_2^{\text{J}/\psi}$ coefficients at high p_{T} in pPb and PbPb may indicate that a similar mechanism is at play in both collision systems.

2.3.2 $\psi(2S)$ **results**

According to most of the CNM-based models such as nPDF and gluon saturation models, or multiple scattering and energy loss models, the effects of the CNM on the $\psi(2S)$ should be similar to those on the J/ψ since these effects mainly depend on the $c\bar{c}$ pair production and the mass of the final particle. Final-state effect such as absorption predicts a larger suppression for the $\psi(2S)$ when crossing the nuclear matter due to its larger binding radius. However this is not expected at the LHC energy because the charmonium formation time τ_f is larger than the nuclear size, as it was discussed in Section 1.4.4. In order to describe the relative $\psi(2S)$ to J/ψ suppression measured at RHIC, models that include final-state effects from a comoving medium and/or from hot nuclear matter in pA collisions were proposed.

Double ratio $\psi(2S)$/J/ψ Experimentally, it is convenient to extract the ratio of $\psi(2S)$ over J/ψ since many terms, and their uncertainties, related to the efficiencies and luminosity, cancel out in the ratio. The double ratio of the $\psi(2S)$ to J/ψ production cross sections is defined as:

$$R = \left[\sigma_{\psi(2S)}/\sigma_{\text{J/}\psi}\right]_{\text{pPb}} / \left[\sigma_{\psi(2S)}/\sigma_{\text{J/}\psi}\right]_{\text{pp}}. \tag{2.5}$$

The double ratio is shown on the left panel of Fig. 2.17 at backward and forward rapidity in pPb collisions at $\sqrt{s_{NN}}$ = 5.02 TeV [100] and is compared to the mid-rapidity measurement of PHENIX obtained in dAu collisions at $\sqrt{s_{NN}}$ = 200 GeV [28]. The production of $\psi(2S)$ is suppressed relatively to that of J/ψ in both rapidity ranges and by up to a factor 2 at backward rapidity and at $\sqrt{s_{NN}}$ = 5.02 TeV, suggesting nuclear matter final-state effects.


ALI-PREL-137063
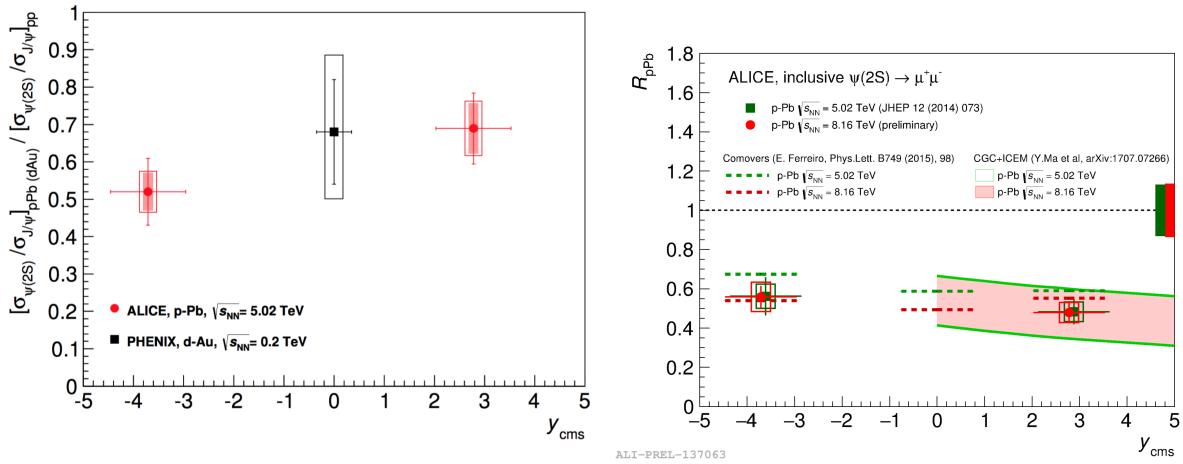
Figure 2.17: Left: Double ratios of $\psi(2S)$ over J/ψ at $\sqrt{s_{NN}}$ = 5.02 TeV in pPb collisions [100], compared to the results obtained at PHENIX at $\sqrt{s_{NN}}$ = 200 GeV in dAu collisions [28]. Right: Nuclear modification factor of $\psi(2S)$ at $\sqrt{s_{NN}}$ = 5.02 [100] and 8.16 TeV in pPb collisions and compared to theoretical calculations (see text). The data at 8.16 TeV are preliminary.

The latest measurements from PHENIX in pp and p (or light nucleus)-A collisions at backward and forward rapidity [52] are also shown in Section 1.4.4 in the left panel of Fig. 1.8 . While at backward rapidity, the $\psi(2S)$ production is suppressed relatively to the J/ψ, this is not the case at forward rapidity as observed at the LHC. In a comover approach, this is expected since the charged-particle density is much lower at forward rapidity at RHIC than at LHC energy.

$\psi(2S)$ **nuclear modification factor**   The nuclear modification factor was also extracted in pPb collisions at $\sqrt{s_{NN}}$ = 5.02 [100] and 8.16 TeV. The right panel of Fig. 2.17 shows R_{pPb} as a function of rapidity and its comparison with two theoretical models that include final-state effects. The results obtained at two different energies are compatible, those obtained at $\sqrt{s_{NN}}$ = 8.16 TeV having a better statistical accuracy. The $\psi(2S)$ production in pPb collisions *w.r.t.* its normalised production in pp collisions is suppressed by 40% at backward rapidity and 50% at forward rapidity.

The calculations from a comover model from Ferreiro [51] represented by dashed lines reproduce well the $\psi(2S)$ R_{pPb} in both rapidity range. The model predicts a stronger suppression at $\sqrt{s_{NN}}$ = 8.16 TeV due to a larger charged-particle multiplicity at 8.16 TeV. This effect can not be confirmed or ruled out by the data given the size of the effect and the uncertainties of the data. The second model from Ma *et al.* [41] includes soft-color exchanges between the $c\bar{c}$ pair undergoing hadronisation and comoving partons that are long-lived on time scales of quarkonium suppression. The soft-color exchanges suppress the $\psi(2S)$ production

relatively to the J/ψ one. These calculations are based on the CGC framework coupled to an improved CEM model for the hadronisation of charmonia. The dense-dilute hypothesis used in the CGC framework makes the model valid only at mid- and forward rapidity.

The $\psi(2S)$ R_{pPb} was also measured as a function of rapidity and p_T in ALICE. Within the data uncertainties, no dependence as a function of p_T was observed [100]. At large p_T, ATLAS and CMS also measures the $\psi(2S)$ production in pPb collisions [101, 102]. In particular, CMS found a significant suppression of the $\psi(2S)$ up to 40% at $y_{cms} \sim -2$ for $4 < p_T < 10$ GeV/c and a relative suppression of the $\psi(2S)$ w.r.t. J/ψ at backward rapidity in the same p_T interval.

The event centrality dependence was also studied. Figure 2.18 shows Q_{pPb} as a function of event centrality at backward (left panel) and forward (right panel) rapidity, as determined from the energy deposited in the ZDC in ALICE [83]. In both rapidity intervals, no significant $\langle N_{coll} \rangle$ dependence of Q_{pPb} is observed within the data uncertainties. However, the large uncertainties do not allow to draw a firm conclusion. The data are compared to two theoretical models. The first model is based on final-state effects from a comoving medium from Ferreiro [51] as shown in the right panel of Fig. 2.17, that can fairly well describe Q_{pPb} in both rapidity intervals. The second model is based on a transport approach from Du et al. [59, 53] that assumes hot fireballs are created in the most central collisions in pA collisions. It reproduces fairly well the $\psi(2S)$ Q_{pPb} despite some tension at low $\langle N_{coll} \rangle$ at backward rapidity. Another transport model from Chen et al. [58] gives a good description of the $\psi(2S)$ R_{pPb} but a larger suppression of the J/ψ at backward rapidity and central collisions.
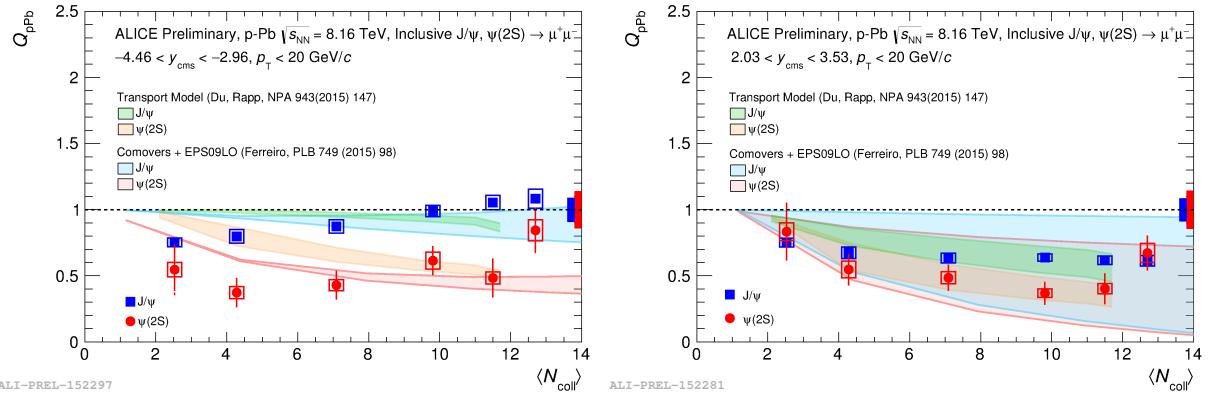

Figure 2.18: Nuclear modification factor of J/ψ and $\psi(2S)$ at $\sqrt{s_{NN}} = 5.02$ [83] and 8.16 TeV in pPb collisions as a function of centrality at backward (left) and forward (right) rapidity and compared to two theoretical calculations (see text). The data at $\sqrt{s_{NN}} = 8.16$ TeV are preliminary.

2.3.3 Open heavy-flavour and bottomonium measurements and implication for charmonia

Charm production Open charm production is of great importance when studying charmonium production since it gives access to the $c\bar{c}$ pair production cross section. An access to the total open charm production in pPb collisions would allow one to disentangle the nuclear effects on the $c\bar{c}$ pair production to those on the charmonium state formation. Studying nuclear effects on open charm production also constrain the various models that are used to describe charmonium production.

Open heavy flavour production can be described by pQCD calculations as a convolution of the PDFs of the incoming nucleons, the hard scattering production of the $c\bar{c}$ pair and the fragmentation function. The latter parametrises the non-perturbative evolution of a charm quark into a given heavy-flavour hadron species. Theoretical calculations based on pQCD (GM-VFNS [103] and FONLL [9]) describe generally well the measured charm cross-section within uncertainties. Open charm cross-sections were usually extracted

from the D^0 meson cross section by using the fraction of charm quark hadronising into D^0 mesons from e^+e^- collisions measurements at LEP [104]. However, recent Λ_c-baryon measurements in pp collisions at $\sqrt{s}$ = 7 TeV and pPb collisions at $\sqrt{s_{NN}}$ =5.02 TeV [105, 106] suggest that the fragmentation of charm quarks into charmed baryons in pp collisions at LHC energy differs from the LEP results and therefore that the fragmentation function is not universal as assumed in the factorisation approach of open charm production. In order to extract the total charm production cross section, one then needs to rely on more precise measurements of charmed-baryon production cross sections at the LHC. Λ_c represents about 6% of charm quark fragmentation as measured by LEP [104].

The left panel of Fig. 2.19 shows the nuclear modification factor of prompt D mesons (average values of the three non-strange D mesons (D^0, D^+ and D^{*+}) as a function of p_T as measured by ALICE at $\sqrt{s_{NN}}$ = 5.02 TeV. R_{pPb} is compatible with unity over the full p_T interval within 2 σ. The values integrated over p_T is: R_{pPb} = 0.96 ± 0.05 (stat) ± 0.07 (syst) for −0.96 < y_{cms} < 0.04. It is interesting to compare this value to the one obtained for inclusive J/ψ in the same rapidity range: R_{pPb} = 0.71 ± 0.06 (stat) ± 0.13 (syst) [75]. At mid-rapidity, the J/ψ R_{pPb} is lower than that of D meson however uncertainties are large and both measurements are compatible within 1.5 σ. The right panel of Fig. 2.19 presents the nuclear modification factor of prompt D^0 mesons as a function of rapidity as measured by LHCb at $\sqrt{s_{NN}}$ = 5.02 TeV. The nuclear modification factor depends on rapidity. While the D^0 meson production is suppressed w.r.t. its normalised production in pp collisions at forward rapidity, it is compatible with unity for −4 < y_{cms} < −2.5 and is enhanced at y_{cms} < −4. Note that LHCb has measured the cross sections for D^0 mesons in a larger rapidity range by half a unit but did not extra/interpolate the pp cross section out of the measured rapidity range, leading to a reduced rapidity measurement for R_{pPb}. The LHCb prompt J/ψ R_{pPb}, indicated in blue in the figure, is consistent with that of prompt D^0, suggesting that initial state effects are the dominant ones for J/ψ production. The rapidity dependence of the D^0 R_{pPb} is well described by nPDF models based on EPS09NLO and nCTEQ15 from Lansberg et al. [82]. The CGC models from Ducloué et al. [38] and Fuji et al. [107] reproduce the measurements in the forward rapidity interval. The first model computes the uncertainties from charm quark mass and factorisation scale only, hence the reduced uncertainty.
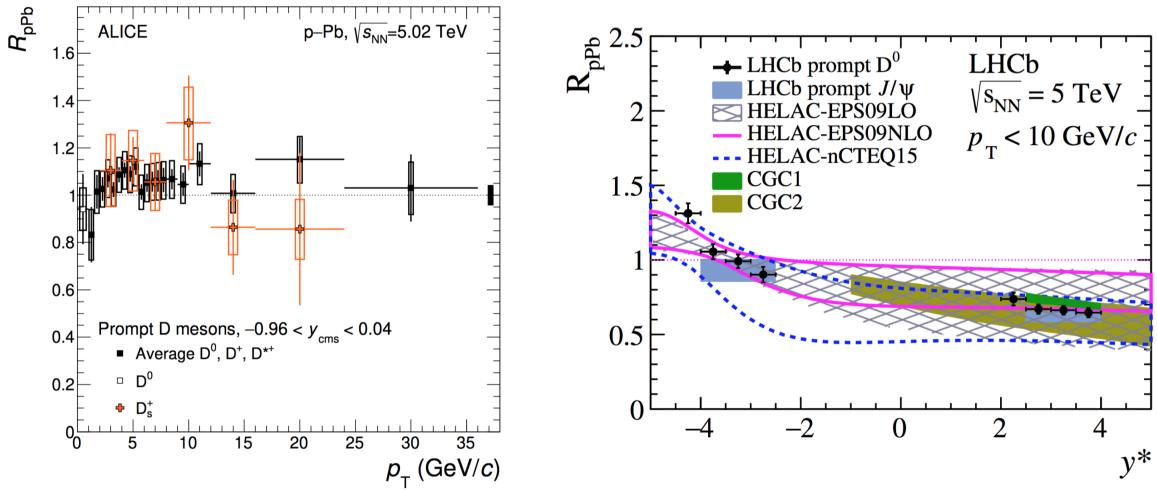
Figure 2.19: Nuclear modification factor of D mesons at $\sqrt{s_{NN}}$ = 5.02 TeV in pPb collisions as a function of p_T at mid-rapidity [108] (left) and as a function of rapidity at backward/forward rapidity (right) [109].

Figure 2.20 shows the inclusive and prompt J/ψ R_{pPb} integrated over p_T and as a function of rapidity obtained at $\sqrt{s_{NN}}$ = 5.02 and 8.16 TeV in pPb collisions and compared to D mesons at $\sqrt{s_{NN}}$ = 5.02 in pPb collisions. Since the J/ψ results at the two energies are compatible, the 8.16 TeV results are added as well

in this compilation figure since they are more precise than the 5.02 TeV ones and they extend the rapidity range. The J/ψ R_{pPb} is compatible with the J/ψ one for $-4 < y_{cms} < 4$ and this suggests that initial state are the dominant nuclear effects in pPb collisions for J/ψ production in this rapidity interval. It differs by 3.8 σ for $-4.5 < y < -4$ when considering LHCb data only, pointing out final-state effect for J/ψ production. It will be helpful in the future to increase the precision of these measurements and to extend the J/ψ ones at backward rapidity (an additional point could be measured from LHCb) to confirm/infirm the similarity and difference between J/ψ and D meson production in pPb collisions. Since the backward/forward rapidity data are dominated by systematic uncertainty, it could help to measure the pp cross section at the correct energy or to evaluate directly the ratio of the two measurements within the same experiment. A comparison as a function of the collision centrality would be very helpful as well.
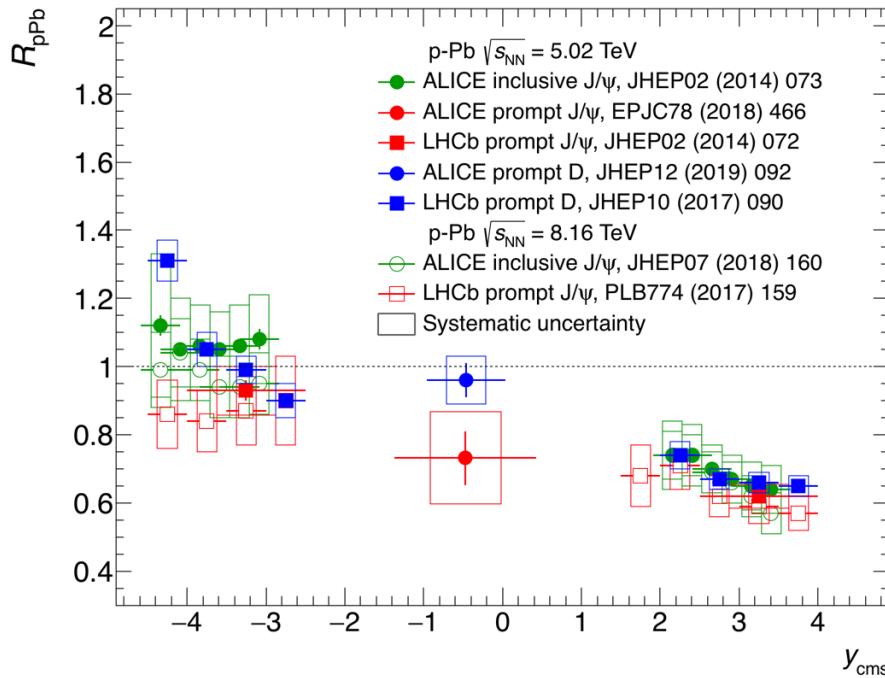
Figure 2.20: Nuclear modification factor of J/ψ at $\sqrt{s_{NN}} = 5.02$ and 816 TeV in pPb collisions as compared to D mesons at $\sqrt{s_{NN}} = 5.02$ in pPb collisions as a function of rapidity and integrated over p_T from ALICE and LHCb.

Beauty production   Open beauty and bottomonium measurements in pPb collisions allow one to probe the nuclear matter effects at a different mass scale than with open charm and charmonium production: the higher beauty quark mass is expected to lead to different effect amplitudes. Excited bottomonium states can also be measured and compared to the ground state as done in the case of the ψ(2S). In the following, we will discuss the bottomonium results and will compare them to the charmonium measurements. The open beauty measurements from non-prompt J/ψ will be also discussed.

Figure 2.21 shows the nuclear modification factor of Υ(1S) in pPb collisions as a function of rapidity as measured in ALICE and LHCb at $\sqrt{s_{NN}} = 8.16$ TeV [110, 111] (left) and ATLAS and CMS at $\sqrt{s_{NN}} = 5.02$ TeV [112, 101] (right). In the right panel, the data from ALICE and LHCb are also added for completeness. The Υ(1S) is suppressed in pPb collisions in particular at mid and forward rapidity. Given the uncertainties of the measurements, no significant rapidity dependence of R_{pPb} is found as for the J/ψ.

Figure 2.22 shows the p_T dependence of the Υ(1S) R_{pPb} at backward (left) and forward (right) rapidity.
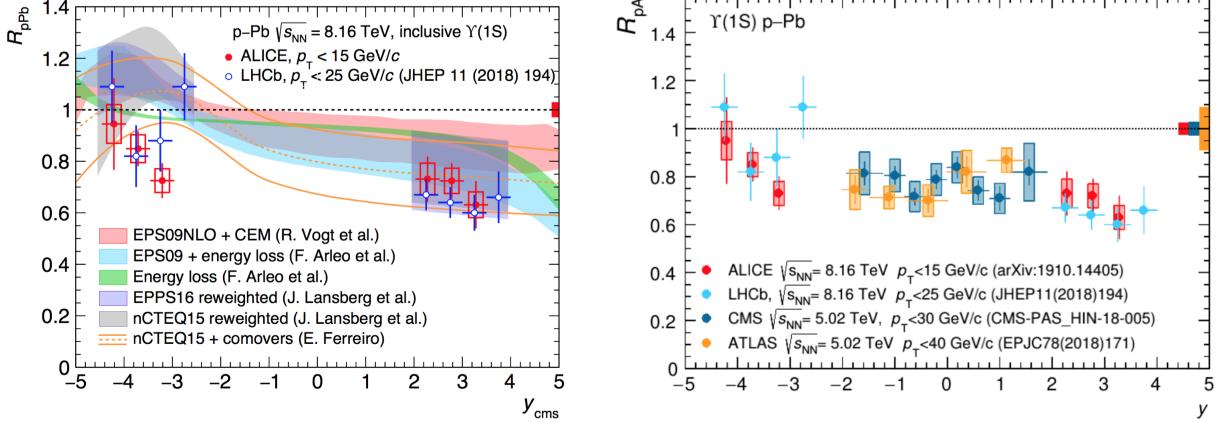
Figure 2.21: Left: nuclear modification factor of $\Upsilon(1S)$ at $\sqrt{s_{NN}} = 8.16$ TeV in pPb collisions as a function of rapidity from ALICE [110] and LHCb [111]. Right: nuclear modification factor of $\Upsilon(1S)$ in pPb collisions at $\sqrt{s_{NN}} = 5.02$ TeV from ATLAS [101] and CMS [112] and at $\sqrt{s_{NN}} = 8.16$ TeV from ALICE [110] and LHCb [111] as a function of rapidity.

A decrease of the nuclear modification factor with decreasing p_T is observed at both rapidity intervals. At $p_T > 8$ GeV/c, R_{pPb} is consistent with unity. R_{pPb} is also found to be consistent with unity by ATLAS for $15 < p_T < 40$ GeV/c at mid-rapidity at $\sqrt{s_{NN}} = 5.02$ TeV [101].
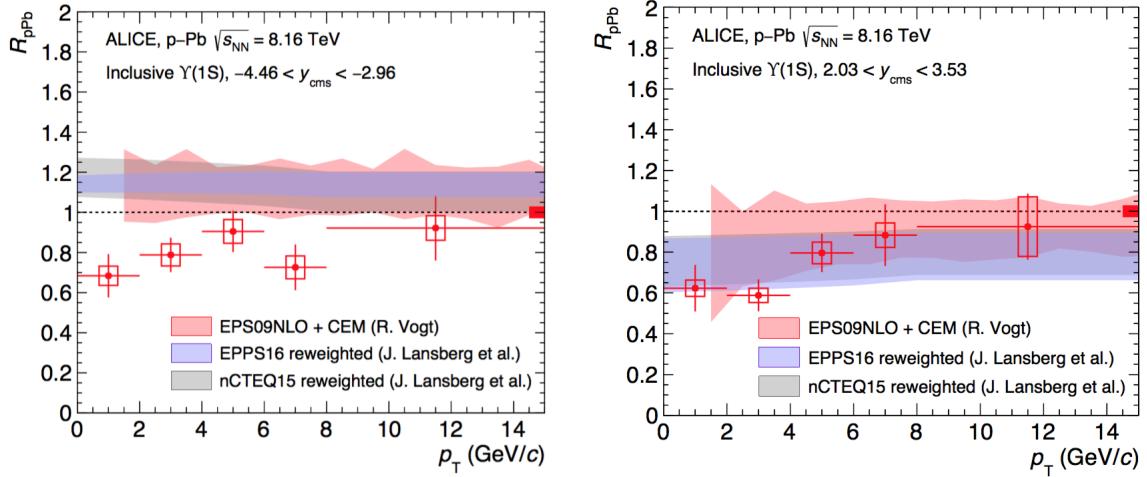
Figure 2.22: Left: nuclear modification factor of $\Upsilon(1S)$ at $\sqrt{s_{NN}} = 8.16$ TeV in pPb collisions as a function of p_T at backward (left) and forward (right) rapidity [110].

In the left panel of Fig. 2.21 and in both panels of Fig. 2.22, some of the models that describe the J/ψ R_{pPb} in Fig. 2.9 are compared to the $\Upsilon(1S)$ measurements. The models based on nPDFs (denoted EPS09NLO from Vogt [79], "EPPS16 reweighted" and "nCTEQ15 reweighted" from Lansberg *et al.* [82] in Fig. 2.21 and 2.22) reproduce well the p_T and rapidity dependence of the $\Upsilon(1S)$ R_{pPb} at forward rapidity. However they overestimate R_{pPb} at backward rapidity and they do not reproduce the p_T dependence of the ALICE measurements. The rapidity dependence measurement is also compared to a model that includes the effects from coherent energy loss from Arleo *et al.* [81]. When the model does not include the contribution from nPDF, it overestimates the ALICE measurement for almost the full rapidity range, while it reproduces well

the rapidity dependence of the J/ψ R_{pPb} over the full rapidity range. When the contribution from nPDF is included (with EPS09), the Υ(1S) R_{pPb} is well reproduced by the coherent energy loss model at forward rapidity.

As for charmonium production, most of the models (nPDF, coherent energy loss, CGC) do not predict a lower R_{pPb} for the excited states of the bottomonium family. The LHC experiments (ALICE [110], ATLAS [101], CMS [113, 112] and LHCb [110]) have however found a larger suppression of the excited state Υ(2S) and Υ(3S) productions relatively to the Υ(1S) bound state one at $\sqrt{s_{NN}}$ = 5.02 and 8.16 TeV in pPb collisions. Figure 2.23 shows the double ratio of the Υ(2S) (left panel) and the Υ(3S) (right panel) to the Υ(1S) production cross sections, as defined in Eq. 2.5, at backward and forward rapidity at $\sqrt{s_{NN}}$ = 8.16 TeV in pPb collisions as measured by LHCb [110]. The excited states are systematically more suppressed than the ground state. In particular, the double ratio shows a stronger suppression for Υ(3S) than Υ(1S) at backward rapidity. The data are compared to calculations based on final-state effects from a co-moving medium [51, 114] that reproduce well the relative suppressions of the Υ(2S) and Υ(3S) w.r.t. Υ(1S) at backward and forward rapidity.
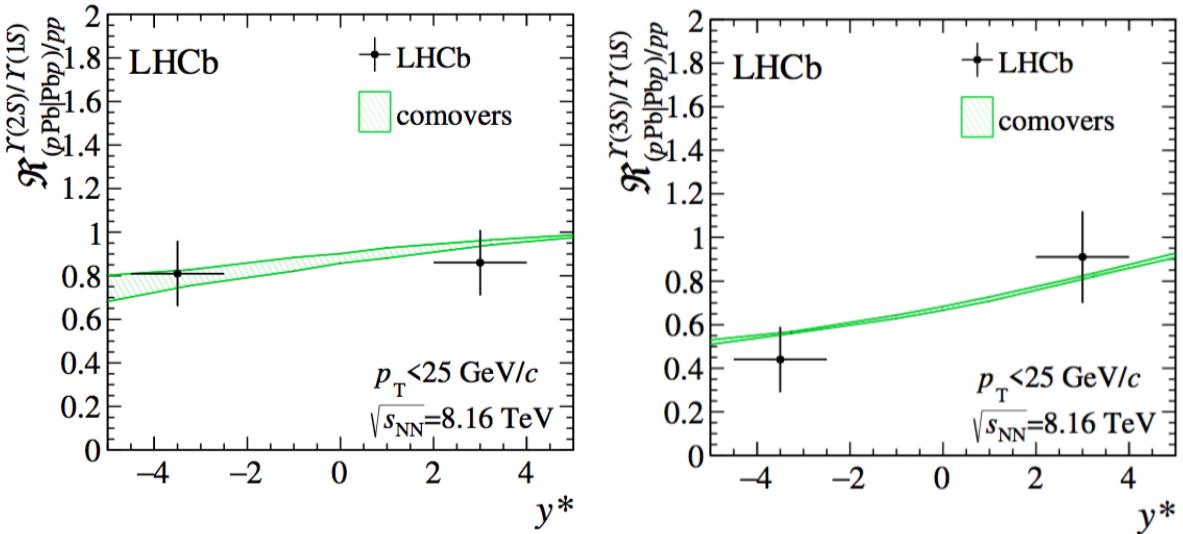
Figure 2.23: Double ratio of Υ(2S) (left) and Υ(3S) (right) over Υ(1S) in pPb and pp collisions at $\sqrt{s_{NN}}$ = 8.16 TeV as a function of rapidity [110].

As for the charm case, it is valuable to compare the bottomonium cross sections to the open beauty ones. Figure 2.24 shows the ratio of the Υ(1S) to the non-prompt J/ψ cross sections as a function of rapidity in pPb collisions at $\sqrt{s_{NN}}$ = 8.16 TeV and in pp collisions at $\sqrt{s}$ = 8 TeV [110]. The ratio is systematically lower in pPb collisions at forward rapidity. As discussed previously on the charm sector, a larger suppression of the J/ψ to the D meson R_{pPb} is not observed (see the left panel of Fig. 2.19). More data will allow one to confirm if there is a different suppression mechanism for bottomonium and open beauty in pPb collisions at the LHC energy.
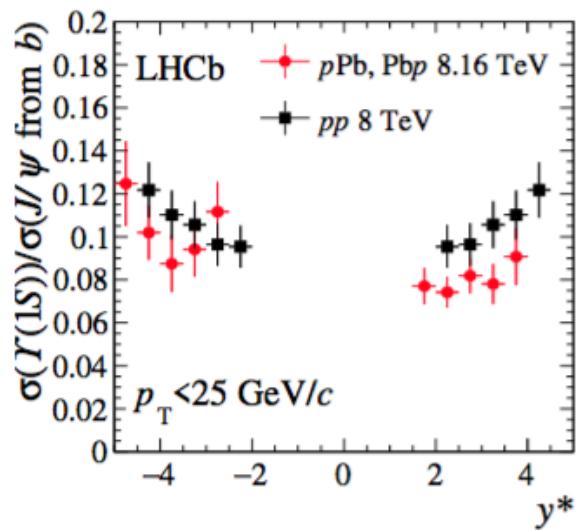
Figure 2.24: Ratio of $\Upsilon(1S)$ to non-prompt J/ψ cross sections as a function of rapidity in pPb collisions at $\sqrt{s_{NN}} = 8.16$ TeV and pp collisions at $\sqrt{s} = 8$ TeV [110].

Chapter 3

Opportunities for charmonium production in pA collisions in a fixed-target mode at the LHC

Fixed-target experiments offer the possibilities to reach high luminosities with dense target and to use various target types, as well as polarised targets. Fixed-target experiments can be achieved with accelerators that run in collider mode, as in the past with HERA at DESY and with the Tevatron at Fermilab, and currently with RHIC at BNL. In the early 90's, there were two LHC fixed-target projects dedicated to *b*-physics (GAJET and LHB). These projects were in competition with a third one on the same physics topic but running in collider mode. The third project was chosen and finally became the LHCb experiment. Later, the physics opportunities to run a fixed-target experiment with the LHC beams were discussed in [115, 116] and several technical implementations were proposed, in particular with the ALICE and LHCb detectors. The expected performances of a fixed-target programme using the proton and ion beams of the LHC were further studied within the AFTER@LHC study group and reviewed in [117]. In the following, the general physics motivations for fixed-target experiments at the LHC will be presented, as well as the possible implementations at the LHC. Finally the physics opportunities and expected performances in the case of charmonium production in pA collisions will be discussed.

3.1 Main motivations for a fixed-target experiment at the LHC at high luminosity

The 7 TeV proton and 2.76 A TeV lead beams at the LHC allow one to reach a center-of-mass energy per nucleon pair of $\sqrt{s_{NN}} = 115$ GeV and $\sqrt{s_{NN}} = 72$ GeV, respectively. These energies correspond to an energy domain between SPS and nominal RHIC energies. The interaction of proton beam with a target leads to a rapidity boost of 4.8 units, while the rapidity boost is of 4.2 units in case of the lead beam. This implies that the mid- to forward rapidity region in the center of mass frame ($y_{cms} \geq 0$) lies within 1 degree in the laboratory frame and that the backward region ($y_{cms} \leq 0$) is easily accessible by using standard experimental techniques or existing detectors such as those of ALICE or LHCb. The fixed-target mode offers thus the opportunity to access the backward rapidity domain that can be linked to the high-*x* frontier of the nucleon and nuclear internal structure, where *x* is the momentum fraction of the parton struck in a target nucleon or nucleus.

The physics motivations of a fixed-target experiment at the LHC are three-fold [116, 118, 119, 120, 117]: advance our understanding of the high-*x* gluon, antiquark and heavy-quark content in the nucleon

and nucleus, unravel the spin structure of the nucleon, and study the quark-gluon plasma (QGP) created in heavy-ion collisions towards large rapidity. In the following, these three main motivations will be briefly discussed.

3.1.1 High-x frontier

As illustrated by the uncertainties on the gluon nuclear modification factor shown on the right panel of Fig. 1.5, the gluon distribution in nuclei is barely known at large-x. This is also the case of the gluon distribution in the nucleon. At large x, there are also long-standing puzzles such as the non-perturbative source of charm and beauty quarks in the proton which would carry a non negligible fraction of its momentum. Accessing the high-x gluon in a nucleon, where gluon carries most of the nucleon momentum would test the QCD in a new limit, not explored so far. Studying the high-x distribution of the quarks and gluons in proton and nuclei is also crucial to improve the knowledge of the parton luminosities at hadron colliders for the production of high-mass particles and ultra high energy cosmic rays.

For nucleus targets, the atomic mass dependence can give important input to study the EMC effects and understand how quarks and gluons behave in the nuclear medium. Using deuteron and ^{3}He targets would provide access to the parton distribution functions in a neutron and allow one to check the assumptions usually made for light quarks based on isospin symmetry. Also it can be used to test if the gluon distribution is similar in a proton and a neutron.

The left and right panel of Fig. 3.1 illustrates the target x range (denoted x_2 or x_{target} in the following) covered by the LHCb (left) and ALICE muon spectrometer (right) detectors if used in a fixed target mode in the case of open and hidden heavy-flavour measurements. By measuring quarkonium and open heavy flavour production as a function of rapidity and p_T, one could access the high-x frontier of the gluon distribution at relatively low scale, represented here by the hadron transverse mass. To access the light quark distribution functions in the nucleon and nucleus at low scale, the golden process in hadronic collisions is the Drell-Yan one. Studies carried out in [117] show that Drell-Yan measurements with a LHCb-like detector in a fixed-target mode would allow one to constrain the quark and antiquark distributions at moderate and high-x. Note that for these measurements, a high luminosity with a hydrogen target (*i.e.* $\mathcal{L}_{pp} = 1 - 10$ fb^{-1}) would be required since the cross section decreases towards the backward rapidity region, *i.e.* towards the end of the process phase-space.

3.1.2 Nucleon spin structure

The spin internal structure of the nucleon is still largely unknown despite many precise measurements in Deep Inelastic Scattering (DIS) and Semi-Inclusive DIS (SIDIS). Nowadays, it is not clear how the quarks and gluons bind into a spin-$\frac{1}{2}$ object. The nucleon spin can arise from the intrinsic spin of the quarks and the gluons but also from their Orbital Angular Momentum (OAM), not yet measured. There is still a long experimental way to resolve the so-called spin puzzle which consists now in determining how large the different contributions of the quarks and the gluon to the nucleon spin are. In order to measure the parton OAM, one should access observables that are sensitive to the parton position and momentum. This can be carried out with the extraction of the Generalised Parton Distributions from the measurements of exclusive processes where the final state is fully determined. One can also indirectly access information on the orbital motion of the partons via Single-Spin Asymmetries (SSA) in different hard processes in SIDIS or hadronic collisions, and in particular with a transversally polarised nucleon.

Experimentally, one can measure Single Transverse-Spin Asymmetries (STSA) which gives access to the left-right asymmetries of the parton distributions with respect to the plane formed by the proton momentum and the spin direction. These STSA are related to the transverse motion of the partons inside the polarised nucleons. In the approach of the Transverse-Momentum Dependent (TMD) factorisation, the TMD PDFs
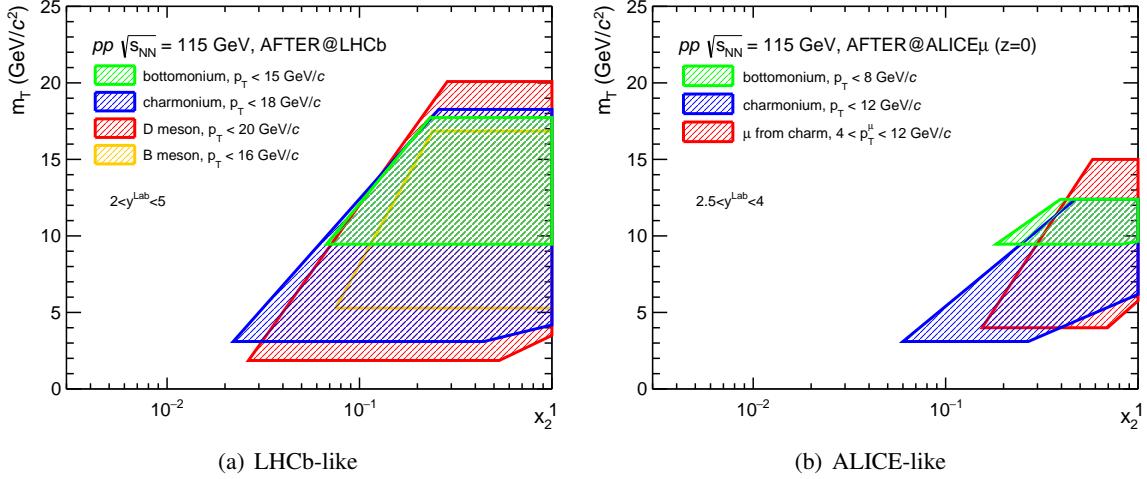
Figure 3.1: Typical kinematical reach with heavy-hadron production in x_{target} (momentum fraction of the parton in the target) and the hadron transverse mass of the fixed-target mode with a detector acceptance like (a) LHCb and (b) ALICE [117]. The transverse mass is chosen to be $m_T = \sqrt{M^2_{\text{hadron}} + p^2_{T,\text{hadron}}}$.

such as the Sivers function, that can be extracted from STSA measurements, encode the possible spin-spin and spin-orbit correlations between the hadron and its constituents.

By using the proton beam of the LHC on a polarised transverse hydrogen, deuterium and/or ^{3}He target, one could achieve Drell-Yan STSA measurements, allowing one to constrain the Sivers function for light quarks. In particular, the TMD factorisation predicts a sign change of the STSA in SIDIS and Drell-Yan processes that could be tested in the kinematic range accessible at the LHC in a fixed-target mode. On the other hand, heavy-flavour and quarkonium STSA measurements would allow one to probe the transverse dynamics of gluons. These measurements would be complementary to the SIDIS measurements performed by COMPASS. By accessing the backward rapidity region, such measurements would probe the range of parton at high momentum fraction x in the polarised target.

3.1.3 Quark gluon plasma

With the lead beam of the LHC, one could explore the nuclear medium created in Pb-A collisions at $\sqrt{s_{NN}} = 72$ GeV. At this energy, the medium created in the collision is expected to have a low baryon chemical potential (μ_B) and a temperature (T) approximately 1.5 times higher than the critical temperature of the phase transition between a hadron gas and a QGP [15]. The Beam Energy Scan (BES) programme at RHIC has shown that in AuAu collisions at $\sqrt{s_{NN}} = 62$ GeV the produced hadrons have a large elliptic flow and jet-quenching effects were observed [121, 122, 123, 124]. These results suggest that quarks and gluons are deconfined in this energy range and that the produced medium can be studied at the LHC in a fixed-target mode as well.

Model calculations indicate that μ_B and T of the produced medium depend on the charged-particle rapidity [125, 126, 127]. The right panel of Fig. 3.2(b) shows the rapidity dependence of μ_B as calculated by the viscous hydro+cascade model vHLLE+UrQMD [127]. According to this model, measurements performed in a broad rapidity coverage, such as the particle yield and their anisotropies, would allow one to scan various values of μ_B and T and thus the nuclear phase diagram from the deconfined regime to the phase transition to the hadronic gas. The left panel of Fig. 3.2(b) illustrates the possible coverage of the nuclear phase space diagram when using the LHC lead beam on a fixed target. It is compared to running and planned heavy-ion

experiments. A rapidity scan at the LHC in a fixed-target mode would be complementary to the beam energy scan performed at RHIC. Another possibility to scan the nuclear phase diagram would be to use various target and beam types. A fixed-target mode has the advantage of the versatility of the target. In addition, different beam types are possible at the LHC such as xenon beam that was used for a short run in Run 2. Oxygen beam is also envisioned in Run 3 or 4.

In the sector of quarkonium production, the excited states of Υ, as well as the charmonium states, are expected to melt into the QGP [128] at the medium temperature accessible at the LHC with a lead beam in a fixed-target mode. It would be very valuable to study the quarkonium production at this energy and to compare to the results obtained at nominal RHIC and LHC energies. In particular, the recombination process of $c\bar{c}$ pairs is not expected at $\sqrt{s_{NN}} = 72$ GeV. For the charmonium family, a direct measurement on χ_c production in heavy ion collisions still need to be measured at high energy. This would allow one to improve the understanding of charmonium production in proton-nucleus and nucleus-nucleus collisions since the χ_c contributes largely to the J/ψ production via feed-down. At RHIC energy, a first χ_c measurement was performed in dAu collisions at $\sqrt{s_{NN}} = 200$ GeV but with low precision [28].

(a)   (b)
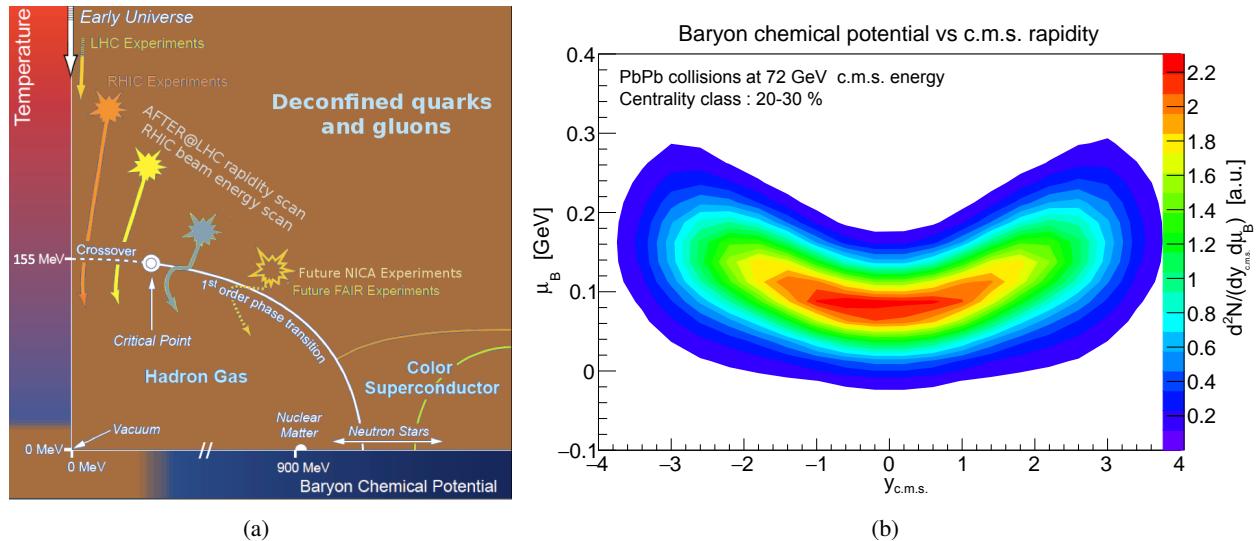
Figure 3.2: (a) Phase diagram of the strongly interacting matter and the reach of the heavy-ion program with a fixed-target experiment at the LHC (b) The baryonic chemical potential μ_B as a function of the rapidity y_{cms} in mid-central PbPb $\sqrt{s_{NN}} = 72$ GeV collisions predicted by the viscous hydro+cascade model vH-LLE+UrQMD [Adapted from [127]]. The colour represents the differential density of produced particles as a function of y_{cms} and μ_B.

3.2 Fixed-target implementations at the LHC

Several techniques are promising to obtain a fixed-target experiment at the LHC at high luminosity. LHCb has pioneered the use of gaseous fixed-target with the System for Measuring the Overlap with Gas (SMOG) [129, 130], originally designed for luminosity calibration. In that case, the gas density is low since the gas is not confined to a specific region and there is no dedicated pumping system. Also only noble gases have been used so far and for limited running time periods. Higher density gas targets are possible with the gas-jet system or by using a storage cell as illustrated in the bottom parts of Fig. 3.3. With those target setups, H, D and ^{3}He gases could be injected as well as polarised gases. Solid targets can also provide high luminosity

fixed-target experiment. The beam halo can directly interact with the target inserted inside the beam pipe as shown on the top right panel of Fig. 3.3. Another more promising solution, that has the advantage to be more parasitic to the main beams, is to deviate the beam halo on an internal solid target by using a bent crystal (see the top left panel of Fig. 3.3). With this technique, two solutions can be envisioned: either the beam is extracted and a new beam line is created, or the beam is used on a target located in an existing cavern (beam splitting). The first solution requires however civil engineering and could be achieved only over a longer timescale. The second solution is possible provided that the deflected beam halo is then absorbed upstream of the detector.
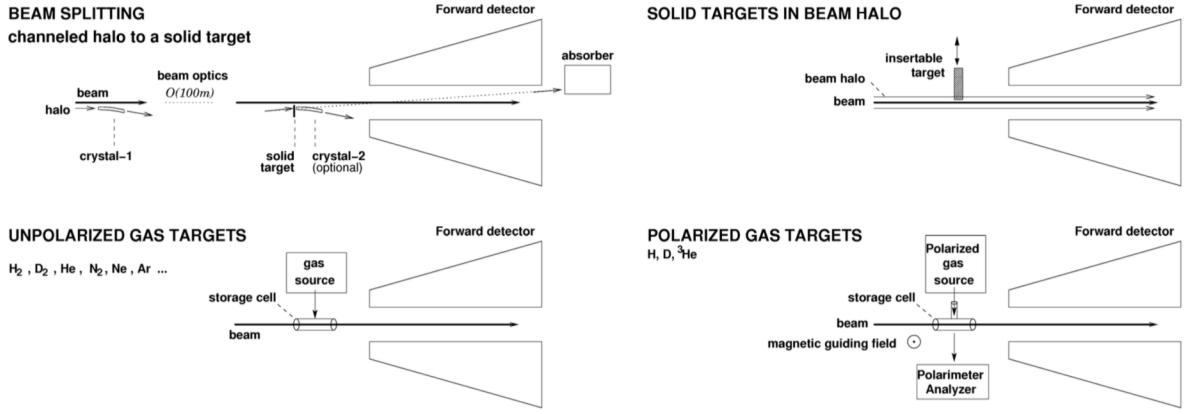

Figure 3.3: Various possible setups for fixed-target: crystal beam splitting for solid target with optionally a second crystal (top left), solid target in beam halo (top right), unpolarised gaseous target with optionally a storage cell (bottom left), polarised gas jet injected into the beam pipe with optionally a storage cell (bottom right). Figure from [131].

.

Several implementations of the gas and solid target solutions at the LHC were investigated in [117] and were discussed in the Physics Beyond Collider working groups at CERN, in particular with the aim at evaluating the effect on the LHC beams [131, 132]. Building a new dedicated experiment at the LHC would be the most suitable option, however one would need to have a large community working on and supporting the project, which is not the case now. It is also possible to use an existing detector at the LHC in order to cover a large part of the physics opportunities described earlier. There are different projects based on the internal gas target and the crystal/solid target solutions within the ALICE and LHCb collaborations. We will first discuss some general aspects regarding the acceptance and the multiplicities of possible fixed-target implementations at the LHC and we will then briefly describe the ongoing studies and projects.

3.2.1 General aspects: acceptance and multiplicity

One of the main motivation of the fixed-target programme at the LHC is to access the parton in the target at high x. Due to the large beam rapidity shift (4.8 units with the 7 TeV proton beam and 4.2 units with the 2.76 A TeV lead beam), the particle production is shifted towards larger angles. Figure 3.4 shows the rapidity coverage in the center of mass (y_{cms}) of the ALICE and LHCb detectors when used in collider and in fixed-target modes. In the latter case, various positions of the target are considered: either at the nominal interaction point corresponding to $z = 0$, or shifted on the opposite side of the ALICE muon spectrometer or the LHCb detectors. When the target is shifted from the nominal interaction point, the rapidity acceptance is estimated by considering the active area of the detectors and massless particles. These rapidity coverages

are also compared to those of the STAR and PHENIX detectors at RHIC. As illustrated in Fig. 3.4, the major advantage of a fixed-target experiment is that particle production can be easily measured at large negative y_{cms} with standard detector techniques and in particular with detectors with full particle identification capabilities. The full forward hemisphere is compressed into a very small solid angle area. Since the luminosities by using the LHC beams on a fixed target are expected to be high, as we will see later, it allows one to probe the full rapidity range with high statistics for many processes.
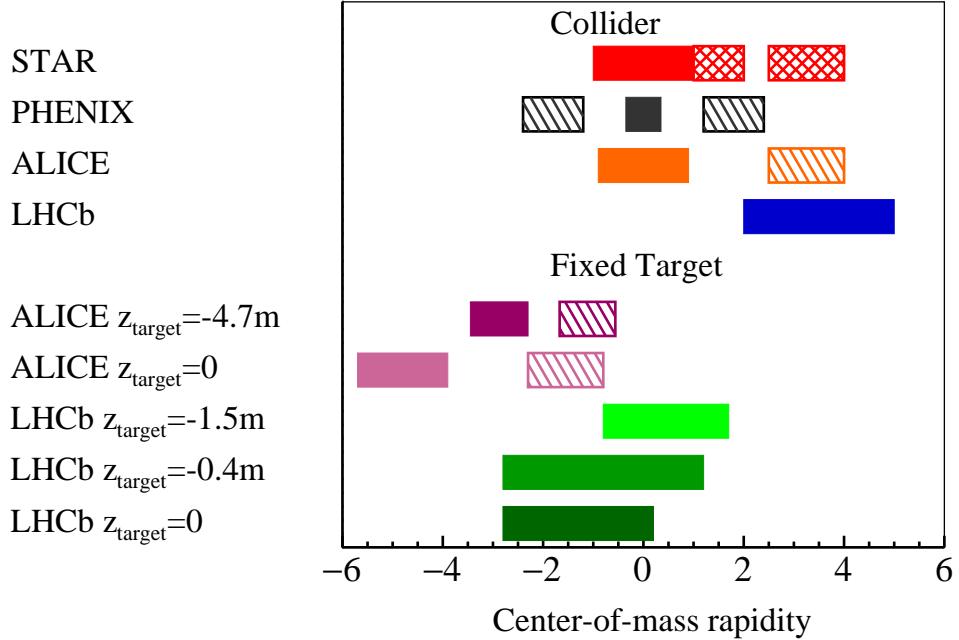

Figure 3.4: Comparison of the kinematical coverages of the ALICE and LHCb detectors at the LHC and the STAR and PHENIX detectors at RHIC. For ALICE and LHCb, the acceptance is shown in the collider and fixed-target modes for a 7 TeV proton beam and for various fixed-target positions. When the target position is at the nominal Interaction Point (IP), one has $z_{target} = 0$, otherwise the target is located on the opposite side of the muon spectrometer of ALICE or of the LHCb detectors. The fully filled rectangles refer to detectors with particle identification capabilities, the double-hatched rectangles to electromagnetic calorimeters and the hatched rectangles to muon detectors.

In the case of heavy nuclear targets, such as *Xe* or *W*, the detectors have to cope with the high multiplicities foreseen with the lead beam at $\sqrt{s_{NN}} = 72$ GeV. The average number of charged particles is maximal at $\eta_{lab} \sim 4.2$ and amount to $dN_{ch}/d\eta \sim 600 - 700$ for the most 10% central collisions according to EPOS [133, 134]. The charged-particles multiplicities are shown in Fig. 3.5 for various heavy-ion systems as a function of the pseudorapidity in the laboratory frame and is compared to the ones obtained at the LHC in a collider mode. In a fixed-target mode the multiplicities do not exceed the one obtained in the most central PbPb collisions at $\sqrt{s_{NN}} = 5.5$ TeV up to $\eta_{lab} \sim 7$.

3.2.2 Internal gas target

The LHCb collaboration has demonstrated that direct gas injection in the beam pipe is tolerable within a certain range. The SMOG system [129] has injected noble gases (He, Ne and Ar) into the VELO [135] chamber, *i.e.* inside the LHC beam pipe, for a limited time. The injected gas travels from the VELO chamber to the ion pump stations located about 20 m away on both sides. The current limitation to noble gases avoids altering the Non-Evaporable-Getter (NEG) coating properties of the beam pipe. The gas pressure is limited
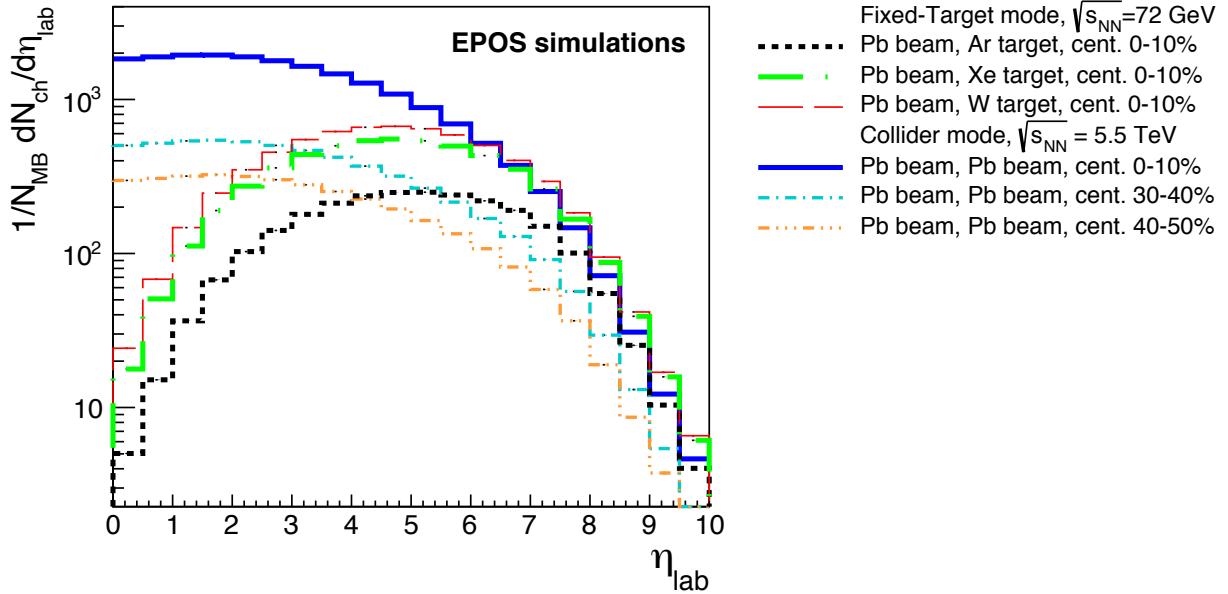
Figure 3.5: The averaged charged-particle multiplicity as a function of the pseudorapidity in the laboratory frame for the most central collisions in PbAr, PbXe and PbW collisions at $\sqrt{s_{NN}}$ = 72 GeV in a fixed-target mode and for various event centrality intervals in PbPb collisions at $\sqrt{s_{NN}}$ =5.5 TeV in a collider mode [117].

to about 1.5×10^{-7} mbar, *i.e.* two ordres of magnitude higher than the LHC vacuum pressure. First physics results obtained with the SMOG system were published in [136, 137]. Since the uncertainty on the gas pressure is large with the SMOG system, the luminosity was estimated from the yield of electrons scattering off gas atoms, a process that is theoretically well-known.

In order to increase the gas density, the SMOG2 project was proposed [138]. It consists of a storage cell (a long narrow tube of 20 cm with an inner diameter of 10 mm) placed inside the beam pipe on the axis of the LHC beam and in front of the VELO detector. The target is thus displaced from the nominal interaction point by around 40 cm. The gas is injected via capillary into the center of the target. The cell is openable in order to cope with the larger transverse beam size at beam injection or during beam adjustments. The two parts of the cell are connected to the VELO boxes and in order to move simultaneously to the VELO boxes. The project was accepted and is part of the LHCb upgrade for Run 3 [139]. It will allow an increase of the effective target areal density by up to 2 orders of magnitude with respect to SMOG for the most heavier gases. This system should in principle allow the use of gases such as H_2, D_2, O, Kr and Xe, in addition to the target species already used with SMOG. However vacuum studies are needed to define the gas density for those cases. As it can be seen on Fig. 3.4, the rapidity of the LHCb detectors is not expected to be modified by a shift of 40 cm of the target position. In terms of achievable luminosity, a first scenario was proposed for Run 3 [140] with the following luminosities: $\mathcal{L}_{pH}$ = 150 pb^{-1}, $\mathcal{L}_{pD}$ = 9 pb^{-1}, $\mathcal{L}_{pAr}$ = 45 pb^{-1}, $\mathcal{L}_{pKr}$ = 30 pb^{-1} and $\mathcal{L}_{pXe}$ = 22 pb^{-1} at $\sqrt{s_{NN}}$ = 115 GeV as well as $\mathcal{L}_{PbAr}$ = 50 nb^{-1}, $\mathcal{L}_{PbH}$ = 10 nb^{-1} and $\mathcal{L}_{pAr}$ = 5 pb^{-1} at $\sqrt{s_{NN}}$ = 72 GeV. SMOG2 will allow one to study many of the physics process described earlier at high luminosities over a broad rapidity range.

The storage cell can also be used in association with an Atomic Beam Source (ABS) that injects polarised gas (H, D or ^{3}He), such as the target that was used for the HERMES experiment [141] at DESY. The project LHCSpin [142] proposes to install this target around 1.5 m in front of the VELO of LHCb. The target system would be isolated by a valve from the VELO with a dedicated pumping system allowing to increase

the gas density in the target area *w.r.t.* SMOG2. An instantaneous luminosity of $\mathcal{L}_{pH} = 5 \times 10^{32}$cm^{-2}s^{-1} is achievable with this target system. In addition to the ABS, there is a magnet around the target to ensure a vertical holding field and a diagnostic system on the opposite side of the ABS. The diagnostic system consists of a Breit-Rabi polarimeter and a target gas analyzer to characterize the polarisation of the injected gas and the degree of recombination of the gas within the cell, respectively. A target polarisation of the order of 85 % is expected. Many studies are ongoing for that project. The main identified issue with respect to the original target from the HERMES experiment concerns the coating of the cell that does not comply with the LHC requirement and R&D studies are ongoing to find a proper coating. Since the target would be installed at 1.5 m from the VELO, it was proposed to install a vertex detector behind the target. The rapidity coverage of the LHCb detectors with a target positioned at 1.5 m from the nominal interaction point is shown in Fig. 3.4. The acceptance computed in the plot does not consider an additional vertex detector, neither geometrical constraints from the beam pipe. It is worth noting that displacing the target upstream of the nominal interaction point by few meters reduce the capability of the experiment to access the backward rapidity range in the center-of-mass frame, which is important to access the high-x partons in the target.

3.2.3 Crystal and internal solid target

When high-energy particles enter a crystal with small angles relative to the crystal planes, their transverse motion is governed by the crystal potential averaged over the planes. If the particle angles are smaller than the critical channeling angle, they can be captured into the channeling regime [143]. Channeled particles move through a crystal oscillating between two neighbouring planes. Channeling is also realised in a bent crystal if its bending radius is larger than the critical bending radius [144, 145] and high energy particles can be deviated by a bent crystal. The channeling process is used in particle accelerators for beam extraction and beam splitting. In particular, the UA9 collaboration has demonstrated the feasibility of crystal-assisted collimation in the SPS [146] and later in the LHC [147]. Crystal-assisted collimation relies on a well-oriented bent crystal located inside the beam pipe that deflects the channeled particles into an absorber. The halo particles that are intercepted by the crystal turn after turn are very well collimated and have a large probability of being channeled. The halo particles that are not captured at the first hit with the crystal, or that go through a nuclear reaction, continue circulating and have a high efficiency to be channeled by the crystal after one or more revolution. This is the so-called multi-pass channeling effect [148].

   A slight modification of the crystal collimation scheme allows one to deviate the beam halo particles into an internal target positioned in front of an existing experiment. The non-interacting deviated halo can be absorbed by a set of absorbers located behind the experiment. Figure 3.6 shows an example of a fixed-target scenario in ALICE [149]. A bent crystal of few mm and mounted on a goniometer could be located upstream of the interaction point by 70 m to channel and deflect the halo of the LHC beam horizontally by 250 μrad. This would allow one to place a target at 8 mm from the beam axis when located close to the interaction point (within few meters). A similar scheme has been proposed in LHCb to measure the electric and magnetic dipole moments of charmed charged baryons [150, 151, 152]. In the LHCb proposal, there is a second long bent crystal placed closely after the target that channels part of the baryons produced in the target and deflects them in the LHCb experiment by 7 mrad. Recent LHC collimation studies show that the layout proposed could deliver at least 10^6 protons per second in the case of the LHCb interaction point while being compatible with high intensity LHC physics operation (*i.e.* in parasitic operation) [131, 153]. It is worth noting that another interaction region, IR3, was also considered in these studies, that would require a new experimental setup but would give less constraints *w.r.t.* LHCb interaction region. Another scenario with controlled excitation of beam losses for selected proton bunches would provide higher flux but would need further studies. Such a scheme could be also used in the ALICE interaction region where dedicated collimation studies are needed. If a target of the order of 1 cm of W is used, the instantaneous luminosity expected in pW collisions with the deviated halo intensity quoted above is of the order of 6×10^{28} cm^{-2}s^{-1}.
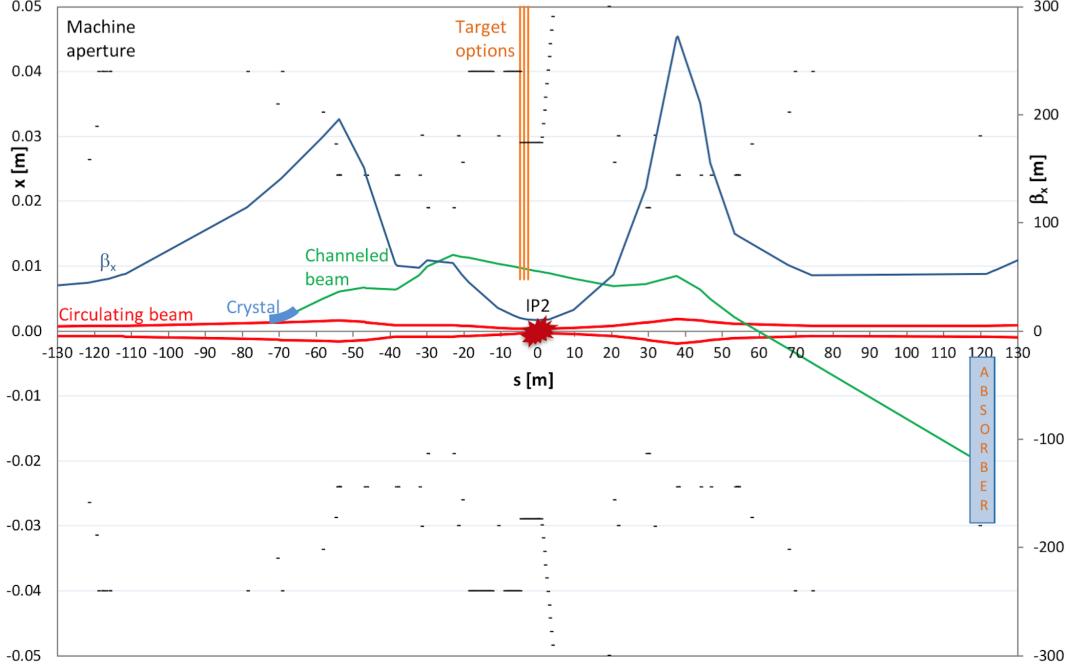
Figure 3.6: Particle trajectories for an internal fixed-target experiment: a bent crystal splits and deflects the halo (green) from the circulating beam (red), and sends it on an internal target (orange) placed in front of the ALICE detectors; the non-interacting channeled particles are caught by an absorber downstream; a safe distance is maintained between the channeled beam (green) and the machine aperture (black) [149].
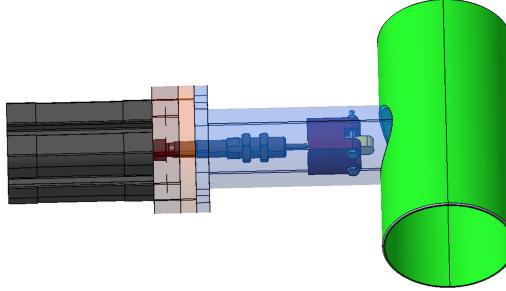

Figure 3.7: Setup for an internal solid target with one target system [149]. On the right side the pipe section is shown in green. Leftwards are visible the target (yellow), the target holder (brown), the actuator (black) and flanges (pink and orange) with a gasket inside. In translucent blue is the tapping of the pipe.

In ALICE, a solid target system has been designed in order to have a moveable target with a parking position outside of the beam pipe and small dimensions of the order of $170 \times 50 \times 50$ mm [149] for a better integration in the experiment. The target system is shown in Fig. 3.6 where the green part represents the beam pipe section and the translucent blue part the tapping of the pipe. The target, in yellow, with a radius of 2.5 mm, a total length of 17.5 mm and a width that can vary between 0.2 mm to few mm, is inserted into the beam pipe thanks to an actuator which is out of the vacuum. The actuator is a single-effect pneumatic actuator with a position of work inside the pipe when activated by pressurised air. An electro-valve distributor controls the position of the actuator through a plastic hose that can be away of the setup. It is possible to

51

design a setup with more than one target system allowing one to have several target types distributed along the beam pipe.

The integration of such system is constrained by the position and the integration of the existing detectors. A possible location would be at approximately 5 m from the interaction point in front of the existing valve. The target can outgas and the beam pipe section around the target system has to be isolated by adding a new valve behind the target, in order to maintain a high vacuum level in IP2. The rapidity coverage of the ALICE detectors with a target positioned at 4.7 m from the nominal interaction point is shown in Fig. 3.4. The acceptance computed in the plot does not consider possible geometrical constraints from the beam pipe. As previously mentioned, moving the target upstream of the nominal interaction point by few meters reduce the capability of the experiment to access the backward rapidity region in the center-of-mass frame.

3.3 Physics motivations for charmonium production in pA collisions at $\sqrt{s_{NN}} = 72$ and 115 GeV

The physics opportunities of running a fixed-target experiment at the LHC were evaluated and reviewed in [117]. In this Section, the interest of measuring charmonium production in pA collisions will be discussed.

In Section 1.4, it was discussed that various nuclear effects can affect the charmonium production in pA collisions and in Section 2, the results obtained at the LHC were presented and compared to those from RHIC as well as to theoretical calculations. The interpretation of the current RHIC and LHC data would benefit from additional measurements at lower energy and above the SPS and Fermilab energy.

At the LHC, two energies can be obtained in pA collisions with a nuclear target if one uses the 2.76 or the 7 TeV proton beam. The 2.76 TeV proton beams are usually required at LHC for a short running time of the order of the week as it serves as a reference for the heavy-ion collisions. High precision data over a broad rapidity and p_T range in pA collisions at $\sqrt{s_{NN}} = 72$ and 115 GeV would help to disentangle the various cold nuclear matter effects and to constrain theoretical models. We have also discussed earlier that it would be very valuable to measure precisely the χ_c production since it is expected to contribute to the prompt J/ψ production through feed-down in pA collisions.

Assuming only the modification of the PDFs in the nucleus on the $c\bar{c}$ and $b\bar{b}$ pair production, a study has been carried out in [117] to estimate the impact of open and hidden heavy flavour production (D^0, J/ψ, B^+ and Υ(1S)) in a fixed target mode at the LHC on the nPDFs. In this study a data-driven approach [82] is used to fit the matrix elements of heavy flavour production in pp collisions. In order to compute the heavy flavour production in pA collisions, the matrix elements are then folded with proton CT14 PDFs and nucleus nCTEQ15 nPDFs. The nuclear modification factor is then extracted from these computations by considering pp and pXe collisions at $\sqrt{s_{NN}} = 115$ GeV with an integrated luminosity of 10 fb^{-1} and 100 pb^{-1}, respectively. Typical values of efficiency of 10% and systematic uncertainties of 2% (uncorrelated) and 5% (correlated over rapidity) are considered. The branching ratios of $D^0 \rightarrow K\pi$, $B^+ \rightarrow KJ/\psi \rightarrow K\mu^+\mu^-$, J/$\psi \rightarrow \mu^+\mu^-$ and Υ(1S) $\rightarrow \mu^+\mu^-$ are also included for the yield and statistical uncertainty estimation. For D^0 and B^+, their charge conjugate particles are summed up.

The nuclear modification factors R_{pXe} are shown in Fig. 3.8 for the four particles. The interval of rapidity in the center-of-mass frame corresponds to a rapidity in the laboratory frame of $2 < y_{lab} < 5$, such as the one of LHCb. The red enveloppe corresponds to the uncertainties of the nCTEQ15 nPDFs. The R_{pXe} were evaluated at three different choices of the factorisation scale μ_F. A Bayesian-reweighting analysis was performed as in [32] for each particle separately by considering the pseudo-data with their total uncertainties. The blue enveloppe corresponds to the reweighted nCTEQ15 nPDFs uncertainties. A large reduction of the nPDFs uncertainties is obtained in particular in the backward rapidity range. As it can be seen from the projected uncertainties, a high statistical data sample is motivated to access a broad rapidity range, in particular the interval of the far backward rapidity in the center of mass with the open and hidden beauty

probes.
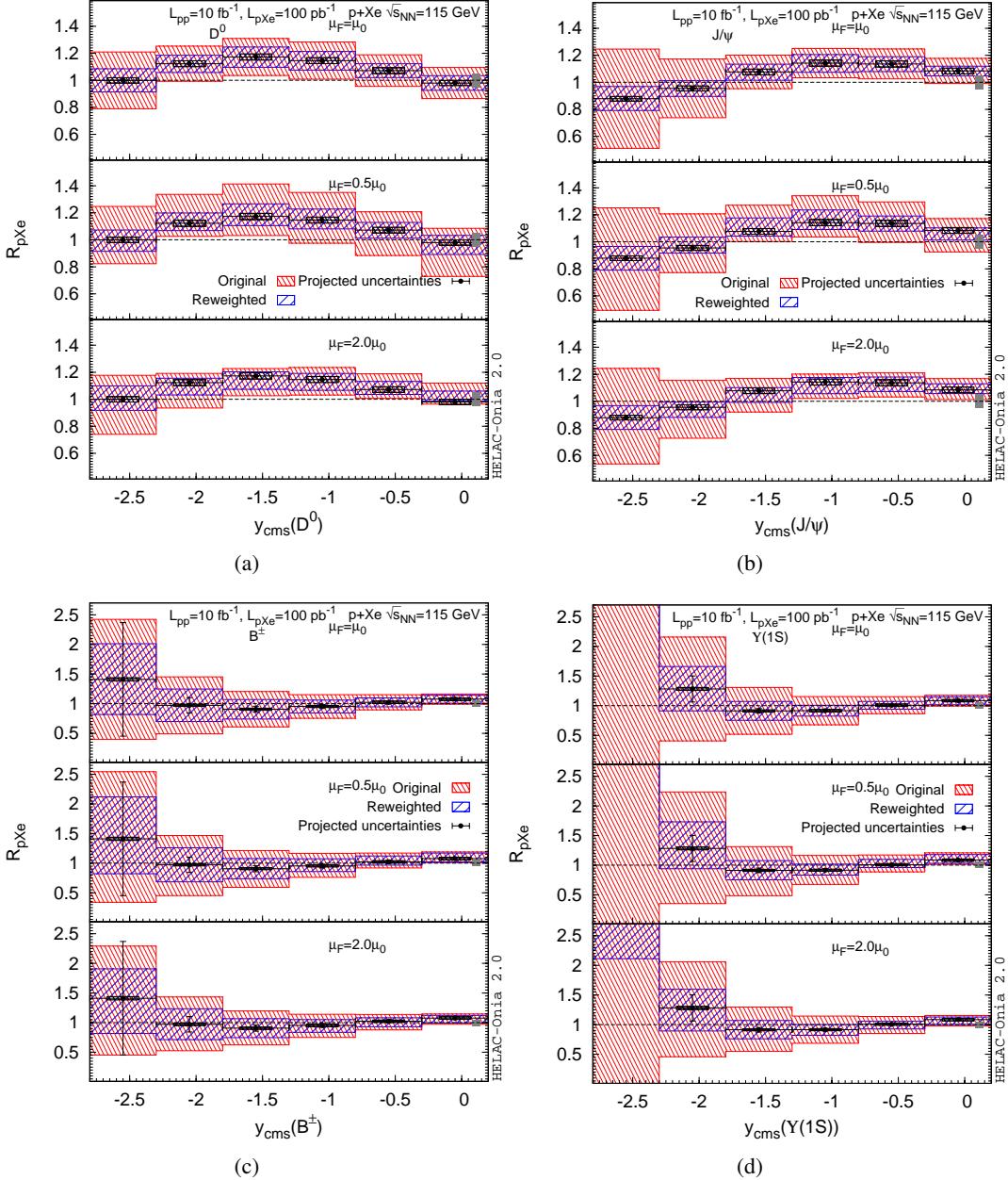
Figure 3.8: Projection of the statistical uncertainties on the R_{pA} using the LHCb detectors in a fixed-target mode for (a) D^0, (b) J/ψ, (c) B^+, and (d) $\Upsilon(1S)$ production in pXe collisions compared to the uncertainties encoded in nCTEQ15 nPDFs, which are representative of typical nPDF uncertainties, evaluated at different typical choices of the factorisation scale, μ_F, like in [32]. The default normalisation scale, μ_0, is taken to be $M^2 + p_T^2$ for J/ψ and $\Upsilon(1S)$, $4M^2 + p_T^2$ for D^0 and B^+. A 2% uncorrelated systematic uncertainty and a 5% global uncertainty are also shown. Figures from [117].

The impact of the pseudo-data is visible in Fig. 3.9. The four panels show the ratio of nCTEQ15 gluon nPDFs over the CT14 gluon PDFs at a scale $Q = 2$ GeV before and after the reweighting for the three factorisation scales and for each particle. A combined analysis would reduce further the nPDFs uncertainty.

In particular the high-*x* region is largely constrained by the pseudo-data as expected and discussed in Section 3.1.1 with the left panel of Fig. 3.1 in the case of the LHCb rapidity acceptance. This study illustrates that measurements on open and hidden heavy flavour production at backward rapidity with a high luminosity would allow one to improve our knowledge on nPDFs, in particular at high-*x*.
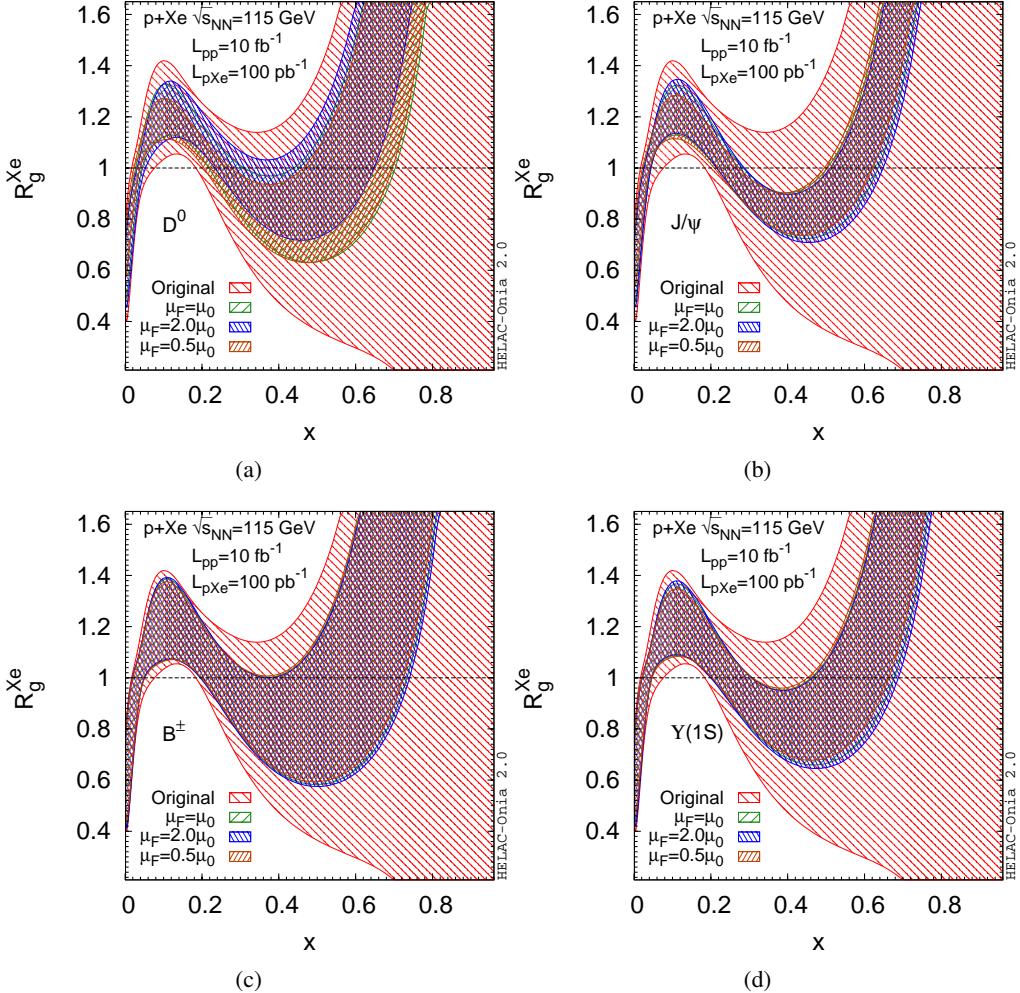

Figure 3.9: nCTEQ15 nPDFs before and after the reweighting using R_{pXe} pseudo-data shown in Fig. 3.8 for (a) D^0, (b) J/ψ, (c) B^+, (d) $\Upsilon(1S)$ production. The plots show ratios R_g^{Xe} of gluon densities encoded in nCTEQ15 over that in CT14 PDFs at a scale $Q = 2$ GeV. Figures from [117].

As specified above, this study assumes the absence of other cold nuclear matter effects or that those other effects can be subtracted. At LHC collider energies this approach was applied to existing data [32]. At lower energies, and particularly in the backward rapidity region and at low p_T, quarkonium breakup by nuclear absorption will likely happen and should be disentangle from other effects. The excited states of charmonium (and bottomonium) can help to disentangle the nuclear absorption effect since it depends on the binding energy of the bounding state.

In [154], the effect from energy loss has been estimated for J/ψ and Υ production in pCa, pCu and pPb collisions at $\sqrt{s_{NN}} = 115$ GeV. The nuclear modification factor are shown in the left (J/ψ) and right (Υ) panels of Fig. 3.10 as a function of y_{cms}. The expected modification in those systems *w.r.t.* pp collisions is of the order of 10-20% for $y_{cms} > -2.5$ for the J/ψ and $y_{cms} > -2$ for the Υ. The vertical arrows indicate the criti-

cal rapidity, y_c, below which the J/ψ and Υ may suffer inelastic interactions from the surrounding nucleons while escaping the nucleus. y_c is calculated from the nucleus radius, the quarkonium formation time and the collision energy. At $y_{\mathrm{cms}} < y_c$, an additional suppression from nuclear absorption is expected. For the J/ψ, the amplitude of the modification is similar to nCTEQ15 nPDFs but while the central values of nCTEQ15 nPDFs indicate an enhancement of the J/ψ production, the energy loss model predicts a suppression for $y_{\mathrm{cms}} > -1.8$.
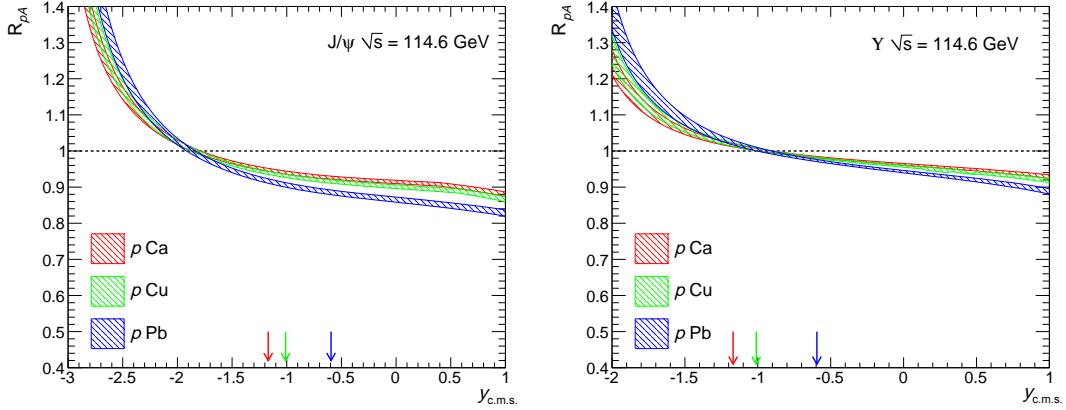

Figure 3.10: J/ψ (left) and Υ (right) nuclear modification factor in pCa, pCu and pPb collisions at $\sqrt{s} = 114.6$ GeV resulting from the coherent energy loss model [154].

In addition to charmonium studies, it will be very interesting to study the Drell-Yan process, a more cleaner process than charmonium production since its production mechanism is well known in pp collisions and the invariant mass of the dilepton gives the scale Q of the process. Also only initial state effects are expected to modify its production in pA collisions *w.r.t.* pp collisions. Drell-Yan data are used in global (n)PDF analyses to extract the light quark and anti-quark distributions and will be complementary to charmonium measurements.

Finally, it would be valuable to search for collective dynamics of partons in pA collisions in a fixed-target mode at the LHC. As shown in Section 2.3.1 a positive v_2 has been measured in pPb collisions for inclusive J/ψ at $\sqrt{s_{NN}} = 5.02$ TeV with a magnitude similar to the elliptic flow measured in PbPb collisions for $3 < p_{\mathrm{T}} < 6$ GeV/c. In heavy-ion collisions, a positive v_2 is usually interpreted as an indication of collective interactions at the partonic level and of a possible QGP formation. Also at lower energy in the RHIC beam energy scan, positive flow parameters were measured for charged particles down to $\sqrt{s_{NN}} = 19.6$ GeV [155]. Studying heavy flavour and more specifically charmonium production at $\sqrt{s_{NN}} = 72$ and 115 GeV with various types of targets from low to high atomic mass would contribute to the understanding of the collective behaviour in small systems.

By using a deuterium target transversally polarised with a lead beam, one could measure the elliptic flow of charged particles with respect to the target polarisation axis [156]. This is equivalent of measuring the azimuthal asymmetry of the final hadrons from the one-particle distribution. This would allow one to disentangle different models that reproduce well the elliptic flow measured in pA collisions at RHIC and the LHC. In the case of correlations from gluon dynamics (Color Glass Condensate model), no azimuthal asymmetries are expected while hydrodynamic and transport models that describe collective dynamics of partons in pA collisions predict a non zero elliptic flow with respect to the target polarisation axis. These measurements could be done for heavy-flavour production as well.

55

Conclusion

Charmonium production is extensively studied experimentally and theoretically since its discovery in 1974. It provides a testing ground for perturbative and non-perturbative aspects of QCD calculations in high-energy hadronic collisions. In heavy-ion collisions, it is used as a probe of the quark gluon plasma and in proton-nucleus collisions, it gives insight on the cold nuclear medium effects that modify its production *w.r.t.* proton-proton collisions.

The LHC has delivered a large integrated luminosity of pPb collisions at two different energies, $\sqrt{s_{NN}} =$ 5.02 and 8.16 TeV. These collisions have allowed precise measurements and have given precious informations on charmonium production, in particular thanks to the muon spectrometer of the ALICE experiment.

The nuclear effects are estimated with the nuclear modification factor, R_{pPb}, that compares the production of charmonia in pPb collisions with their production in pp collisions normalised by the number of binary nucleon collisions. A suppression of the J/ψ production is observed at mid- and forward rapidity in pPb collisions, concentrated in the low p_T region ($p_T < 5$ GeV/c) and in the most central collisions. At larger p_T, the J/ψ production in pPb collisions is compatible with the binary scaling of its production in pp collisions and this supports the absence of nuclear effects. At backward rapidity, the J/ψ production is compatible with no suppression, however the R_{pPb} increases from low p_T to higher p_T, suggesting small but p_T dependent nuclear effect. Similar results are found at $\sqrt{s_{NN}} = 5.02$ and 8.16 TeV. The p_T broadening increases at backward and forward rapidity with increasing centrality with a steeper increase at forward rapidity. Models based on pure initial state effects (shadowing and gluon saturation) or that include effect from the final state (coherent energy loss, comovers and transport models) gives a rather good description of the suppression observed. Other observables such as the self-normalised yield as a function of charged particles or the elliptic flow have been measured. In particular, the J/ψ elliptic flow is found to be positive for $3 < p_T < 6$ GeV/c. Since the obtained values are similar than those measured in PbPb collisions for the same p_T interval, these results suggest that similar mechanism is at play in both collision systems, such as collective-like effects.

The $\psi(2S)$ excited charmonium state is suppressed at backward and forward rapidity and is relatively suppressed *w.r.t.* to the production of J/ψ. This suggests that final-state effects such as those from comoving particles that are produced along the charmonia (comover model) or from hot nuclear matter (transport model) need to be considered to describe the production of this weakly bound charmonium state.

A comparison of the results obtained at LHC with those of RHIC at $\sqrt{s_{NN}} = 200$ GeV is very valuable since it allows to constrain the models at different energies. Finally, results obtained at the LHC on open charm and open and hidden beauty production are essential to understand better the CNM effects. In particular, the similarity of suppression of the D meson with the J/ψ suggests that initial state effects are the dominant ones for J/ψ production. The measurements from bottomonium were not predicted by most of the models in particular the suppression measured at low p_T and backward rapidity at the LHC. In the beauty sector, more statistics will improve the current understanding of CNM effects.

The LHC can also run in a fixed-target mode with one beam scattering on a target placed inside the beam line, allowing one to reach center of mass energy per nucleon pair of $\sqrt{s_{NN}} = 115$ GeV with the 7 TeV proton beam and $\sqrt{s_{NN}} = 72$ GeV with the 2.76 A TeV lead beam. The achievable luminosities are expected to be high when considering the fixed-target implementations based on internal gas target and on

solid target coupled to a bent crystal that deviates the beam halo. Both implementations could allow the fixed-target setup to run parasitically to the LHC nominal operation. The target versatility, as well as a broad rapidity range that could be probed by the ALICE and LHCb detectors if used in a fixed-target mode, are nice features that give access in proton-nucleus collisions to the high-x content of the nuclear structure and to the study of CNM effects over a broad rapidity range with charmonium production.

Open and hidden heavy-flavour production will be further studied in the future at RHIC and LHC. In particular, the upgrades of the ALICE detectors [157] are currently ongoing during the long shutdown 2 (2019-2020). The upgrades are planned for Run 3 and 4 (2021-2030). They will allow for a continuous readout and better studies of correlations between the muon spectrometer and the central barrel by using identified particles. A Muon Forward Tracker [158] will be placed in front of the absorber of the muon spectrometer in order to separate the prompt J/ψ production from the non-prompt one. The MFT will also reduce the background for the $\psi(2S)$ leading to measurements with better precision. The luminosity in proton-lead collisions is expected to be 300 nb^{-1} [159], *i.e.* about a factor 10 higher than the luminosity collected with the muon spectrometer in ALICE in Run 2. The MFT will allow one to measure the hadronic environment around the measured particles in all systems by using isolation criteria. The other LHC experiments (AT-LAS, CMS and LHCb) will also collect a high luminosity data sample in proton-nucleus collisions during Run 3 and 4. In the LHC fixed-target mode, we are studying in ALICE the possibility offered by an internal solid target associated to bent crystal that deviates the halo of the LHC beams, with the aim of installing the target and crystal systems in 2027 for Run 4. LHCb will collect data in Run 3 with the SMOG2 system that will provide up to 100 times higher gas density than the SMOG system used in Run 2. LHCb is also studying a polarised gas target system that aims at running in Run 4. Finally, at RHIC, the sPHENIX experiment [160] is aiming at precision measurements of the Υ family at midrapidity at $\sqrt{s_{NN}}$ = 200 GeV. It will collect proton-gold collisions at $\sqrt{s_{NN}}$ = 200 GeV with an integrated luminosity of 3.2 pb^{-1} and it is expected to take place in 2023.

Bibliography

[1] **Particle Data Group** Collaboration, M. Tanabashi *et al.*, "Review of Particle Physics," *Phys. Rev.* **D98** no. 3, (2018) 030001.

[2] J.-P. Lansberg, "New Observables in Inclusive Production of Quarkonia," `arXiv:1903.09185 [hep-ph]`.

[3] M. L. Mangano, "Two lectures on heavy quark production in hadronic collisions," *Proc. Int. Sch. Phys. Fermi* **137** (1998) 95–137, `arXiv:hep-ph/9711337 [hep-ph]`.

[4] S. Forte and G. Watt, "Progress in the Determination of the Partonic Structure of the Proton," *Ann. Rev. Nucl. Part. Sci.* **63** (2013) 291–328, `arXiv:1301.6754 [hep-ph]`.

[5] **ALICE** Collaboration, S. Acharya *et al.*, "Energy dependence of forward-rapidity J/ψ and ψ(2S) production in pp collisions at the LHC," *Eur. Phys. J.* **C77** no. 6, (2017) 392, `arXiv:1702.00557 [hep-ex]`.

[6] **CMS** Collaboration, A. M. Sirunyan *et al.*, "Measurement of quarkonium production cross sections in pp collisions at $\sqrt{s}$ = 13 TeV," *Phys. Lett.* **B780** (2018) 251–272, `arXiv:1710.11002 [hep-ex]`.

[7] Y.-Q. Ma, K. Wang, and K.-T. Chao, "J/ψ(ψ') production at the Tevatron and LHC at $O(\alpha_s^4 v^4)$ in nonrelativistic QCD," *Phys. Rev. Lett.* **106** (2011) 042002, `arXiv:1009.3655 [hep-ph]`.

[8] Y.-Q. Ma and R. Venugopalan, "Comprehensive Description of J/ψ Production in Proton-Proton Collisions at Collider Energies," *Phys. Rev. Lett.* **113** no. 19, (2014) 192301, `arXiv:1408.4075 [hep-ph]`.

[9] M. Cacciari, S. Frixione, N. Houdeau, M. L. Mangano, P. Nason, and G. Ridolfi, "Theoretical predictions for charm and bottom production at the LHC," *JHEP* **10** (2012) 137, `arXiv:1205.6344 [hep-ph]`.

[10] **HotQCD** Collaboration, A. Bazavov *et al.*, "Chiral crossover in QCD at zero and non-zero chemical potentials," *Phys. Lett. B* **795** (2019) 15–21, `arXiv:1812.08235 [hep-lat]`.

[11] M. Strickland, "Anisotropic Hydrodynamics: Three lectures," *Acta Phys. Polon.* **B45** no. 12, (2014) 2355–2394, `arXiv:1410.5786 [nucl-th]`.

[12] **ALICE** Collaboration, J. Adam *et al.*, "Centrality dependence of the pseudorapidity density distribution for charged particles in Pb-Pb collisions at $\sqrt{s_{NN}}$ = 5.02 TeV," *Phys. Lett.* **B772** (2017) 567–577, `arXiv:1612.08966 [nucl-ex]`.

[13] T. Matsui and H. Satz, "J/ψ Suppression by Quark-Gluon Plasma Formation," *Phys. Lett.* **B178** (1986) 416–422.

[14] S. Digal, P. Petreczky, and H. Satz, "Quarkonium feed down and sequential suppression," *Phys. Rev.* **D64** (2001) 094015, `arXiv:hep-ph/0106017 [hep-ph]`.

[15] H. Satz, "Colour deconfinement and quarkonium binding," *J. Phys.* **G32** (2006) R25, `arXiv:hep-ph/0512217 [hep-ph]`.

[16] P. Braun-Munzinger and J. Stachel, "(Non)thermal aspects of charmonium production and a new look at J / psi suppression," *Phys.Lett.* **B490** (2000) 196–202, `arXiv:nucl-th/0007059 [nucl-th]`.

[17] R. L. Thews, M. Schroedter, and J. Rafelski, "Enhanced J/ψ production in deconfined quark matter," *Phys.Rev.* **C63** (2001) 054905, `arXiv:hep-ph/0007323 [hep-ph]`.

[18] **NA50** Collaboration, B. Alessandro *et al.*, "A New measurement of J/psi suppression in Pb-Pb collisions at 158-GeV per nucleon," *Eur. Phys. J.* **C39** (2005) 335–345, `arXiv:hep-ex/0412036 [hep-ex]`.

[19] **PHENIX** Collaboration, A. Adare *et al.*, "J/ψ Production vs Centrality, Transverse Momentum, and Rapidity in Au+Au Collisions at $\sqrt{s_{NN}}$ = 200 GeV," *Phys. Rev. Lett.* **98** (2007) 232301, `arXiv:nucl-ex/0611020 [nucl-ex]`.

[20] **PHENIX** Collaboration, A. Adare *et al.*, "J/ψ suppression at forward rapidity in Au+Au collisions at $\sqrt{s_{NN}}$ = 200 GeV," *Phys. Rev.* **C84** (2011) 054912, `arXiv:1103.6269 [nucl-ex]`.

[21] **STAR** Collaboration, L. Adamczyk *et al.*, "J/ψ production at low p_T in Au + Au and Cu + Cu collisions at $\sqrt{s_{NN}}$ = 200 GeV with the STAR detector," *Phys. Rev.* **C90** no. 2, (2014) 024906, `arXiv:1310.3563 [nucl-ex]`.

[22] **ALICE** Collaboration, B. B. Abelev *et al.*, "Centrality, rapidity and transverse momentum dependence of J/ψ suppression in Pb-Pb collisions at $\sqrt{s_{NN}}$=2.76 TeV," *Phys. Lett.* **B734** (2014) 314–327, `arXiv:1311.0214 [nucl-ex]`.

[23] **ALICE** Collaboration, J. Adam *et al.*, "J/ψ suppression at forward rapidity in Pb-Pb collisions at $\sqrt{s_{NN}}$ = **5.02** TeV," *Phys. Lett.* **B766** (2017) 212–224, `arXiv:1606.08197 [nucl-ex]`.

[24] **CMS** Collaboration, A. M. Sirunyan *et al.*, "Measurement of prompt D^0 meson azimuthal anisotropy in Pb-Pb collisions at $\sqrt{s_{NN}}$ = 5.02 TeV," *Phys. Rev. Lett.* **120** no. 20, (2018) 202301, `arXiv:1708.03497 [nucl-ex]`.

[25] **ALICE** Collaboration, S. Acharya *et al.*, "D-meson azimuthal anisotropy in midcentral Pb-Pb collisions at $\sqrt{s_{NN}}$ = **5.02** TeV," *Phys. Rev. Lett.* **120** no. 10, (2018) 102301, `arXiv:1707.01005 [nucl-ex]`.

[26] **ALICE** Collaboration, S. Acharya *et al.*, "J/ψ elliptic flow in Pb-Pb collisions at $\sqrt{s_{NN}}$ = 5.02 TeV," *Phys. Rev. Lett.* **119** no. 24, (2017) 242301, `arXiv:1709.05260 [nucl-ex]`.

[27] B. Z. Kopeliovich and B. G. Zakharov, "Quantum effects and color transparency in charmonium photoproduction on nuclei," *Phys. Rev.* **D44** (1991) 3466–3472.

[28] **PHENIX** Collaboration, A. Adare *et al.*, "Nuclear Modification of $\psi(2S), \chi_c$, and J/ψ Production in d+Au Collisions at $\sqrt{s_{NN}}$=200 GeV," *Phys. Rev. Lett.* **111** no. 20, (2013) 202301, `arXiv:1305.5516 [nucl-ex]`.

[29] **European Muon** Collaboration, J. J. Aubert *et al.*, "The ratio of the nucleon structure functions F_2^N for iron and deuterium," *Phys. Lett.* **B123** (1983) 275–278.

[30] K. J. Eskola, P. Paakkinen, H. Paukkunen, and C. A. Salgado, "EPPS16: Nuclear parton distributions with LHC data," *Eur. Phys. J.* **C77** no. 3, (2017) 163, arXiv:1612.05741 [hep-ph].

[31] K. Kovarik *et al.*, "nCTEQ15 - Global analysis of nuclear parton distributions with uncertainties in the CTEQ framework," *Phys. Rev.* **D93** no. 8, (2016) 085037, arXiv:1509.00792 [hep-ph].

[32] A. Kusina, J.-P. Lansberg, I. Schienbein, and H.-S. Shao, "Gluon Shadowing in Heavy-Flavor Production at the LHC," *Phys. Rev. Lett.* **121** no. 5, (2018) 052004, arXiv:1712.07024 [hep-ph].

[33] K. J. Eskola, I. Helenius, P. Paakkinen, and H. Paukkunen, "A QCD analysis of LHCb D-meson data in p+Pb collisions," arXiv:1906.02512 [hep-ph].

[34] K. J. Eskola, H. Paukkunen, and C. A. Salgado, "EPS09: A New Generation of NLO and LO Nuclear Parton Distribution Functions," *JHEP* **04** (2009) 065, arXiv:0902.4154 [hep-ph].

[35] **PHENIX** Collaboration, S. S. Adler *et al.*, "J/psi production and nuclear effects for d+Au and p+p collisions at s(NN)**(1/2) = 200-GeV," *Phys. Rev. Lett.* **96** (2006) 012304, arXiv:nucl-ex/0507032 [nucl-ex].

[36] E. Iancu and R. Venugopalan, "The Color glass condensate and high-energy scattering in QCD," in *Quark-gluon plasma 4*, R. C. Hwa and X.-N. Wang, eds., pp. 249–3363. 2003. arXiv:hep-ph/0303204 [hep-ph].

[37] H. Fujii and K. Watanabe, "Heavy quark pair production in high energy pA collisions: Quarkonium," *Nucl. Phys.* **A915** (2013) 1–23, arXiv:1304.2221 [hep-ph].

[38] B. Ducloué, T. Lappi, and H. Mäntysaari, "Forward J/ψ production in proton-nucleus collisions at high energy," *Phys. Rev.* **D91** no. 11, (2015) 114005, arXiv:1503.02789 [hep-ph].

[39] B. Ducloué, T. Lappi, and H. Mäntysaari, "Forward J/ψ production at high energy: centrality dependence and mean transverse momentum," *Phys. Rev.* **D94** no. 7, (2016) 074031, arXiv:1605.05680 [hep-ph].

[40] Y.-Q. Ma, R. Venugopalan, and H.-F. Zhang, "J/ψ production and suppression in high energy proton-nucleus collisions," *Phys. Rev.* **D92** (2015) 071901, arXiv:1503.07772 [hep-ph].

[41] Y.-Q. Ma, R. Venugopalan, K. Watanabe, and H.-F. Zhang, "$\psi(2S)$ versus J/ψ suppression in proton-nucleus collisions from factorization violating soft color exchanges," *Phys. Rev.* **C97** no. 1, (2018) 014909, arXiv:1707.07266 [hep-ph].

[42] R. Sharma and I. Vitev, "High transverse momentum quarkonium production and dissociation in heavy ion collisions," *Phys. Rev.* **C87** no. 4, (2013) 044905, arXiv:1203.0329 [hep-ph].

[43] B. Z. Kopeliovich, I. Schmidt, and M. Siddikov, "Suppression versus enhancement of heavy quarkonia in pA collisions," *Phys. Rev.* **C95** no. 6, (2017) 065203, arXiv:1701.07134 [hep-ph].

[44] F. Arleo and S. Peigne, "Heavy-quarkonium suppression in p-A collisions from parton energy loss in cold QCD matter," *JHEP* **03** (2013) 122, arXiv:1212.0434 [hep-ph].

[45] **NuSea** Collaboration, M. J. Leitch *et al.*, "Measurement of J / psi and psi-prime suppression in p-A collisions at 800-GeV/c," *Phys. Rev. Lett.* **84** (2000) 3256–3260, arXiv:nucl-ex/9909007 [nucl-ex].

[46] C. Lourenco, R. Vogt, and H. K. Woehri, "Energy dependence of J/psi absorption in proton-nucleus collisions," *JHEP* **02** (2009) 014, arXiv:0901.3054 [hep-ph].

[47] D. C. McGlinchey, A. D. Frawley, and R. Vogt, "Impact parameter dependence of the nuclear modification of J/ψ production in d+Au collisions at $\sqrt{S_{NN}}$ = 200 GeV," *Phys. Rev.* **C87** no. 5, (2013) 054910, arXiv:1208.2667 [nucl-th].

[48] A. Andronic *et al.*, "Heavy-flavour and quarkonium production in the LHC era: from proton-proton to heavy-ion collisions," *Eur. Phys. J.* **C76** no. 3, (2016) 107, arXiv:1506.03981 [nucl-ex].

[49] A. Capella, A. Kaidalov, A. Kouider Akil, and C. Gerschel, "J / psi and psi-prime suppression in heavy ion collisions," *Phys. Lett.* **B393** (1997) 431–436, arXiv:hep-ph/9607265 [hep-ph].

[50] E. G. Ferreiro, "Charmonium dissociation and recombination at LHC: Revisiting comovers," *Phys. Lett.* **B731** (2014) 57–63, arXiv:1210.3209 [hep-ph].

[51] E. G. Ferreiro, "Excited charmonium suppression in proton-nucleus collisions as a consequence of comovers," *Phys. Lett.* **B749** (2015) 98–103, arXiv:1411.0549 [hep-ph].

[52] A. Adare *et al.*, "Measurement of J/ψ at forward and backward rapidity in p+p, p+Al, p+Au, and ^{3}He+Au collisions at $\sqrt{s_{NN}}$ = 200 GeV," arXiv:1910.14487 [hep-ex].

[53] X. Du and R. Rapp, "In-Medium Charmonium Production in Proton-Nucleus Collisions," *JHEP* **03** (2019) 015, arXiv:1808.10014 [nucl-th].

[54] **CMS** Collaboration, V. Khachatryan *et al.*, "Evidence for Collective Multiparticle Correlations in p-Pb Collisions," *Phys. Rev. Lett.* **115** no. 1, (2015) 012301, arXiv:1502.05382 [nucl-ex].

[55] **ALICE** Collaboration, B. B. Abelev *et al.*, "Multiparticle azimuthal correlations in p -Pb and Pb-Pb collisions at the CERN Large Hadron Collider," *Phys. Rev.* **C90** no. 5, (2014) 054901, arXiv:1406.2474 [nucl-ex].

[56] **ATLAS** Collaboration, M. Aaboud *et al.*, "Measurement of multi-particle azimuthal correlations in pp, p+Pb and low-multiplicity Pb+Pb collisions with the ATLAS detector," *Eur. Phys. J.* **C77** no. 6, (2017) 428, arXiv:1705.04176 [hep-ex].

[57] Y. Liu, C. M. Ko, and T. Song, "Hot medium effects on J/ψ production in p + Pb collisions at $\sqrt{s_{NN}}$ = 5.02 TeV," *Phys. Lett.* **B728** (2014) 437–442, arXiv:1309.5113 [nucl-th].

[58] B. Chen, T. Guo, Y. Liu, and P. Zhuang, "Cold and Hot Nuclear Matter Effects on Charmonium Production in p+Pb Collisions at LHC Energy," *Phys. Lett.* **B765** (2017) 323–327, arXiv:1607.07927 [nucl-th].

[59] X. Du and R. Rapp, "Sequential Regeneration of Charmonia in Heavy-Ion Collisions," *Nucl. Phys.* **A943** (2015) 147–158, arXiv:1504.00670 [hep-ph].

[60] R. Vogt, "Shadowing effects on J/ψ and Υ production at energies available at the CERN Large Hadron Collider," *Phys. Rev.* **C92** no. 3, (2015) 034909, arXiv:1507.04418 [hep-ph].

[61] F. Arleo and S. Peigné, "Quarkonium suppression in heavy-ion collisions from coherent energy loss in cold nuclear matter," *JHEP* **10** (2014) 073, arXiv:1407.5054 [hep-ph].

[62] B. Z. Kopeliovich, I. K. Potashnikova, H. J. Pirner, and I. Schmidt, "Heavy quarkonium production: Nontrivial transition from pA to AA collisions," *Phys. Rev.* **C83** (2011) 014912, `arXiv:1008.4272 [hep-ph]`.

[63] **ALICE** Collaboration, K. Aamodt *et al.*, "The ALICE experiment at the CERN LHC," *JINST* **3** (2008) S08002.

[64] **ALICE** Collaboration, B. B. Abelev *et al.*, "Performance of the ALICE Experiment at the CERN LHC," *Int. J. Mod. Phys.* **A29** (2014) 1430044, `arXiv:1402.4476 [nucl-ex]`.

[65] **ALICE** Collaboration, J. Adam *et al.*, "Centrality dependence of particle production in p-Pb collisions at $\sqrt{s_{NN}}$= 5.02 TeV," *Phys. Rev.* **C91** no. 6, (2015) 064905, `arXiv:1412.6828 [nucl-ex]`.

[66] M. L. Miller, K. Reygers, S. J. Sanders, and P. Steinberg, "Glauber modeling in high energy nuclear collisions," *Ann. Rev. Nucl. Part. Sci.* **57** (2007) 205–243, `arXiv:nucl-ex/0701025 [nucl-ex]`.

[67] **ALICE collaboration** Collaboration, "Quarkonium signal extraction in ALICE,". `https://cds.cern.ch/record/2060096`.

[68] **ALICE** Collaboration, B. Abelev *et al.*, "*J/ψ* polarization in *pp* collisions at $\sqrt{s}$ = 7 TeV," *Phys. Rev. Lett.* **108** (2012) 082001, `arXiv:1111.1630 [hep-ex]`.

[69] **CMS** Collaboration, S. Chatrchyan *et al.*, "Measurement of the Prompt *J/ψ* and *ψ*(2S) Polarizations in *pp* Collisions at $\sqrt{s}$ = 7 TeV," *Phys. Lett.* **B727** (2013) 381–402, `arXiv:1307.6070 [hep-ex]`.

[70] **LHCb** Collaboration, R. Aaij *et al.*, "Measurement of *J/ψ* polarization in *pp* collisions at $\sqrt{s}$ = 7 TeV," *Eur. Phys. J.* **C73** no. 11, (2013) 2631, `arXiv:1307.6379 [hep-ex]`.

[71] **ALICE** Collaboration, S. Acharya *et al.*, "Measurement of the inclusive J/ *ψ* polarization at forward rapidity in pp collisions at $\sqrt{s}$ = **8** TeV," *Eur. Phys. J.* **C78** no. 7, (2018) 562, `arXiv:1805.04374 [hep-ex]`.

[72] **ALICE** Collaboration, B. B. Abelev *et al.*, "Measurement of visible cross sections in proton-lead collisions at $\sqrt{s_{NN}}$ = 5.02 TeV in van der Meer scans with the ALICE detector," *JINST* **9** no. 11, (2014) P11003, `arXiv:1405.1849 [nucl-ex]`.

[73] **ALICE Collaboration, LHCb Collaboration** Collaboration, "Reference *pp* cross-sections for *J/ψ* studies in proton-lead collisions at $\sqrt{s_{NN}}$ = 5.02 TeV and comparisons between ALICE and LHCb results,". `http://cds.cern.ch/record/1639617`. CONF-2013-013.

[74] **ALICE** Collaboration, B. B. Abelev *et al.*, "*J/ψ* production and nuclear effects in p-Pb collisions at $\sqrt{S_{NN}}$ = 5.02 TeV," *JHEP* **02** (2014) 073, `arXiv:1308.6726 [nucl-ex]`.

[75] **ALICE** Collaboration, J. Adam *et al.*, "Rapidity and transverse-momentum dependence of the inclusive J/*ψ* nuclear modification factor in p-Pb collisions at $\sqrt{s_{NN}}$ = 5.02 TeV," *JHEP* **06** (2015) 055, `arXiv:1503.07179 [nucl-ex]`.

[76] **ALICE** Collaboration, J. Adam *et al.*, "Centrality dependence of inclusive J/*ψ* production in p-Pb collisions at $\sqrt{s_{NN}}$ = 5.02 TeV," *JHEP* **11** (2015) 127, `arXiv:1506.08808 [nucl-ex]`.

[77] **ALICE** Collaboration, S. Acharya *et al.*, "Inclusive J/*ψ* production at forward and backward rapidity in p-Pb collisions at $\sqrt{s_{NN}}$ = 8.16 TeV," *JHEP* **07** (2018) 160, `arXiv:1805.04381 [nucl-ex]`.

[78] **LHCb** Collaboration, R. Aaij *et al.*, "Prompt and nonprompt J/ψ production and nuclear modification in pPb collisions at $\sqrt{s_{\text{NN}}}$ = 8.16 TeV," *Phys. Lett.* **B774** (2017) 159–178, arXiv:1706.07122 [hep-ex].

[79] J. L. Albacete *et al.*, "Predictions for Cold Nuclear Matter Effects in p+Pb Collisions at $\sqrt{s_{NN}}$ = 8.16 TeV," *Nucl. Phys.* **A972** (2018) 18–85, arXiv:1707.09973 [hep-ph].

[80] E. G. Ferreiro, F. Fleuret, J. P. Lansberg, and A. Rakotozafindrabe, "Impact of the Nuclear Modification of the Gluon Densities on J/ψ production in pPb collisions at $\sqrt{s_{NN}}$ = 5 TeV," *Phys. Rev.* **C88** no. 4, (2013) 047901, arXiv:1305.4569 [hep-ph].

[81] F. Arleo, R. Kolevatov, S. Peigné, and M. Rustamova, "Centrality and pT dependence of J/psi suppression in proton-nucleus collisions from parton energy loss," *JHEP* **05** (2013) 155, arXiv:1304.0901 [hep-ph].

[82] J.-P. Lansberg and H.-S. Shao, "Towards an automated tool to evaluate the impact of the nuclear modification of the gluon density on quarkonium, D and B meson production in proton-nucleus collisions," *Eur. Phys. J.* **C77** no. 1, (2017) 1, arXiv:1610.05382 [hep-ph].

[83] **ALICE** Collaboration, J. Adam *et al.*, "Centrality dependence of ψ(2S) suppression in p-Pb collisions at $\sqrt{s_{\text{NN}}}$ = 5.02 TeV," *JHEP* **06** (2016) 050, arXiv:1603.02816 [nucl-ex].

[84] **PHENIX** Collaboration, A. Adare *et al.*, "Transverse-Momentum Dependence of the J/ψ Nuclear Modification in d+Au Collisions at $\sqrt{s_{NN}}$ = 200 GeV," *Phys. Rev.* **C87** no. 3, (2013) 034904, arXiv:1204.0777 [nucl-ex].

[85] Z.-B. Kang and J.-W. Qiu, "Transverse momentum broadening of vector boson production in high energy nuclear collisions," *Phys. Rev.* **D77** (2008) 114027, arXiv:0802.2904 [hep-ph].

[86] Z.-B. Kang and J.-W. Qiu, "Nuclear modification of vector boson production in proton-lead collisions at the LHC," *Phys. Lett.* **B721** (2013) 277–283, arXiv:1212.6541 [hep-ph].

[87] **ALICE** Collaboration, D. Adamová *et al.*, "J/ψ production as a function of charged-particle pseudorapidity density in p-Pb collisions at $\sqrt{s_{\text{NN}}}$ = 5.02 TeV," *Phys. Lett.* **B776** (2018) 91–104, arXiv:1704.00274 [nucl-ex].

[88] J. Crkovská, *Study of the* J/ψ *production in pp collisions at* $\sqrt{s}$ = 5.02 *TeV and of the* J/ψ *production multiplicity dependence in p-Pb collisions at* $\sqrt{s_{NN}}$ = 8.16 *TeV with ALICE at the LHC*. PhD thesis, Institut de Physique Nucl/'eaire d'Orsay, France, 2018. https://tel.archives-ouvertes.fr/tel-01952850.

[89] **ALICE** Collaboration, S. Acharya *et al.*, "Search for collectivity with azimuthal J/ψ-hadron correlations in high multiplicity p-Pb collisions at $\sqrt{s_{\text{NN}}}$ = 5.02 and 8.16 TeV," *Phys. Lett.* **B780** (2018) 7–20, arXiv:1709.06807 [nucl-ex].

[90] **ALICE** Collaboration, B. Abelev *et al.*, "J/ψ Production as a Function of Charged Particle Multiplicity in pp Collisions at $\sqrt{s}$ = 7 TeV," *Phys. Lett.* **B712** (2012) 165–175, arXiv:1202.2816 [hep-ex].

[91] **CMS** Collaboration, V. Khachatryan *et al.*, "Observation of Long-Range Near-Side Angular Correlations in Proton-Proton Collisions at the LHC," *JHEP* **09** (2010) 091, arXiv:1009.4122 [hep-ex].

[92] **CMS** Collaboration, S. Chatrchyan *et al.*, "Observation of Long-Range Near-Side Angular Correlations in Proton-Lead Collisions at the LHC," *Phys. Lett.* **B718** (2013) 795–814, `arXiv:1210.5482 [nucl-ex]`.

[93] **ALICE** Collaboration, B. Abelev *et al.*, "Long-range angular correlations on the near and away side in *p*-Pb collisions at $\sqrt{s_{NN}}$ = 5.02 TeV," *Phys. Lett.* **B719** (2013) 29–41, `arXiv:1212.2001 [nucl-ex]`.

[94] **ATLAS** Collaboration, G. Aad *et al.*, "Observation of Associated Near-Side and Away-Side Long-Range Correlations in $\sqrt{s_{NN}}$=5.02 TeV Proton-Lead Collisions with the ATLAS Detector," *Phys. Rev. Lett.* **110** no. 18, (2013) 182302, `arXiv:1212.5198 [hep-ex]`.

[95] **ALICE** Collaboration, B. B. Abelev *et al.*, "Long-range angular correlations of π, K and p in p-Pb collisions at $\sqrt{s_{NN}}$ = 5.02 TeV," *Phys. Lett.* **B726** (2013) 164–177, `arXiv:1307.3237 [nucl-ex]`.

[96] **CMS** Collaboration, V. Khachatryan *et al.*, "Long-range two-particle correlations of strange hadrons with charged particles in pPb and PbPb collisions at LHC energies," *Phys. Lett.* **B742** (2015) 200–224, `arXiv:1409.3392 [nucl-ex]`.

[97] **ALICE** Collaboration, K. Aamodt *et al.*, "Harmonic decomposition of two-particle angular correlations in Pb-Pb collisions at $\sqrt{s_{NN}}$ = 2.76 TeV," *Phys. Lett.* **B708** (2012) 249–264, `arXiv:1109.2501 [nucl-ex]`.

[98] K. Dusling and R. Venugopalan, "Comparison of the color glass condensate to dihadron correlations in proton-proton and proton-nucleus collisions," *Phys. Rev.* **D87** no. 9, (2013) 094034, `arXiv:1302.7018 [hep-ph]`.

[99] A. Bzdak and G.-L. Ma, "Elliptic and triangular flow in *p*+Pb and peripheral Pb+Pb collisions from parton scatterings," *Phys. Rev. Lett.* **113** no. 25, (2014) 252301, `arXiv:1406.2804 [hep-ph]`.

[100] **ALICE** Collaboration, B. B. Abelev *et al.*, "Suppression of ψ(2S) production in p-Pb collisions at $\sqrt{s_{NN}}$ = 5.02 TeV," *JHEP* **12** (2014) 073, `arXiv:1405.3796 [nucl-ex]`.

[101] **ATLAS** Collaboration, M. Aaboud *et al.*, "Measurement of quarkonium production in proton?lead and proton?proton collisions at 5.02 TeV with the ATLAS detector," *Eur. Phys. J.* **C78** no. 3, (2018) 171, `arXiv:1709.03089 [nucl-ex]`.

[102] **CMS** Collaboration, A. M. Sirunyan *et al.*, "Measurement of prompt ψ(2S) production cross sections in proton-lead and proton-proton collisions at $\sqrt{s_{NN}}$ = 5.02 TeV," *Phys. Lett.* **B790** (2019) 509–532, `arXiv:1805.02248 [hep-ex]`.

[103] I. Helenius and H. Paukkunen, "Revisiting the D-meson hadroproduction in general-mass variable flavour number scheme," *JHEP* **05** (2018) 196, `arXiv:1804.03557 [hep-ph]`.

[104] L. Gladilin, "Fragmentation fractions of *c* and *b* quarks into charmed hadrons at LEP," *Eur. Phys. J.* **C75** no. 1, (2015) 19, `arXiv:1404.3888 [hep-ex]`.

[105] **ALICE** Collaboration, S. Acharya *et al.*, "Λ_c^+ production in pp collisions at $\sqrt{s}$ = 7 TeV and in p-Pb collisions at $\sqrt{s_{NN}}$ = 5.02 TeV," *JHEP* **04** (2018) 108, `arXiv:1712.09581 [nucl-ex]`.

[106] **LHCb** Collaboration, R. Aaij *et al.*, "Prompt Λ_c^+ production in *p*Pb collisions at $\sqrt{s_{NN}}$ = 5.02 TeV," *JHEP* **02** (2019) 102, `arXiv:1809.01404 [hep-ex]`.

[107] H. Fujii and K. Watanabe, "Nuclear modification of forward D production in pPb collisions at the LHC," arXiv:1706.06728 [hep-ph].

[108] **ALICE** Collaboration, S. Acharya *et al.*, "Measurement of prompt D^0, D^+, D^{*+}, and D_s^+ production in p−Pb collisions at $\sqrt{s_{NN}}$ = **5.02 TeV**," arXiv:1906.03425 [nucl-ex].

[109] **LHCb** Collaboration, R. Aaij *et al.*, "Study of prompt D^0 meson production in pPb collisions at $\sqrt{s_{NN}}$ = 5 TeV," *JHEP* **10** (2017) 090, arXiv:1707.02750 [hep-ex].

[110] **ALICE** Collaboration, S. Acharya *et al.*, "Inclusive Υ production in p-Pb collisions at $\sqrt{s_{NN}}$ = 8.16 TeV," arXiv:1910.14405 [nucl-ex].

[111] **LHCb** Collaboration, R. Aaij *et al.*, "Study of Υ production in pPb collisions at $\sqrt{s_{NN}}$ = 8.16 TeV," *JHEP* **11** (2018) 194, arXiv:1810.07655 [hep-ex].

[112] **CMS Collaboration** Collaboration, "Nuclear modification of Υ states in pPb collisions at $\sqrt{s_{NN}}$ = 5.02 TeV," Tech. Rep. CMS-PAS-HIN-18-005, CERN, Geneva, 2019. https://cds.cern.ch/record/2699566.

[113] **CMS** Collaboration, S. Chatrchyan *et al.*, "Event Activity Dependence of Y(nS) Production in $\sqrt{s_{NN}}$=5.02 TeV pPb and $\sqrt{s}$=2.76 TeV pp Collisions," *JHEP* **04** (2014) 103, arXiv:1312.6300 [nucl-ex].

[114] E. G. Ferreiro and J.-P. Lansberg, "Is bottomonium suppression in proton-nucleus and nucleus-nucleus collisions at LHC energies due to the same effects?," arXiv:1804.04474 [hep-ph].

[115] A. B. Kurepin, N. S. Topilskaya, and M. B. Golubeva, "Charmonium production in fixed-target experiments with SPS and LHC beams at CERN," *Phys. Atom. Nucl.* **74** (2011) 446–452. [Yad. Fiz.74,467(2011)].

[116] S. J. Brodsky, F. Fleuret, C. Hadjidakis, and J. P. Lansberg, "Physics Opportunities of a Fixed-Target Experiment using the LHC Beams," *Phys. Rept.* **522** (2013) 239–255, arXiv:1202.6585 [hep-ph].

[117] C. Hadjidakis *et al.*, "A Fixed-Target Programme at the LHC: Physics Case and Projected Performances for Heavy-Ion, Hadron, Spin and Astroparticle Studies," arXiv:1807.00603 [hep-ex].

[118] L. Massacrier, B. Trzeciak, F. Fleuret, C. Hadjidakis, D. Kikola, J. P. Lansberg, and H. S. Shao, "Feasibility studies for quarkonium production at a fixed-target experiment using the LHC proton and lead beams (AFTER@LHC)," *Adv. High Energy Phys.* **2015** (2015) 986348, arXiv:1504.05145 [hep-ex].

[119] B. Trzeciak, C. Da Silva, E. G. Ferreiro, C. Hadjidakis, D. Kikola, J. P. Lansberg, L. Massacrier, J. Seixas, A. Uras, and Z. Yang, "Heavy-ion Physics at a Fixed-Target Experiment Using the LHC Proton and Lead Beams (AFTER@LHC): Feasibility Studies for Quarkonium and Drell-Yan Production," *Few Body Syst.* **58** no. 5, (2017) 148, arXiv:1703.03726 [nucl-ex].

[120] D. Kikola, M. G. Echevarria, C. Hadjidakis, J.-P. Lansberg, C. Lorce, L. Massacrier, C. M. Quintans, A. Signori, and B. Trzeciak, "Feasibility Studies for Single Transverse-Spin Asymmetry Measurements at a Fixed-Target Experiment Using the LHC Proton and Lead Beams (AFTER@LHC)," *Few Body Syst.* **58** no. 4, (2017) 139, arXiv:1702.01546 [hep-ex].

[121] **STAR** Collaboration, L. Adamczyk *et al.*, "Centrality dependence of identified particle elliptic flow in relativistic heavy ion collisions at $\sqrt{s_{NN}}$=7.7-62.4 GeV," *Phys. Rev.* **C93** no. 1, (2016) 014907, `arXiv:1509.08397 [nucl-ex]`.

[122] **STAR** Collaboration, L. Adamczyk *et al.*, "Elliptic flow of identified hadrons in Au+Au collisions at $\sqrt{s_{NN}}$ = 7.7-62.4 GeV," *Phys. Rev.* **C88** (2013) 014902, `arXiv:1301.2348 [nucl-ex]`.

[123] **STAR** Collaboration, L. Adamczyk *et al.*, "Inclusive charged hadron elliptic flow in Au + Au collisions at $\sqrt{s_{NN}}$ = 7.7 - 39 GeV," *Phys. Rev.* **C86** (2012) 054908, `arXiv:1206.5528 [nucl-ex]`.

[124] **STAR** Collaboration, L. Adamczyk *et al.*, "Beam Energy Dependence of Jet-Quenching Effects in Au+Au Collisions at $\sqrt{s_{NN}}$ = 7.7, 11.5, 14.5, 19.6, 27, 39, and 62.4 GeV," `arXiv:1707.01988 [nucl-ex]`.

[125] F. Becattini and J. Cleymans, "Chemical Equilibrium in Heavy Ion Collisions: Rapidity Dependence," *J. Phys.* **G34** (2007) S959–964, `arXiv:hep-ph/0701029 [hep-ph]`.

[126] V. Begun, D. Kikola, V. Vovchenko, and D. Wielanek, "Estimation of the freeze-out parameters reachable in the AFTER@LHC project," `arXiv:1806.01303 [nucl-th]`.

[127] I. Karpenko, "Rapidity scan in heavy ion collisions at $\sqrt{s_{NN}}$ = 72 GeV using a viscous hydro + cascade model," `arXiv:1805.11998 [nucl-th]`.

[128] A. Mocsy, P. Petreczky, and M. Strickland, "Quarkonia in the Quark Gluon Plasma," *Int. J. Mod. Phys.* **A28** (2013) 1340012, `arXiv:1302.2180 [hep-ph]`.

[129] **LHCb** Collaboration, R. Aaij *et al.*, "Precision luminosity measurements at LHCb," *JINST* **9** no. 12, (2014) P12005, `arXiv:1410.0149 [hep-ex]`.

[130] C. Barschel, *Precision luminosity measurement at LHCb with beam-gas imaging*. PhD thesis, RWTH Aachen U., 2014. `http://inspirehep.net/record/1339684/files/CERN-THESIS-2013-301.pdf`.

[131] C. Barschel *et al.*, "Report from the LHC Fixed Target working group of the CERN Physics Beyond Colliders forum," Tech. Rep. CERN-PBC-REPORT-2019-001, CERN, Geneva, Mar, 2019. `https://cds.cern.ch/record/2653780`.

[132] M. Ferro-Luzzi, S. Redaelli, and C. Hadjidakis, "Studies for future fixed-target experiments at the LHC in the framework of the CERN Physics Beyond Colliders study," **IPAC2018** (2018) TUPAF045.

[133] T. Pierog, I. Karpenko, J. M. Katzy, E. Yatsenko, and K. Werner, "EPOS LHC: Test of collective hadronization with data measured at the CERN Large Hadron Collider," *Phys. Rev.* **C92** no. 3, (2015) 034906, `arXiv:1306.0121 [hep-ph]`.

[134] K. Werner, F.-M. Liu, and T. Pierog, "Parton ladder splitting and the rapidity dependence of transverse momentum spectra in deuteron-gold collisions at RHIC," *Phys. Rev.* **C74** (2006) 044902, `arXiv:hep-ph/0506232 [hep-ph]`.

[135] R. Aaij *et al.*, "Performance of the LHCb Vertex Locator," *JINST* **9** (2014) P09007, `arXiv:1405.7808 [physics.ins-det]`.

[136] **LHCb** Collaboration, R. Aaij *et al.*, "Measurement of antiproton production in pHe collisions at $\sqrt{s_{NN}}$ = 110 GeV," `arXiv:1808.06127 [hep-ex]`.

[137] **LHCb** Collaboration, R. Aaij *et al.*, "First Measurement of Charm Production in its Fixed-Target Configuration at the LHC," *Phys. Rev. Lett.* **122** no. 13, (2019) 132002, `arXiv:1810.07907 [hep-ex]`.

[138] P. Di Nezza *et al.*, "The SMOG2 project,". `http://cds.cern.ch/record/2651269`.

[139] **LHCb** Collaboration, "LHCb SMOG Upgrade,". `https://cds.cern.ch/record/2673690`.

[140] G. Graziani, "LHCb as a fixed target experiment." Physics Beyond Collider, General Meeting, November 5, 2019.

[141] **HERMES** Collaboration, A. Airapetian *et al.*, "The HERMES polarized hydrogen and deuterium gas target in the HERA electron storage ring," *Nucl. Instrum. Meth.* **A540** (2005) 68–101, `arXiv:physics/0408137 [physics]`.

[142] C. A. Aidala *et al.*, "The LHCSpin Project," `arXiv:1901.08002 [hep-ex]`.

[143] J. Linhard *K. Dan. Vidensk. Selsk. Mat. Fys. Medd.34* **14** (1965) .

[144] D. Gemmell *Rev.Mod.Physics* **46** (1974) 129.

[145] E. Tsyganov *Preprint TM-682, TM-684, Fermilab, Batavia* (1976) .

[146] W. Scandale *et al.*, "First results on the SPS beam collimation with bent crystals," *Phys. Lett.* **B692** (2010) 78–82.

[147] W. Scandale *et al.*, "Observation of channeling for 6500 GeV/ c protons in the crystal assisted collimation setup for LHC," *Phys. Lett.* **B758** (2016) 129–133.

[148] X. Altuna *et al.*, "High efficiency multipass proton beam extraction with a bent crystal at the SPS," *Phys. Lett.* **B357** (1995) 671–677.

[149] F. Galluccio, C. Hadjidakis, A. Kurepin, L. Massacrier, S. Porteboeuf, K. Pressard, W. Scandale, N. Topilskaya, B. Trzeciak, A. Uras, and D. Kikola, "Physics opportunities for a fixed-target programme in the ALICE experiment,". `http://cds.cern.ch/record/2671944`.

[150] A. S. Fomin *et al.*, "Feasibility of measuring the magnetic dipole moments of the charm baryons at the LHC using bent crystals," *JHEP* **08** (2017) 120, `arXiv:1705.03382 [hep-ph]`.

[151] E. Bagli *et al.*, "Electromagnetic dipole moments of charged baryons with bent crystals at the LHC," *Eur. Phys. J.* **C77** no. 12, (2017) 828, `arXiv:1708.08483 [hep-ex]`.

[152] F. J. Botella, L. M. Garcia Martin, D. Marangotto, F. M. Vidal, A. Merli, N. Neri, A. Oyanguren, and J. R. Vidal, "On the search for the electric dipole moment of strange and charm baryons at LHC," *Eur. Phys. J.* **C77** no. 3, (2017) 181, `arXiv:1612.06769 [hep-ex]`.

[153] D. Mirarchi, A. S. Fomin, S. Redaelli, and W. Scandale, "Layouts for fixed-target experiments and dipole moment measurements of short-living baryons using bent crystals at the LHC," `arXiv:1906.08551 [physics.acc-ph]`.

[154] F. Arleo and S. Peigne, "Quarkonium suppression from coherent energy loss in fixed-target experiments using LHC beams," *Adv. High Energy Phys.* **2015** (2015) 961951, `arXiv:1504.07428 [hep-ph]`.

[155] **PHENIX** Collaboration, C. Aidala *et al.*, "Measurements of Multiparticle Correlations in d + Au Collisions at 200, 62.4, 39, and 19.6 GeV and p + Au Collisions at 200 GeV and Implications for Collective Behavior," *Phys. Rev. Lett.* **120** no. 6, (2018) 062302, `arXiv:1707.06108 [nucl-ex]`.

[156] P. Bozek and W. Broniowski, "Elliptic Flow in Ultrarelativistic Collisions with Polarized Deuterons," *Phys. Rev. Lett.* **121** no. 20, (2018) 202301, `arXiv:1808.09840 [nucl-th]`.

[157] B. Abelev *et al.*, "Upgrade of the alice experiment: Letter of intent," *Journal of Physics G: Nuclear and Particle Physics* **41** no. 8, (Jul, 2014) 087001.

[158] **ALICE Collaboration** Collaboration, "Addendum of the Letter of Intent for the upgrade of the ALICE experiment : The Muon Forward Tracker," Tech. Rep. CERN-LHCC-2013-014. LHCC-I-022-ADD-1, CERN, Geneva, Aug, 2013. `http://cds.cern.ch/record/1592659`. Final submission of the presetn LoI addendum is scheduled for September 7th.

[159] Z. Citron *et al.*, "Report from Working Group 5," in *Report on the Physics at the HL-LHC,and Perspectives for the HE-LHC*, A. Dainese, M. Mangano, A. B. Meyer, A. Nisati, G. Salam, and M. A. Vesterinen, eds., pp. 1159–1410. 2019. `arXiv:1812.06772 [hep-ph]`.

[160] **PHENIX** Collaboration, A. Adare *et al.*, "An Upgrade Proposal from the PHENIX Collaboration," `arXiv:1501.06197 [nucl-ex]`.